The Dissertation Committee for Mahesh Srinivasan Certifies that this is the approved version of the following dissertation:

Hierarchical Control of DC Microgrids with Constant Power Loads

Committee:

Ross Baldick, Supervisor

Alexis Kwasinski

Aristotle Arapostathis

Gary Hallock

Robert Hebner

Hierarchical Control of DC Microgrids with Constant Power Loads

by

Mahesh Srinivasan BE, MSc(Engg)

Dissertation

Presented to the Faculty of the Graduate School of

The University of Texas at Austin

in Partial Fulfillment

of the Requirements

for the Degree of

Doctor of Philosophy

The University of Texas at Austin

August 2017

Dedication

Dedicated to my parents

Hierarchical Control of DC Microgrids with Constant Power Loads

Mahesh Srinivasan PhD

The University of Texas at Austin, 2017

Supervisor: Ross Baldick

This dissertation proposes general methodologies for designing hierarchical control schemes for dc microgrids loaded by constant power loads (CPLs). CPLs form a major proportion of the system loads in many microgrids. Without proper control, CPLs present destabilizing effect at the dc microgrid. In addition to stable operation of microgrid, proper current sharing among paralleled sources is essential. The proposed hierarchical control strategy consists of two control levels. The lower level consists of droop-based primary controllers which enables current-sharing among paralleled sources and also damps limit cycle oscillations due to CPLs. The higher level consists of secondary controller which compensates for voltage deviations due to primary controller. This higher level is implemented either as autonomous controllers or as a centralized controller. In the case of autonomous secondary controllers, they operate alongside of primary controllers in each of the paralleled converters. In the case of centralized secondary controller, a remote secondary controller uses a high speed communication link to communicate to local controllers.

Interfacing sources with different characteristics and voltage ranges necessitates the use of complex converter topologies. As an initial step towards implementing hierarchical control scheme for such microgrids with CPLs, a linear controller is proposed for dc microgrids with standalone SEPIC, Cuk and Zeta converters. During the

first stage of the two stage controller, limit cycle oscillations are damped by inserting a virtual resistance in series with the converter input inductor. During the second stage, an integral controller is added to the first stage to compensate for voltage deviations. For microgrids containing different converter topologies, stability of equilibrium points is examined and stability conditions are derived and explained. Experiments performed on a prototype microgrid are used to verify the proposed control laws.

Expanding study on stability of microgrids, the maximum real power load in a dc microgrid bus is traced geometrically. The generalized circle diagram approach used in a conventional power system is modified for this purpose. The different types of buses present in a dc microgrid are described and the locus of operating points is obtained. The proposed method is verified by simulations on an example dc microgrid.

Table of Contents

List of Tables

List of Figures

Chapter 1: Introduction

Traditional power system architecture mainly consists of three stages namely generation, transmission and distribution with clearly demarcated boundaries between stages. However, increasing energy concerns have led towards improvement of existing power system architectures and research and development of newer power system architectures [1]. Some concerns include reliability of power system, depletion of fossil fuels, increase in energy consumed and augmentation of existing transmission capacity to meet increasing load [1][2][3]. To address these concerns, part of energy that is required by the consumers is produced near the loads [4]. With increasing penetration of distributed generation (DG), newer power system architectures termed microgrids have come to coexist with the traditional power system architectures [5].

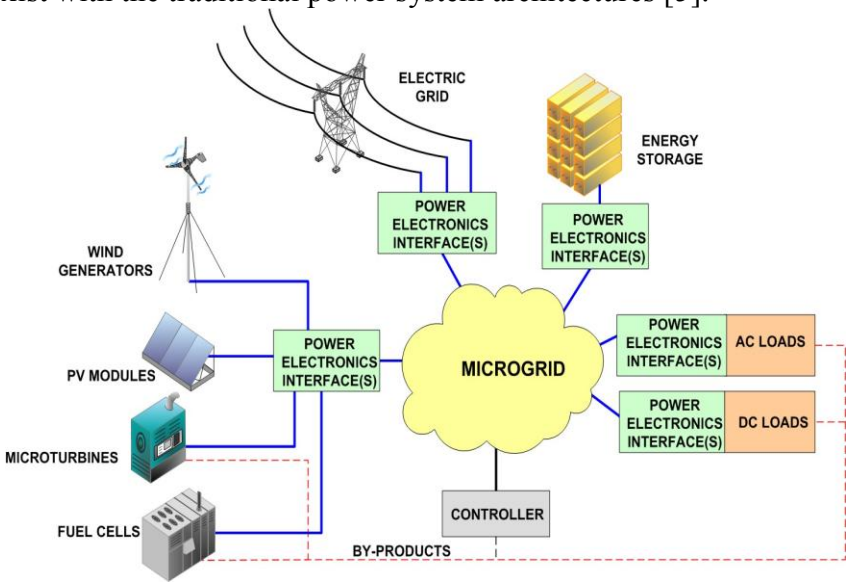

Figure. 1. Architecture of a microgrid [6]

ADVANTAGES AND ISSUES OF DC MICROGRIDS

US department of energy, DoE defines microgrids as "Locally confined and independently controlled electric power grids in which distribution architecture integrates

loads and distributed energy resources which allows the microgrid to operate connected or isolated to a main grid" [7]. The architecture of a general microgrid is given in Fig. 1. In a microgrid, different power sources and energy storage have different characteristics and varying voltage levels. So they are connected in parallel through power electronic converters at the microgrid [8] as can be seen from Fig. 1. In addition to microgrids interfaced to traditional grids, a number of standalone microgrids like electric ships, remote telecom and data centers and electric vehicles are receiving prominence [9]. One of the shining examples of this trend is the increasing proportion of hybrid electric vehicles (HEV) and plug-in hybrid electric vehicles (PHEV) in the automotive industry [10]. Although more development work is done with regard to ac microgrids, recently dc microgrids are receiving good attention [11]. DC microgrids do not have frequency or reactive power related issues and hence analysis and design of control loops is easier [12]. In addition, a number of sources like solar panels, fuel cells, energy storage and present day electronic loads are inherently dc [13]. Reliability concerns of microgrids have been addressed by proposing a number of standards and improving them subsequently [14], [15]. However, dedicated standards for operating dc microgrids are yet to be developed [16]. Another challenge with regard to a dc microgrid is that of design of a reliable protection and isolation scheme for the same [16].

CONSTANT POWER LOADS AND EXISTING CONTROL METHODS

While analyzing the microgrid loads, the presence of constant power loads (CPL)s in the present day microgrids has to be taken into account [17]. It is expected that in most dc microgrids, loads would behave as instantaneous constant-power loads (CPLs) to the converters located upstream (line regulating converters or LRCs) interfacing the sources and the microgrid main bus [17] [18]. Some examples for CPLs in the microgrids are as

follows. With regard to automotive microgrids, multiple dc voltage buses may be observed in today's vehicular power systems. Typically, the higher voltage dc bus supplies the motor drive that propels the vehicle. Lower voltage dc buses supply other loads within the vehicle [19]. These loads are connected to the dc buses through dc-dc converters with a fast regulating controller making them behave as constant power loads (CPLs). Another example of a CPL is when the main motor drive regulates the speed keeping the product of torque and speed constant [19]. Energy storage systems (ESS) like batteries which are charged in regulated charging mode acts as CPL [20]. It is well known that CPLs create a negative impedance instability problem at the dc bus [21]. Without proper control, voltage oscillations may be observed at the dc bus in the form of limit cycles or lead to a tendency for the bus voltage to collapse.

The stability aspects of microgrids are characterized in [22] where lack of system damping due to constant power loads (CPLs) is discussed under broader area namely small signal instability. In the past, several control methods have been proposed to address this issue. They can be broadly divided into linear methods, non-linear methods or use of passive components [12]. Among the prominent linear schemes, the method studied in [18] uses a proportional and differential controller to stabilize the dc-dc buck converter. Another method proposed in [23] uses the converter inductor current feedback to damp limit cycle oscillations. The method proposed in [24] deals with converters having an LCL output filter. The methodology suggested in [24] proposes control techniques to replicate the process of inserting resistances and capacitances in the converter circuit to attain stability. An active damping technique for a voltage source converter (VSC) based dc microgrid with CPLs is proposed in [25]. Among the prominent nonlinear methods is the method proposed in [31] which uses a hysteresis controller with a first order switching surface with a negative slope. In the method

proposed in [27], a feedback control term is added which modifies the CPL term into a constant power source (CPS) and hence adds damping to the system. In [28], the CPL non-linear state equation is converted into a linear state equation by considering the energy stored in the capacitor as a state variable. A combination of linear and nonlinear control schemes for a synchronous buck converter is considered in [29]. In [30], a non-linear PD controller is derived using passivity based analysis to stabilize non-minimum phase converters like boost and buckboost. This non-linear PD controller is replaced with a linear PD controller which stabilizes the boost and buckboost converters supplying a CPL. Current mode control has been suggested to damp the oscillations due to a CPL fed by a boost converter in [32]. But to improve the transient response, [32] employs load current feedback which involves a parameter external to the converter and, hence, may be argued that lacks autonomy characteristics. Passive damping methods use inefficient methods by adding physical resistors to damp oscillations. Passive damping methods make assumptions on power distribution circuits or on other parameters so that such limit cycle oscillations are considered to be non-existent [33], [34], [35], [36]. In such systems, inherent damping is present in the form of renewable energy sources (RES) acting as constant power sources (CPSs), transmission lines and filters, other resistive loads and ESS directly connected to the dc microgrid. However, such passive components are bulky, which is in contrary to the current requirements of many industrial domains like automotive and aerospace [37]. A comprehensive list of stability schemes for dc microgrids, protection issues and evaluation of the same is presented in [12], [16].

HIERARCHICAL CONTROL APPROACH - EXISTING METHOD AND ISSUES

A general framework of a hierarchical control scheme for both grid-connected as well as islanded microgrids is introduced in [38]. This control scheme consists of 3 levels

namely primary, secondary and tertiary. The primary control level uses the droop mechanism to enable current sharing among the sources. The main advantage about the droop approach is that it is a low cost, reliable and modular scheme [39], [40]. The second stage consists of a secondary controller which has an integral action and compensates for voltage deviations due to primary controller. In current literature, secondary controller is implemented as a single centralized controller with a high bandwidth communication channel [41] to each of the local controllers. Recent work also implements secondary control in the form of a distributed controller with low bandwidth communication channels between the controllers [42], [43]. The tertiary control level manages the flow of power between the microgrid and the main power grid. Other than the three control levels mentioned above, there are inner control loops which are implemented for each paralleled converter. However, recent work [33] has shown that the internal voltage and current loops are much faster than droop controller and hence they can be assumed to maintain the respective variables at their reference values. Recent work on the control of an islanded microgrid focuses on the coordinated operation of renewable energy sources (RES), energy storage systems (ESS) and the loads that may be present in the microgrid [44], [20], [45], [46], [47]. The stability of such a microgrid is dependent on the control strategy employed by the converters [22]. Existing methods do not seem to provide an understanding of how various converter parameters affect microgrid stability. There seems to be no analysis or control techniques developed based on different converter topologies that may be present in a microgrid. Another issue with regard to hierarchical control methodology proposed in the literature is that the microgrid loads are assumed to be resistive.

CONTRIBUTIONS

In this dissertation, a general methodology to design hierarchical control scheme for dc microgrids with CPLs is developed. The developed methodology is applicable to dc microgrids containing a wide array of non-isolated dc-dc converter topologies loaded by CPLs. The lower control level namely droop based primary controller performs dual function of current sharing as well as damping limit cycle oscillations due to CPL. Thus, damping of CPL induced oscillations and current sharing among paralleled converters is realized by control action. This is one of the main contributions of the research work. Two different architectures of secondary controllers are developed and are shown in Figs. (2) and (3). Firstly, an autonomous secondary controller is considered. Here, secondary controller is implemented in each of the paralleled converters and exists alongside of each of the primary controllers. Each secondary controller senses the microgrid voltage independently and sends the secondary control signals to the respective converter modules based on the integral control gains. Autonomous controllers are desired in order to share the load among LRCs in order to avoid single point of failures in communication links or in central controllers. Although a central controller can still be used to optimize system operation, local autonomous controllers are used in order to share among sources power differences between the optimal operation point and the actual system operating point. Such differences may originate in system losses or in a failure in the central controller. Hence, local autonomous controllers allow the system to operate—although in a sub-optimal state—when the central controller or its communication links fail. This control scheme consisting of droop based primary controller and autonomous secondary controllers is named as autonomous hierarchical control scheme and is shown in Fig. 2. Secondly, a centralized secondary controller with a high speed communication link is also implemented. In this scheme, a remote secondary controller senses the microgrid

voltage and calculates the secondary control signal. The secondary control signal is transmitted to the parallel converters using a high speed controller area network (CAN) communication link. This control methodology (primary and a centralized secondary controller) is named as a semi-autonomous hierarchical control scheme and is shown in Fig. 3. Important relations regarding droop characteristics, maximum load supplied and current sharing are compared and established for microgrids containing different converter topologies. Stability conditions for the different equilibrium points are derived and are related to the converter parameters. Attempts have been made to derive and explain the general stability conditions using the equivalent circuit of the converters.

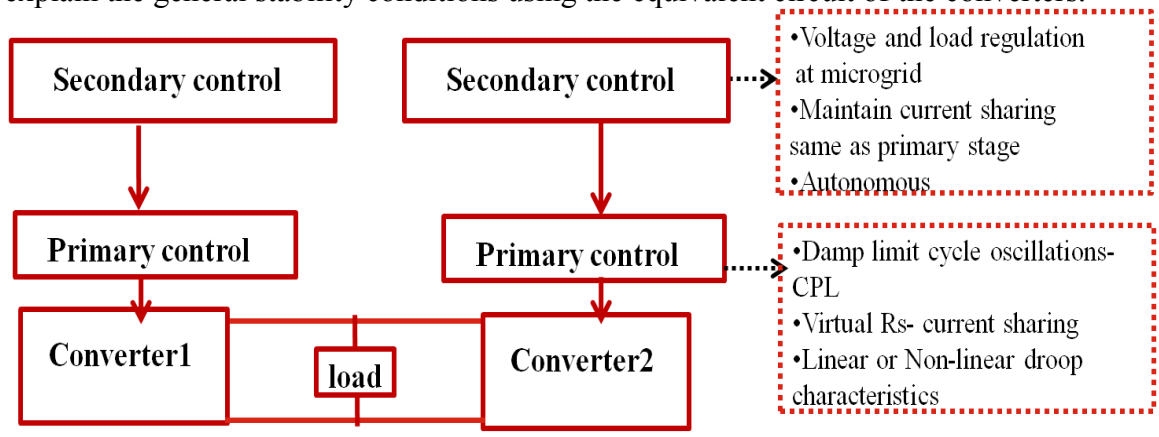

Figure. 2. Autonomous hierarchical control scheme

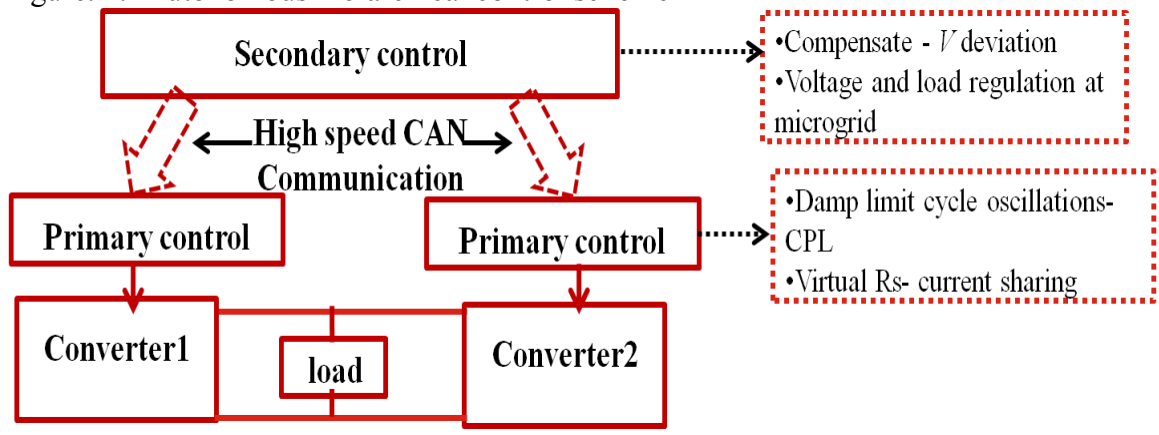

Figure. 3. Semi-autonomous hierarchical control scheme

In the current literature, dc-dc converters supplying power to the microgrid are modeled as a constant voltage sources and a linear droop is realized by an actual or a virtual resistor connected in series with the respective voltage sources. This may be true in the case of buck converters. But in the case of other converter topologies, the equivalent circuit of the converter consists of a transformer with a non-linear turns ratio [48]. Hence a linear droop characteristic may not provide a stable equilibrium point for such converters. Among the various converter topologies, dc-dc boost converters find many applications in vehicular power systems, especially FCVs. Since the output voltage of the fuel cells is not high enough to be directly connected to the inverter of the main motor drive and they require a relatively continuous current waveforms, boost converters are well suited in order to interface fuel cells with the rest of the system [49] [50]. Similarly, ultracapacitors have lower terminal voltages. In the case of batteries, a lower terminal voltage is desired in order to keep its series resistance at a minimum value [51] and reduce cell equalization issues. Hence, boost converters are desired in order to interface ultracapacitors and batteries with the rest of the vehicular dc microgrid [51]. An inherent advantage of boost converters is that the output voltage is not inverted [52]. In addition, boost converters are also used in plug-in hybrid electric vehicle (PHEV) charging stations [53]. However, boost converters are non-minimum phase systems and when such converters are used to supply CPLs, the control of such a system becomes a challenging problem. In chapter 3, autonomous hierarchical control scheme is developed for a microgrid containing parallel boost converters and stability conditions are derived.

Although control of parallel connected converters in a microgrid has been discussed in the literature [42], [33], [54], [55][56], [57], [58], [20]. But such methods consider only simple topologies like buck and boost. Using dc-dc buck or boost

topologies constrains the range of source voltages that can be interfaced with the microgrid. In order to interface sources with wider voltage ranges to a dc microgrid, converters capable of providing output voltages both greater than as well as lesser than the respective source voltages may be required [59]. One such topology is the dc–dc buckboost converter. Further, in the chapters 2 and 3 of this dissertation, autonomous secondary controllers have been assumed. However, in an actual microgrid, the presence of transmission lines in between the various buses has to be taken into account. Also if, multiple converters are trying to regulate the bus voltage with an integral feedback control, bus voltage measurement inaccuracies by individual controllers and sensors have to be considered. The effect of such measurement inaccuracies on system stability has to be studied. [60]. Further in a microgrid, where there are many power electronic converters, the control schemes for the individual converters may interact with each other and make the system unstable [61]. To overcome the above mentioned issues, in chapter 4 a semi-autonomous hierarchical control scheme is developed for a dc microgrid with parallel connected buckboost converters. A remote secondary controller senses the microgrid voltage and calculates the secondary control information. This information is transmitted to paralleled converters using a high speed CAN communication network.

Interfacing sources with different characteristics and different output voltage ranges often requires converters with a more complex topology. For example, a fuel cell needs a converter with a current source interface to connect to microgrid [51]. In addition, there is a requirement for converters to provide output voltages greater than and lesser than their source voltage [51]. Such a requirement makes a Cuk converter a possible candidate. In addition, if there is a requirement for a non-inverted output voltage, then a Single ended primary inductor converter (SEPIC) is a possible candidate [52]. One of the challenges in studying such higher order converters is as follows. A detailed

analysis of state variable trajectories similar to that performed in [26], [62] is difficult in the case of higher order converters since they contain an additional capacitor and inductor [63]. Even though a generalized signal flow graph model has been proposed in [64] for modeling and analysis of fourth order dc-dc converters, the converter loads are assumed to be resistive. The work in [65] proposes a sliding mode controller for a fifth order system which consists of a buck converter with an input filter. However during analysis, the system is reduced to a simpler third order system. In chapter 5, a microgrid containing higher order dc-dc converters supplying CPLs is considered. A linear active damping scheme is developed which is applicable to standalone versions of SEPIC, Cuk and Zeta converters. The control scheme is implemented in two steps. The first step acts as an active damping stage [23] because it consists of inserting a 'virtual' resistance through controller action in series with the input inductor of the converter. An outer loop with a slow integral controller is added to the active damping stage in order to compensate for voltage deviation caused by the aforementioned 'virtual' resistance. This second controller loop is also referred to as voltage regulation stage [2], [31]. The integral controller added in this voltage regulation stage also compensates for supply voltage deviation and load changes. The control algorithms derived for various converter topologies are verified by simulations. Further, experiments on a prototype microgrid also validate the proposed algorithms.

Availability and stable operation of a power electronic converter based distributed generation system is very important especially when they power critical loads like hospitals, telecommunications and air-traffic controls [2]. In [3], large step changes in loads are discussed under the purview of transient stability. However, it is well known that microgrids may typically lack inertia which is an inherent feature of the conventional power grid with large synchronous generators [10]. Among the various aspects of

microgrid stability, voltage stability is related to loadability [3]. Loadability of a bus is the maximum real or reactive power load that can be supplied at that bus. In a conventional power system, the continuation power flow approach [13] is used to obtain the loadability at a bus. In [14], the maximum power transfer condition of a two bus system is generalized to a large system using the Thevenin equivalent circuit of the power system. Based on this equivalent circuit, voltage stability at the load buses of the power system is assessed. However, this method does not explicitly compute the loadability; rather it estimates the proximity of this condition using an index. In the case of a dc microgrid with two buses, the loadability at a bus can be obtained algebraically using the Middlebrook criterion [15]. However, for a dc microgrid with more than two buses connected in the form of a network with line impedances, such an algebraic expression cannot be a priori directly obtained. In [16] small-signal analysis is used to obtain the loadability of a microgrid with CPLs. However, system operating conditions like bus voltages and the power injected by the generator buses cannot be obtained near the maximum load point by such methods. A power-flow algorithm for a droop controlled DC microgrid is proposed in [17]. However employing the method in [17] to calculate loadability would involve repeated load-flow solutions. Further, in the case of a droop-controlled microgrid, the increased real power load is shared by all the generators depending on their droop resistances. Thus, there seems to be no method in the literature to address the following problems with regard to a working dc microgrid: 1) whether a planned load addition at a particular bus has the capability to cause voltage collapse, and 2) what is the stability margin after the load addition. The main contribution of this chapter is that of geometrically tracing the operating points of a droop-controlled dc microgrid with constant power loads (CPLs) when the load at one of the buses is varied. In this process, the maximum (real) power load that can be supplied at that bus is

obtained. The method proposed in this chapter incorporates the generalized circle diagram approach [18] into the power flow equations derived in [17]. Simulation results are provided to verify the proposed algorithm.

CHAPTER ORGANIZATION

Chapter 2 is organized as follows. In Section II, the passivity-based controller is described for a microgrid with parallel buck converters. Asymptotic stability of the equilibrium point obtained is verified using the Lyapunov method. To compensate for the voltage deviations due to the passivity-based primary or droop controller, a secondary controller which has an integral action [1] is considered. The equilibrium point obtained using the passivity-based control is shown to be locally asymptotically stable due to inherent system non-linearities. Hence, the necessary and the sufficient conditions to ensure the local asymptotic stability of the equilibrium points obtained using the primary and the overall (primary and secondary) controllers are derived in Section III. In section IV, simulation and experimental results are presented to verify the proposed control strategies.

Chapter 3 is organized as follows. In Section II, the passivity based controller is proposed for a microgrid with parallel boost converters. The equilibrium points and the droop characteristics of the proposed control laws are studied. The conditions to ensure the local asymptotic stability of the equilibrium points are derived in Section III. Simulation and experimental results are presented in Section IV to verify the proposed control strategies.

Chapter 4 is organized as follows. In Section II, a general methodology to the design of primary and secondary controllers for a dc microgrid containing non-isolated dc-dc converters is presented. In Section III, small-signal analysis and equivalent circuits

of the converters are used to obtain stability conditions for the equilibrium points derived in section II. Simulation and experimental results are presented in Section IV to verify the proposed control strategies. A microgrid containing paralleled buckboost converters is used to explain the proposed methodology and the results obtained for the three basic topologies of converters are compared.

Chapter 5 is organized as follows. In section II, linearization and small-signal analysis is used to derive the controller. The controller derived is applicable for a microgrid containing standalone versions of SEPIC, Cuk and Zeta converters supplying CPLs. In section III, stability conditions for equilibrium points are derived. Simulation and experiments on all three higher order converters supplying a CPL are used to verify the proposed control laws in section IV.

Chapter 6 is organized as follows. In section II, a short description of a droop-controlled DC microgrid with the various buses present and the system equations [17] are presented. Further, the generalized circle diagram approach [18] is reviewed briefly for easy understanding of the approach. In section III, the generalized circle diagram approach is modified to obtain the operating points of a DC microgrid. In section IV, simulation results are presented to validate the proposed approach.

Chapter 2: Autonomous Hierarchical Control of Microgrids with Constant-Power Loads-Part I DC-DC Buck Converters[1]

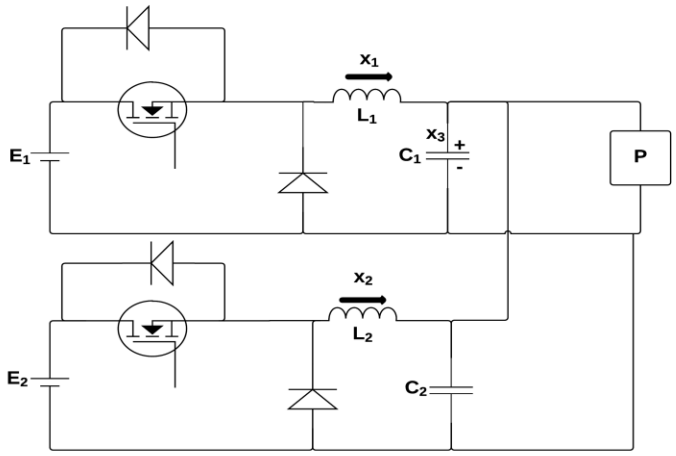

Figure. 4. A system of 2 parallel buck converters supplying a CPL.

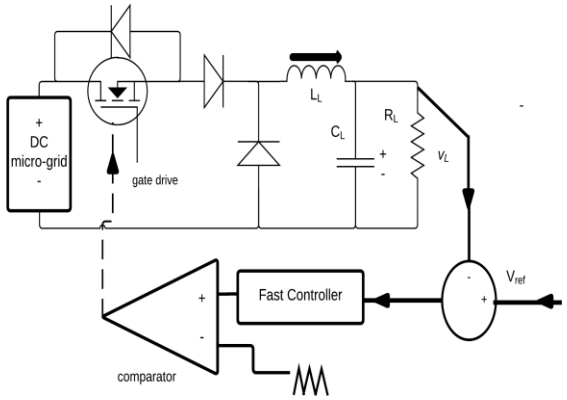

Figure. 5. Detailed diagram of a POL converter acting as CPL in Fig. 4. [18]

CONTROLLER DESIGN AND ANALYSIS

A system of 2 parallel connected buck converters supplying power to a CPL is shown in Fig. 4. Fig 5 represents a detailed diagram of the CPL in Fig. 4. Both the

[1] Contents of this chapter are published in "Autonomous Hierarchical Control of dc microgrids with Constant Power Loads" Proc. Applied Power Electronics Conference and Exposition (APEC) 2015, pp 2808-2815, where Mahesh Srinivasan is the first author

converters are assumed to be operating in continuous conduction mode (CCM). The average state space equation for the system is

$$\mathbf{f}(\mathbf{x},t)=\begin{cases} L_1\dfrac{dx_1}{dt}=d_1E_1-x_3 \\ L_2\dfrac{dx_2}{dt}=d_2E_2-x_3 \\ (C_1+C_2)\dfrac{dx_3}{dt}=x_1+x_2-\dfrac{P}{x_3} \end{cases} \qquad (1)$$
$$\mathbf{x}=[x_1,x_2,x_3]^T=[i_{L1},i_{L2},v_C]^T$$

where d_1 and d_2 refer to the instantaneous duty cycles of the top and bottom converters, respectively. Equation (1) can also be written as

$$\mathbf{M}\dot{\mathbf{x}}+(\mathbf{J}+\mathbf{R(x)})\mathbf{x}=\mathbf{dE} \qquad (2)$$

where

$$\mathbf{M}=\begin{bmatrix} L_1 & 0 & 0 \\ 0 & L_2 & 0 \\ 0 & 0 & C_1+C_2 \end{bmatrix}\mathbf{J}=\begin{bmatrix} 0 & 0 & 1 \\ 0 & 0 & 1 \\ -1 & -1 & 0 \end{bmatrix}\mathbf{E}=\begin{bmatrix} E_1 \\ E_2 \\ 0 \end{bmatrix}\mathbf{R(x)}=\begin{bmatrix} 0 & 0 & 0 \\ 0 & 0 & 0 \\ 0 & 0 & \left(\dfrac{P}{x_3^2}\right) \end{bmatrix}\mathbf{d}=\begin{bmatrix} d_1 & 0 & 0 \\ 0 & d_2 & 0 \\ 0 & 0 & 0 \end{bmatrix} \qquad (3)$$

Under open loop conditions, the system in Fig. 4 represents two ideal voltage sources connected to the dc microgrid. From (1), when the dc-dc converters operate in open loop with duty cycles D_{OL1} and D_{OL2} it is not possible to determine X_{1eq} and X_{2eq} which are the equilibrium values of x_1 and x_2, respectively. However, when sources are not considered to be ideal, X_{1eq}, X_{2eq} are decided by the internal impedance of the sources E_1 and E_2. Also, since the converters in Fig. 4 feed a CPL, the equilibrium point in open loop is unstable [17]. To overcome instabilities due to CPL and to enable current sharing among the different converters, the droop method is used. A simple current sharing scheme using a linear droop is represented in Fig. 6.

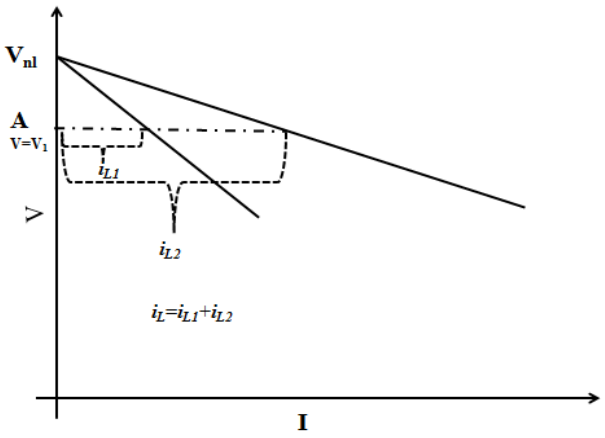

Figure. 6. A linear droop scheme

Consider that two voltage sources with voltage V_{nl} are connected in parallel feeding a load with current demand i_L. The current drawn from each source and the voltage at the common bus can be controlled by inserting resistances in series with the two voltage sources. In Fig. 6, for a total load demand of i_L, the common bus voltage reaches the point A drawing the currents i_{L1} and i_{L2} respectively from each source. However, the addition of resistances in series with the outputs of the converters in Fig. 4 would increase system losses. One way to introduce droop and to avoid system losses is to add virtual resistances through the control inputs d_1 and d_2 [38]. While the droop characteristic need not necessarily be linear as shown in Fig. 6, in the case of two buck converters connected in parallel, a linear droop is preferred for reasons that are explained at the end of this section. Consider again the system in Fig. 4 with virtual resistors R_{d1} and R_{d2} realized by controller action as if they were connected at the output of the buck converters. The buck converters are assumed to be replaced by ideal voltage sources of V_{nl} [42]. Thus, the system in Fig. 4 consists of 2 ideal voltage sources of V_{nl} connected in parallel through the resistances R_{d1} and R_{d2} to the dc microgrid. A constant power load P is connected at the dc microgrid. It must be noted that V_{nl} refers to the no-load voltage at

the dc microgrid. Now the equilibrium point with coordinates X_{1eq}, X_{2eq} and X_{3eq} is given by

$$\mathbf{X_{eq}} = \begin{bmatrix} X_{1eq} \\ X_{2eq} \\ X_{3eq} \end{bmatrix} = \begin{bmatrix} \frac{V_{nl} - \sqrt{V_{nl}^2 - 4PR_{d12}}}{2R_{d1}} \\ \frac{V_{nl} - \sqrt{V_{nl}^2 - 4PR_{d12}}}{2R_{d2}} \\ \frac{V_{nl} + \sqrt{V_{nl}^2 - 4PR_{d12}}}{2} \end{bmatrix} \tag{4}$$

where $V_{nl}^2 \geq 4PR_{d12}$ and $R_{d12}=R_{d1}||R_{d2}$. From (4), it can be observed that the load voltage is drooped linearly from V_{nl} to ($V_{nl}/2$) with a slope of R_{d1} and R_{d2} for the converters 1 and 2, respectively. When the system origin is moved to $\mathbf{X_{eq}}$ by writing

$$\tilde{\mathbf{x}} = \mathbf{x} - \mathbf{X_{eq}} \tag{5}$$

the system equation (2) becomes

$$\mathbf{M}\dot{\tilde{\mathbf{x}}} + (\mathbf{J} + \mathbf{R}(\tilde{\mathbf{x}}))\tilde{\mathbf{x}} = \mathbf{dE} - (\mathbf{J} + \mathbf{R}(\tilde{\mathbf{x}}))\mathbf{X_{eq}} \tag{6}$$

A virtual damping matrix $\mathbf{R_i}(\tilde{\mathbf{x}})$ is considered and a term $\mathbf{R_i}(\tilde{\mathbf{x}})\tilde{\mathbf{x}}$ is added on both the sides of (6) resulting in

$$\mathbf{M}\dot{\tilde{\mathbf{x}}} + (\mathbf{J} + \mathbf{R_t}(\tilde{\mathbf{x}}))\tilde{\mathbf{x}} = \mathbf{dE} - (\mathbf{J} + \mathbf{R}(\tilde{\mathbf{x}}))\mathbf{X_{eq}} + \mathbf{R_i}(\tilde{\mathbf{x}})\tilde{\mathbf{x}} \tag{7}$$

where

$$\mathbf{R_i}(\tilde{\mathbf{x}}) = \begin{bmatrix} R_{d1} & 0 & 0 \\ 0 & R_{d2} & 0 \\ 0 & 0 & \left(\frac{-P}{x_3^2}\right) \end{bmatrix} \mathbf{R_t} = \mathbf{R_i} + \mathbf{R} = \begin{bmatrix} R_{d1} & 0 & 0 \\ 0 & R_{d2} & 0 \\ 0 & 0 & 0 \end{bmatrix} \tag{8}$$

If the force free response of the system (7) is assumed [18] then the modified system can be defined from (7) as

$$\mathbf{M}\dot{\tilde{\mathbf{x}}} + (\mathbf{J} + \mathbf{R_t}(\tilde{\mathbf{x}}))\tilde{\mathbf{x}} = \mathbf{0} \tag{9}$$

If a candidate Lyapunov function $V(\tilde{\mathbf{x}})$ of the form

$$V(\tilde{\mathbf{x}}) = \frac{1}{2}\tilde{\mathbf{x}}^T \mathbf{M}\tilde{\mathbf{x}} \tag{10}$$

is chosen, then its time derivative is

$$\dot{V}(\tilde{\mathbf{x}}) = -R_{d1}\tilde{x}_1^2 - R_{d2}\tilde{x}_2^2 \tag{11}$$

From (11), it can be observed that

$$\left.\begin{aligned} &\dot{V}(\tilde{\mathbf{x}}) \le 0 \\ &\dot{V}(\tilde{\mathbf{x}}) = 0 \text{ if } \tilde{x}_1 = 0 \text{ and } \tilde{x}_2 = 0 \end{aligned}\right\} \tag{12}$$

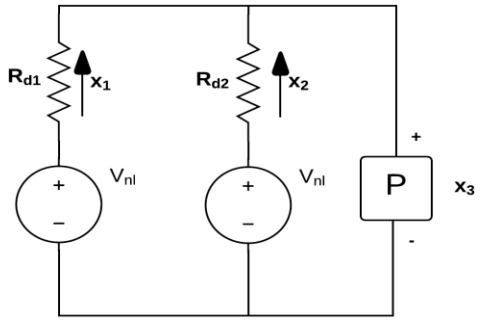

Figure. 7. Thevenin equivalent circuit of the dc micro-grid in Fig. 1 in steady state [42]

In addition, expanding (9) it can be observed that the largest invariant subset of the set where $\dot{V}(\tilde{\mathbf{x}}) = 0$ is the origin. Thus, by LaSalle invariance [66], the origin is an asymptotically stable equilibrium point for the system (9). Thus, the origin is asymptotically stable if the system (7) is assumed to be unforced. Hence, the control inputs are selected such that the right hand side of (7) becomes zero [18]. Then, the control inputs can be calculated from

$$\mathbf{dE} - \left(\mathbf{J} + \mathbf{R}(\tilde{\mathbf{x}})\right)\mathbf{X}_{\mathbf{eq}} + \mathbf{R}_{\mathbf{i}}(\tilde{\mathbf{x}})\tilde{\mathbf{x}} = \mathbf{0} \tag{13}$$

Thus,

$$\left.\begin{aligned} &d_1E_1 - X_{3eq} + \tilde{x}_1R_{d1} = 0 \\ &d_2E_2 - X_{3eq} + \tilde{x}_2R_{d2} = 0 \\ &\frac{V_{nl} - \sqrt{V_{nl}^2 - 4PR_{d12}}}{2R_{d12}} - \frac{P}{x_3} = 0 \end{aligned}\right\} \tag{14}$$

In (14), writing $\tilde{x}_1$ and $\tilde{x}_2$ in terms of x_1, x_2, X_{1eq} and X_{2eq} (5) and substituting for $\mathbf{X_{eq}}$ from (4) yields

$$d_1 = \frac{V_{nl} - R_{d1}x_1}{E_1}$$
$$d_2 = \frac{V_{nl} - R_{d2}x_2}{E_2} \tag{15}$$

The control inputs given by (15) are conveniently referred to as the primary control inputs d_{1p}, d_{2p} respectively. The Thevenin equivalent for the circuit in the Fig. 4 in the steady state with the control inputs (15) is given in Fig. 7. The reasons for considering a linear droop with respect to the parallel connected buck converters inductor current are

1. In a buck converter, the average current through the inductor is equal to the load current supplied by the converter. Thus, a linear droop in the inductor current is equivalent to a linear droop in the load current.
2. Placing virtual resistances in series with the inductors allows damping-out the oscillations caused by the CPL.

In steady state, the instantaneous duty ratios $d_1(t)$, $d_2(t)$ in (15)—obtained through a passivity based method in which virtual resistances are added at the output of the buck converters—represent the static droop lines. This can be observed by replacing (15) with their steady state values.

$$V_{\mu g} = V_{nl} - R_{d1}X_{1eq} = V_{nl} - R_{d2}X_{2eq},\ V_{\mu g} = X_{3eq} \tag{16}$$

In (16), $V_{\mu g}$ is the microgrid main bus voltage. The above observation can also be verified from Fig. 7.

3. The load is connected at the converters common point. Hence, the proportion of power shared by the converters is equal to the current sharing ratio.

Thus, this study demonstrates in an analytical way that the virtual droop resistance in series with the inductors serves two goals.

1. It enables current sharing between the converters.

2. It also damps the oscillations at the dc microgrid caused by the CPL and ensures that the equilibrium point given by (4) is asymptotically stable.

The method described above can be used to derive control inputs for *n* buck converters operating in parallel supplying a CPL.

The primary control inputs (15) enable current sharing at the cost of poor voltage regulation at the dc microgrid. This poor voltage regulation is a result of the voltage drop in the virtual droop resistances which can be remedied by adding the secondary control inputs (17) [38].

$$d_{1s} = \frac{k_i \int (V_{nl} - x_3) dt}{E_1}$$
$$d_{2s} = \frac{k_i \int (V_{nl} - x_3) dt}{E_2} \tag{17}$$

The overall control inputs are given by

$$d_1 = \frac{V_{nl} - x_1 R_{d1} + k_i \int (V_{nl} - x_3) dt}{E_1}$$
$$d_2 = \frac{V_{nl} - x_2 R_{d2} + k_i \int (V_{nl} - x_3) dt}{E_2} \tag{18}$$

The equilibrium point obtained with the control inputs (18) is given by

$$\mathbf{X_{eq}} = \begin{bmatrix} X_{1eq} \\ X_{2eq} \\ X_{3eq} \end{bmatrix} = \begin{bmatrix} \frac{P}{V_{nl}} \frac{R_{d2}}{R_{d1} + R_{d2}} \\ \frac{P}{V_{nl}} \frac{R_{d1}}{R_{d1} + R_{d2}} \\ V_{nl} \end{bmatrix} \tag{19}$$

From (19), it is evident that the secondary control inputs d_{1s}, d_{2s} ensure voltage regulation without affecting the current sharing ratio. The range of acceptable values of k_i to ensure the asymptotic stability of the equilibrium point (19) is derived in Section III.

PRACTICAL STABILITY OF THE EQUILIBRIUM POINTS

It should be noted that although the previous analysis seems to show that the equilibrium points indicated in (4) or (19) are globally asymptotically stable when using the proposed control inputs (15) and (18) respectively, these equilibrium points are in practice locally asymptotically stable. This observation is made because of the following non-linearities that exist in the system in the Fig. 4 [18].

1. The duty ratios d_1 and d_2 can only take values in the range $0 \leq d_1 \leq 1$ and $0 \leq d_2 \leq 1$.

2. In reality, the constant power behavior of an actual CPL is restricted above a threshold voltage, V_{lim}.Thus,

$$x_{ld} = \begin{cases} 0 \text{ if } x_3(t) < V_{\lim} \\ \dfrac{P}{x_3} \text{ if } x_3(t) \geq V_{\lim} \end{cases} \tag{20}$$

where x_{ld} is the instantaneous load current.

3. The system equations (1) are valid only if

$$\begin{aligned} x_1 \geq 0, x_2 \geq 0 \\ x_3 \geq \varepsilon \end{aligned} \tag{21}$$

where, ε is a small positive value . If the condition (21) is not met, then the system equations (1) have to be replaced by

$$\mathbf{f}(\mathbf{x},t) = \begin{cases} x_1 = 0 \text{ if } \dot{x}_1 < 0 \text{ and } x_1(0) = 0 \\ x_2 = 0 \text{ if } \dot{x}_2 < 0 \text{ and } x_2(0) = 0 \\ x_3 = \varepsilon \text{ if } \dot{x}_3 < 0 \text{ and } x_3(0) = \varepsilon \end{cases} \tag{22}$$

The conditions (22) are equivalent to the need for the inductor currents to be positive and the need for the capacitor voltages to be greater than ε.

4. The system of equations (1) are valid only in the continuous conduction mode. In discontinuous conduction mode (DCM), an additional term needs to be added to the inductor current equation [62]. However, it has also been mentioned in [18] that with practical circuit parameter values the DCM operation does not have a significant impact on the system trajectories.

To derive the necessary and sufficient conditions for the local asymptotic stability of the equilibrium points (4) and (19), the system of equations (1) is linearized and the jacobian of the linearized system, **A** is evaluated at each of the equilibrium points. Thus the matrix **A** is given by

$$\mathbf{A} = \left.\frac{\partial \mathbf{f}}{\partial \mathbf{x}}\right|_{\mathbf{x}=\mathbf{X}_{\mathbf{eq}}} \tag{23}$$

All the eigenvalues of the **A** matrix evaluated at each of the equilibrium points (4) and (19) need to lie on the left-half of the *s*-plane for the respective equilibrium points to be locally asymptotically stable.

Consider the system (1) with only the primary control inputs (15) applied. The characteristic polynomial for the **A** matrix is

$$\det(s\mathbf{I} - \mathbf{A}) = s^3 + a_2 s^2 + a_1 s + a_0 \tag{24}$$

Applying the necessary and sufficient conditions from the Routh stability criterion [67] for the local asymptotic stability of the equilibrium point indicated in (4)

$$a_2 > 0 \Rightarrow \frac{R_{d1}}{L_1} + \frac{R_{d2}}{L_2} > \frac{P}{(C_1 + C_2) X_{3eq}^2} \tag{25}$$

$$a_1 > 0 \Rightarrow \frac{L_1 + L_2 + R_{d1} R_{d2} (C_1 + C_2)}{R_{d2} L_1 + R_{d1} L_2} > \frac{P}{X_{3eq}^2} \tag{26}$$

$$a_0 > 0 \Rightarrow R_{d12} < \frac{X_{3eq}^2}{P} \tag{27}$$

$$a_2 a_1 - a_0 > 0 \Rightarrow \left\{ \begin{array}{l} \left[\frac{P^2}{X_{3eq}^4 (C_1 + C_2)^2} + \frac{R_{d1} R_{d2}}{L_1 L_2} \right] \left[\frac{R_{d2}}{L_2} + \frac{R_{d1}}{L_1} \right] + \frac{1}{(C_1 + C_2)} \left[\frac{R_{d2}}{L_2^2} + \frac{R_{d1}}{L_1^2} \right] \\ - \left[\frac{P}{X_{3eq}^2 (C_1 + C_2)} \left[\frac{R_{d2}}{L_2} + \frac{R_{d1}}{L_1} \right]^2 \right] - \left[\frac{P}{X_{3eq}^2 (C_1 + C_2)^2} \left[\frac{1}{L_1} + \frac{1}{L_2} \right] \right] \end{array} \right\} > 0 \tag{28}$$

The condition (27) is identical to the condition identified in [17] in which it has been shown that stability can be achieved in a dc micro-grid if the power dissipated by resistive loads is greater than that dissipated by the CPLs. However, in the presented controller, such resistive loads are virtual, so no real losses are introduced in the

operation of the microgrid. The conditions (25) and (26) imply that a stable equilibrium point can be ensured by inserting higher values of C and lower values of L in the converters [17].

The conditions for the local asymptotic stability of the equilibrium point given in (19) obtained by considering the overall control inputs (18) is derived. The characteristic polynomial for the **A** matrix is given by

$$\det\left(s\mathbf{I}-\mathbf{A}\right)=s^4+a_3s^3+a_2s^2+a_1s+a_0 \tag{29}$$

The increase in the system order by 1 in (29) is due to the presence of the integral term in the control inputs (18). From (29), the necessary conditions for the local asymptotic stability of the equilibrium point (19) can be derived using the Routh stability criterion [67]

$$a_3>0\Rightarrow\frac{R_{d1}}{L_1}+\frac{R_{d2}}{L_2}>\frac{P}{V_{nl}^2\left(C_1+C_2\right)} \tag{30}$$

$$a_2>0\Rightarrow\frac{1}{L_1(C_1+C_2)}+\frac{1}{L_2(C_1+C_2)}+\frac{R_{d1}R_{d2}}{L_1L_2}+\frac{P}{V_{nl}^2(C_1+C_2)}\left[\frac{-R_{d2}}{L_2}-\frac{R_{d1}}{L_1}\right]>0 \tag{31}$$

$$a_1>0\Rightarrow\frac{1}{(C_1+C_2)}\left[\frac{k_i}{L_2}+\frac{R_{d1}}{L_1L_2}+\frac{k_i}{L_1}+\frac{R_{d2}}{L_1L_2}-\frac{R_{d1}R_{d2}P}{L_1L_2V_{nl}^2}\right]>0 \tag{32}$$

$$a_0>0\Rightarrow\frac{k_i\left(R_{d1}+R_{d2}\right)}{L_1L_2(C_1+C_2)}>0 \tag{33}$$

$$a_3a_2-a_1>0\Rightarrow\left\{\begin{array}{c}\left[\frac{P^2}{(C_1+C_2)^2V_{nl}^4}+\frac{R_{d1}R_{d2}}{L_1L_2}\right]\left[\frac{R_{d2}}{L_2}+\frac{R_{d1}}{L_1}\right]+\frac{1}{(C_1+C_2)}\left[\frac{R_{d2}}{L_2^2}+\frac{R_{d1}}{L_1^2}\right]\\ -\left[\frac{P}{(C_1+C_2)V_{nl}^2}\left(\left[\frac{R_{d2}}{L_2}+\frac{R_{d1}}{L_1}\right]^2+\frac{1}{(C_1+C_2)}\left[\frac{1}{L_2}+\frac{1}{L_1}\right]\right)\right]\end{array}\right\}>\frac{k_i}{(C_1+C_2)}\left[\frac{1}{L_2}+\frac{1}{L_1}\right] \tag{34}$$

The conditions (33) and (32) are satisfied because R_{d1}, R_{d2}, and k_i are positive and the condition (27) is satisfied. The condition (30) implies that a stable equilibrium point can be ensured by inserting higher values of C and lower values of L in the converters [17].

SIMULATION AND EXPERIMENTAL RESULTS

Simulation results

To show the validity of the analysis, the circuit shown in Fig. 4 was simulated with the following parameters: E_1=35V, E_2=30V, C_1=C_2=1000μF, L_1=640 μH, L_2=630μH, V_{nl}=25.7V, P=100W, R_{d1}=2.075Ω, R_{d2}=1.709Ω. The open loop operation of the circuit with D_{OL1}=0.734, D_{OL2}=0.857 is shown in Fig. 8 from which it can be observed that x_1, x_2 and x_3 exhibit limit cycle oscillations at a frequency of 200Hz. The currents x_1 and x_2 exhibit limit cycle oscillations about the same average value of 1.946A since the sources E_1 and E_2 are assumed to be ideal. The primary controllers (15) are placed into operation at t=0.3s and the results are given in Fig. 9. It can be observed from Fig. 9 that x_1, x_2 and x_3 settle down at their equilibrium values of 2.12A, 2.58A and 21.3V respectively.

To show the validity of the analysis, the circuit shown in Fig. 4 was simulated with the following parameters: E_1=35V, E_2=30V, C_1=C_2=1000μF, L_1=640 μH, L_2=630μH, V_{nl}=25.7V, P=100W, R_{d1}=2.075Ω, R_{d2}=1.709Ω. The open loop operation of the circuit with D_{OL1}=0.734, D_{OL2}=0.857 is shown in Fig. 8 from which it can be observed that x_1, x_2 and x_3 exhibit limit cycle oscillations at a frequency of 200Hz. The currents x_1 and x_2 exhibit limit cycle oscillations about the same average value of 1.946A since the sources E_1 and E_2 are assumed to be ideal. The primary controllers (15) are placed into operation at t=0.3s and the results are given in Fig. 9. It can be observed from Fig. 9 that x_1, x_2 and x_3 settle down at their equilibrium values of 2.12A, 2.58A and 21.3V respectively. The output current sharing of the paralleled converters is ensured by the primary controller action. But this action also cause a voltage drop in the dc microgrid(25.7V to 21.3V). A secondary controller (17) with k_i=4.5 is added to the primary controller at t=0.5s to compensate for the voltage deviation. Fig. 10 shows the

waveforms of x_1, x_2 and x_3 when the secondary controller is inserted. It can be observed that x_3 rises to the no-load voltage level of 25.7V. The currents x_1 and x_2 decrease and settle down to equilibrium values of 1.76A and 2.13A respectively. Thus, the proposed secondary control not only increases the dc microgrid voltage to V_{nl} but also retains the same current sharing ratio as in the primary droop stage.

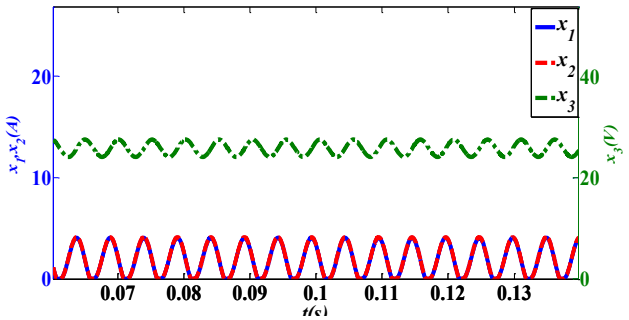

Figure. 8. Simulated results of x_1, x_2 and x_3 operating in open loop with fixed duty ratios

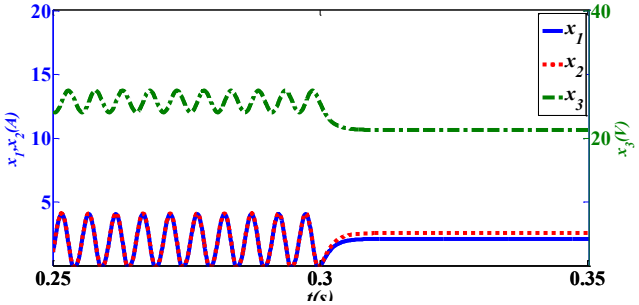

Figure. 9. Simulated results of x_1, x_2 and x_3 showing the transition from open-loop to the primary control mode

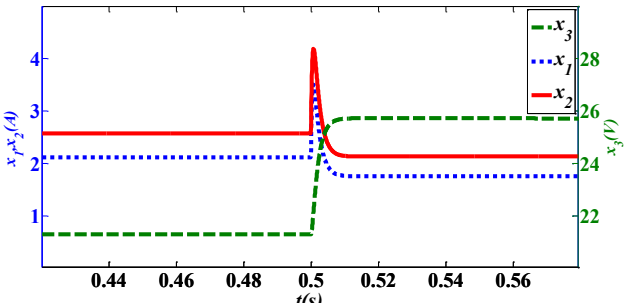

Figure. 10. Simulated results of x_1, x_2 and x_3 showing the transition from the primary control mode to the secondary control mode

Experimental results

The circuit parameters used in the experimental dc microgrid are the same as the simulation parameters. The parameters of the realized CPL are as follows. L_L=300μH, C_L=1680μF, V_L=16V, R_L=2.5Ω. Thus, the POL buck converter presents a CPL of about 100W to the dc microgrid. For sensing and feedback of the inductor currents, current sensing shunt resistors of 0.05Ω are placed in series with the inductors. The open loop behavior of the parallel connected converters is shown in the Fig. 11. As explained previously, the state variables exhibit limit cycle oscillations at around 200Hz. The steady state waveforms of x_1, x_2 and x_3 after adding the primary controller are shown in the Fig. 12 from which it can be observed that the dc microgrid voltage is reduced to 21.3V and the inductor currents x_1 and x_2 increase to 2.12A and 2.58A, respectively. The load currents are shared in the ratio X_{2eq}:X_{1eq}=1.22. The waveforms of x_1, x_2 and x_3 after adding the secondary controller with k_i=4.5 is shown in Fig. 13. It can be observed from Fig. 13 that the secondary control action has restored the voltage of the dc microgrid to 25.7V and the two load currents are reduce to X_{1eq}=1.81A and X_{2eq}=2.20A. The current-sharing ratio is maintained constant at X_{2eq}:X_{1eq}=1.22.

The dynamic behavior when the system transitions from open loop to primary droop control is shown in Fig. 14. As soon as the controller is switched on, the oscillations in the x_1, x_2 and x_3 are damped in 20ms and the voltage of the dc microgrid main bus is drooped, causing the load currents to increase. The dynamic behavior when the system changes from primary control only to added secondary control mode is shown in Fig. 15. As seen in the Fig. 15, the voltage increases to V_{nl} while the currents decrease and settle in about 20ms to their equilibrium values given by (19). Line and load regulation are ensured by the secondary control action. Fig. 16 verifies the load regulation. If the load at the experimental dc microgrid is increased from 100W to 120W

the state variable waveforms change as shown in Fig. 16. It can be observed that the dc microgrid voltage is maintained constant at 25.7V while both x_1 and x_2 increase to 2.11A and 2.56A respectively while still maintaining the same current sharing ratio than that in Figs. 12 and 13. To verify line regulation, E_1 is reduced from 35V to 30 V and the dynamic response is shown in the Fig.17. From Fig. 17, it can be observed that x_3 is maintained constant at V_{nl} while x_1 decreases to 1.1A and x_2 increases to 2.8A maintaining x_1+x_2 constant. It can be observed from Fig. 17 that x_1 and x_2 settle down to their new equilibrium values in about 120ms. Hence, the dynamics of the integral term are slower compared to those of the other terms in the controller. The experimental results are almost identical to the results obtained from the simulations.

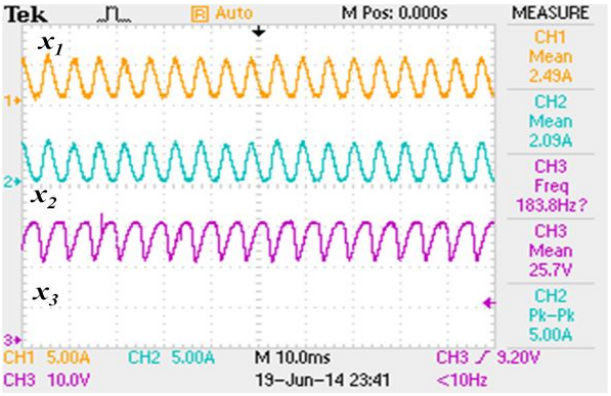

Figure. 11. Experimental results of x_1, x_2 and x_3 in open loop with fixed duty ratios

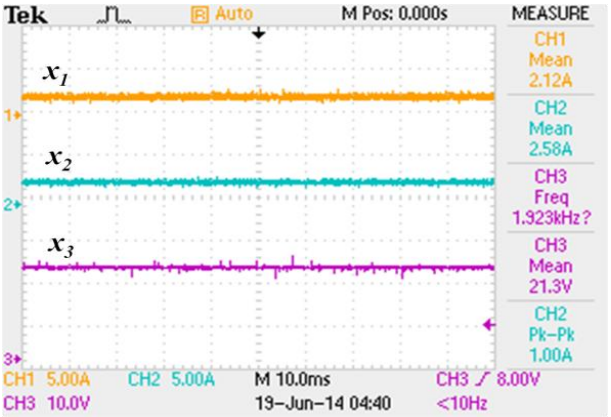

Figure. 12. Experimental results of x_1, x_2 and x_3 after primary droop control

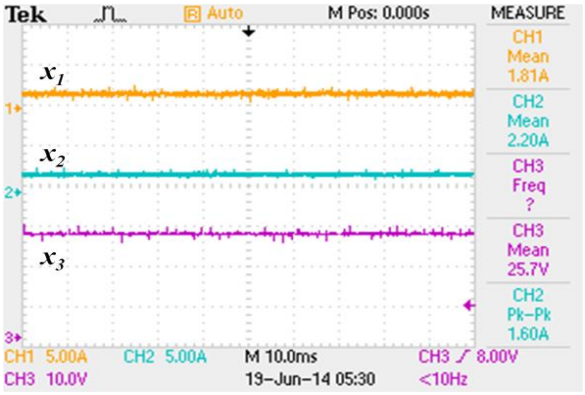

Figure. 13. Experimental results of x_1, x_2 and x_3 after secondary control

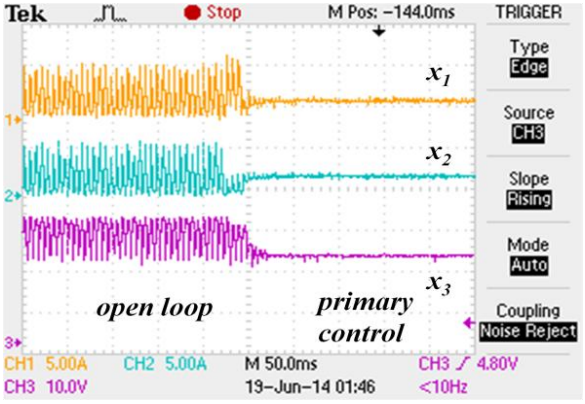

Figure. 14. Experimental results of x_1, x_2 and x_3 showing the dynamic response from open loop to primary droop control

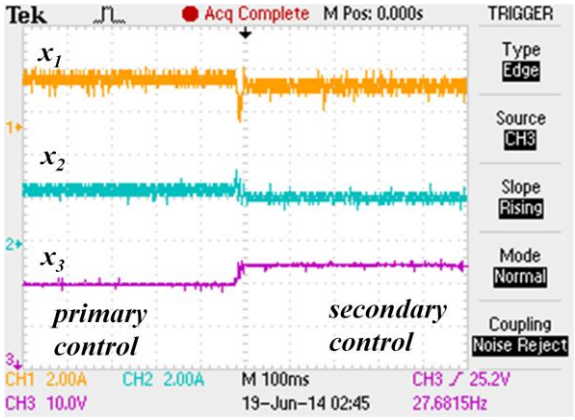

Figure. 15. Experimental results of x_1, x_2 and x_3 showing the dynamic response from primary droop control to secondary control mode

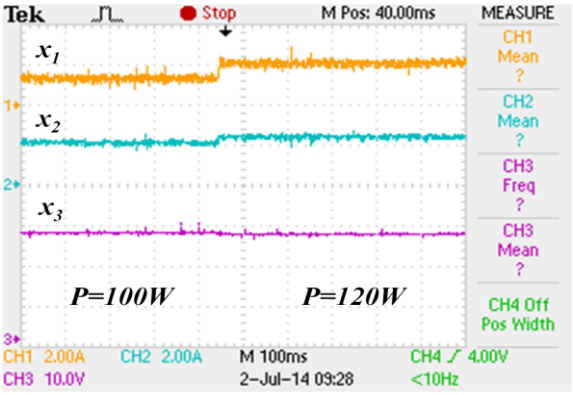

Figure. 16. Experimental waveforms of x_1, x_2 and x_3 showing the dynamic response for the load increase from 100W to 120W

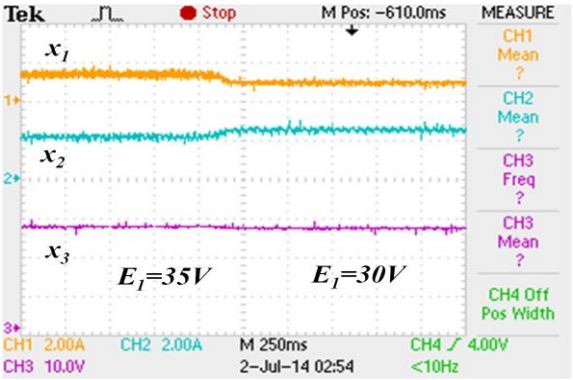

Figure. 17. Experimental waveforms of x_1, x_2 and x_3 showing the dynamic response when E_1 is decreased from 35V to 30V

SUMMARY

A passivity based approach is used to derive a distributed and autonomous control law for buck converters operating in parallel supplying a CPL. This approach yields a controller that adds virtual resistors as if they were in series with the buck converter inductors. The virtual resistances realized by control action enable current sharing among the paralleled converters as well as the stable operation of dc microgrid in the presence of CPL. In addition, the passivity based controller yields control laws that also represents the static droop characteristics in the steady state. Secondary controllers, consisting of integral terms are added to compensate for the voltage deviations due to the droop controller. Due

to inherent system non-linearities, the equilibrium points obtained are only locally asymptotically stable. The range of acceptable droop resistances and integral controller gains are derived using the Routh stability criteria. The analysis and the results are supported by simulations and experimental results.

Chapter 3: Autonomous Hierarchical Control of Microgrids with Constant-Power Loads-Part II DC-DC Boost Converters[2]

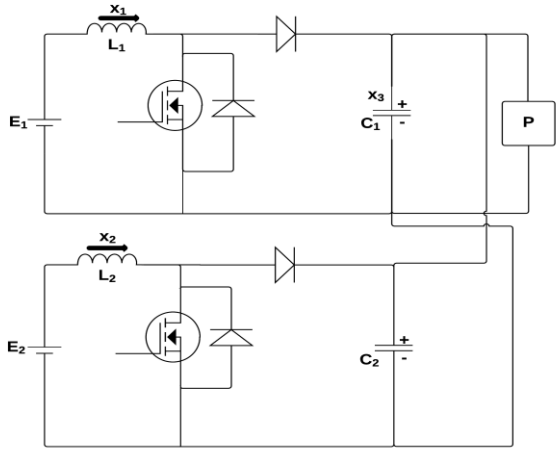

Figure. 18. A system of 2 parallel boost converters supplying a CPL.

CONTROLLER DESIGN AND ANALYSIS

A system of two parallel boost converters supplying a CPL is given in Fig. 18. The CPL in Fig. 18 is a buck converter whose output voltage is maintained at a constant value by a fast regulating PI controller. Since this buck converter regulates the voltage at the load, it is called point of load (POL) converter. Both the converters in Fig. 18 are assumed to be operating in continuous conduction mode (CCM). The average state equations for the system are given by

$$\mathbf{f}(\mathbf{x},t)=\begin{cases} L_1\dfrac{dx_1}{dt}=E_1-d_1^{'}x_3 \\ L_2\dfrac{dx_2}{dt}=E_2-d_2^{'}x_3 \\ (C_1+C_2)\dfrac{dx_3}{dt}=d_1^{'}x_1+d_2^{'}x_2-\dfrac{P}{x_3} \end{cases}$$
$$\mathbf{x}=[x_1,x_2,x_3]^T$$
$$d_1^{'}=1-d_1,\ d_2^{'}=1-d_2 \qquad (35)$$

[2]Contents of this chapter are published in "Decentralized Control of a Vehicular Microgrid with Constant Power Loads", Proc. IEEE Electric Vehicle Conference (IEVC), 2014, pp.1-8., where Mahesh Srinivasan is the first author

where d_1 and d_2 refer to the instantaneous duty cycles of the top and bottom converters, respectively. Equation (35) can also be written as

$$\mathbf{M}\dot{\mathbf{x}} + \left(\mathbf{J} + \mathbf{R}(\mathbf{x})\right)\mathbf{x} = \mathbf{E} \tag{36}$$

where

$$\mathbf{M} = \begin{bmatrix} L_1 & 0 & 0 \\ 0 & L_2 & 0 \\ 0 & 0 & (C_1 + C_2) \end{bmatrix} \mathbf{E} = \begin{bmatrix} E_1 \\ E_2 \\ 0 \end{bmatrix}$$

$$\mathbf{J} = \begin{bmatrix} 0 & 0 & d_1' \\ 0 & 0 & d_2' \\ -d_1' & -d_2' & 0 \end{bmatrix} \mathbf{R}(\mathbf{x}) = \begin{bmatrix} 0 & 0 & 0 \\ 0 & 0 & 0 \\ 0 & 0 & \left(\frac{P}{x_3^2}\right) \end{bmatrix} \tag{37}$$

Under ideal conditions, the circuit in the Fig. 18 represents 2 ideal transformers whose primary voltages are E_1 and E_2 respectively and their secondary terminals are connected in parallel at the vehicular dc microgrid [48]. It is desired that the sources E_1 and E_2 share their output currents in proportion to their respective power ratings. To achieve the objective of current sharing, the droop method is used because it does not require communication between converter modules and, thus, increases reliability by avoiding single points of failures. To obtain the locus of the microgrid voltage at equilibrium, X_{3eq} consider the equivalent circuit of the boost converter with the resistances connected at the secondary outputs as shown in Fig. 19. The values of the variable resistances connected at the output are given by

$$R_x = R_{d1} \frac{X_{3eq}^2}{E_1^2} \frac{1}{(1-k_1)} \tag{38}$$

$$R_y = R_{d2} \frac{X_{3eq}^2}{E_2^2} \frac{1}{(1-k_2)} \tag{39}$$

In (38) and (39), R_{d1} and R_{d2} are the droop resistances of the 2 converters respectively and k_1 and k_2 are the open loop duty ratios of the 2 converters such that

$$\frac{E_1}{1-k_1} = \frac{E_2}{1-k_2} = V_{nl} \tag{40}$$

Examining (38) and (39) closely, it can be observed that R_x and R_y represent R_{d1} and R_{d2} referred from the primary to the secondary of the transformers shown in Fig. 19. To obtain X_{3eq}, Kirchhoff current law is applied for the vehicular dc microgrid in Fig. 19. Once X_{3eq} is obtained, the loci of X_{1eq} and X_{2eq} can be obtained from

$$X_{1eq} = \frac{P}{V_{nl}} \frac{R_y}{(R_x + R_y)} \frac{1}{(1-k_1)} \tag{41}$$

$$X_{2eq} = \frac{P}{V_{nl}} \frac{R_x}{(R_x + R_y)} \frac{1}{(1-k_2)} \tag{42}$$

The reason for using (41) and (42) to obtain X_{1eq} and X_{2eq} instead of solving the circuit in Fig. 19 is that even though R_x and R_y represent actual resistances in the circuit, they are actually loss-free since voltage droop is realized using control action [38]. The equilibrium point with the coordinates X_{1eq}, X_{2eq} and X_{3eq} thus obtained is given by

$$\mathbf{X_{eq}} = \begin{bmatrix} X_{1eq} \\ X_{2eq} \\ X_{3eq} \end{bmatrix} = \begin{bmatrix} \dfrac{E_1^2 P R_{d2}}{E_1^3 R_{d2} + E_2^3 R_{d1}} \\ \dfrac{E_2^2 P R_{d1}}{E_1^3 R_{d2} + E_2^3 R_{d1}} \\ \dfrac{E_1^3 R_{d2} + E_2^3 R_{d1}}{P R_{d1} R_{d2} + E_1^2 (1-k_1) R_{d2} + E_2^2 (1-k_2) R_{d1}} \end{bmatrix} \tag{43}$$

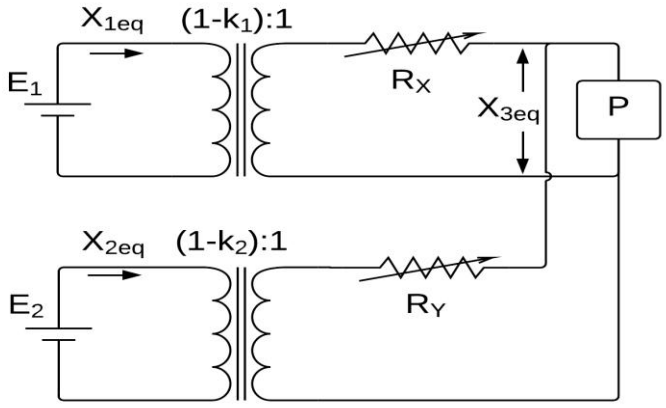

Figure. 19. Equivalent circuit of parallel connected boost converters used to obtain the locus of X_{3eq}

A change of coordinates from **x** to

$$\tilde{\mathbf{x}} = \mathbf{x} - \mathbf{X_{eq}} \tag{44}$$

applied to (36) yields

$$\mathbf{M}\dot{\tilde{\mathbf{x}}} + \left(\mathbf{J} + \mathbf{R}(\tilde{\mathbf{x}})\right)\tilde{\mathbf{x}} = \mathbf{E} - \left(\mathbf{J} + \mathbf{R}(\tilde{\mathbf{x}})\right)\mathbf{X_{eq}} \tag{45}$$

Consider now that a virtual damping matrix $\mathbf{R_i}(\tilde{\mathbf{x}})$ is defined by

$$\mathbf{R_i}(\tilde{\mathbf{x}}) = \begin{bmatrix} R_{d1} & 0 & 0 \\ 0 & R_{d2} & 0 \\ 0 & 0 & \left(\dfrac{-P}{x_3^2}\right) \end{bmatrix} \tag{46}$$

Next, a term $\mathbf{R_i}(\tilde{\mathbf{x}})\tilde{\mathbf{x}}$ is added on both the sides of (45), yielding

$$\mathbf{M}\dot{\tilde{\mathbf{x}}} + \left(\mathbf{J} + \mathbf{R_t}(\tilde{\mathbf{x}})\right)\tilde{\mathbf{x}} = \mathbf{E} - \left(\mathbf{J} + \mathbf{R}(\tilde{\mathbf{x}})\right)\mathbf{X_{eq}} + \mathbf{R_i}(\tilde{\mathbf{x}})\tilde{\mathbf{x}} \tag{47}$$

where

$$\mathbf{R_t} = \mathbf{R_i} + \mathbf{R} = \begin{bmatrix} R_{d1} & 0 & 0 \\ 0 & R_{d2} & 0 \\ 0 & 0 & 0 \end{bmatrix} \tag{48}$$

This step is equivalent to adding virtual damping resistors R_{d1} and R_{d2} in series with the inductors L_1 and L_2 in order to damp the oscillations due to the CPL and also cancel the

non-linearity in the state equation (36) [30]. Now, it is assumed that the system of equations (47) evolves unforced. Thus, the modified system can be defined from (47) as

$$\mathbf{M}\dot{\tilde{\mathbf{x}}} + \left(\mathbf{J} + \mathbf{R}_t(\tilde{\mathbf{x}})\right)\tilde{\mathbf{x}} = \mathbf{0} \tag{49}$$

If a candidate Lyapunov function $V(\tilde{\mathbf{x}})$ of the form

$$V(\tilde{\mathbf{x}}) = \frac{1}{2}\tilde{\mathbf{x}}^T\mathbf{M}\tilde{\mathbf{x}} \tag{50}$$

is chosen, then its time derivative is

$$\dot{V}(\tilde{\mathbf{x}}) = -R_{d1}\tilde{x}_1^2 - R_{d2}\tilde{x}_2^2 \tag{51}$$

From (51), it can be observed that

$$\left.\begin{array}{l} \dot{V}(\tilde{\mathbf{x}}) \le 0 \\ \dot{V}(\tilde{\mathbf{x}}) = 0 \text{ if } \tilde{x}_1 = 0 \text{ and } \tilde{x}_2 = 0 \end{array}\right\} \tag{52}$$

Additionally, expanding (49) it can be observed that the largest invariant subset of the set where $\dot{V}(\tilde{\mathbf{x}}) = 0$ is given by

$$\begin{aligned} d_1'\tilde{x}_3 &= 0 \\ d_2'\tilde{x}_3 &= 0 \end{aligned} \tag{53}$$

The condition $d_1 \neq 1$, $d_2 \neq 1$ is enforced for boost converters. Thus, (53) is satisfied if and only if $\tilde{x}_3 = 0$. Therefore, by LaSalle invariance [66], the origin is an asymptotically stable equilibrium point for the system (49). To obtain a stable controller design, the controller inputs are designed such that the right hand side of (47) becomes zero [30]. Then, equation (47) implies that

$$\mathbf{E} - \left(\mathbf{J} + \mathbf{R}(\tilde{\mathbf{x}})\right)\mathbf{X}_{\mathbf{eq}} + \mathbf{R}_i(\tilde{\mathbf{x}})\tilde{\mathbf{x}} = \mathbf{0} \tag{54}$$

Thus,

$$\left.\begin{array}{l} E_1 - d_1'X_{3eq} + \tilde{x}_1 R_{d1} = 0 \\ E_2 - d_2'X_{3eq} + \tilde{x}_2 R_{d2} = 0 \\ d_1'X_{1eq} + d_2'X_{2eq} - \dfrac{P}{x_3} = 0 \end{array}\right\} \tag{55}$$

From the first equation of (55),

$$d_1^{'} = \frac{E_1 + x_1 R_{d1} - X_{1eq} R_{d1}}{X_{3eq}} \tag{56}$$

Hence, from (43),

$$X_{3eq} = \frac{E_1^2}{(1-k_1)E_1 + R_{d1} X_{1eq}} \tag{57}$$

Substituting (57) in (56) and simplifying

$$d_1^{'} = \frac{\left((1-k_1)E_1^2 + R_{d1} X_{1eq} k_1 E_1 + R_{d1} x_1 (1-k_1) E_1 + R_{d1}^2 X_{1eq} x_1 - R_{d1}^2 X_{1eq}^2\right)}{E_1^2} \tag{58}$$

Consider

$$R_{d1}^2 X_{1eq} x_1 - R_{d1}^2 X_{1eq}^2 = R_{d1}^2 X_{1eq} \tilde{x}_1 \tag{59}$$

$$R_{d1} X_{1eq} k_1 E_1 + R_{d1} x_1 (1-k_1) E_1 = R_{d1} x_1 E_1 - R_{d1} \tilde{x}_1 k_1 E_1 \tag{60}$$

At a sufficiently closer point to the equilibrium, the terms containing perturbation of x_1 in the RHS of (59) and (60) can be neglected because they have opposite signs. Substituting (59) and (60) in (58) after neglecting the perturbation terms and simplifying, it yields d_1 in (61) which is the primary control input for the top converter in Fig. 18. Following similar steps, the primary control input for the bottom converter in Fig. 18 which is d_2 is obtained (61). Thus, the control inputs to the first or the primary stage are

$$\begin{aligned} d_1 &= \frac{k_1 E_1 - x_1 R_{d1}}{E_1}, 0 \le d_1 < 1, 0 \le k_1 < 1 \\ d_2 &= \frac{k_2 E_2 - x_2 R_{d2}}{E_2}, 0 \le d_2 < 1, 0 \le k_2 < 1 \\ \frac{E_1}{1-k_1} &= \frac{E_2}{1-k_2} = V_{nl} \end{aligned} \tag{61}$$

Even though the passivity based approach suggests global asymptotic stability of the equilibrium point (43) obtained using the control inputs (61), the equilibrium point (43) is only locally asymptotically stable. This is due to the approximation made by neglecting the perturbation terms in (59) and (60) and also because of the limitations in the duty cycle inputs (61). Since from (43)

$$\frac{X_{1eq}}{X_{2eq}} = \frac{E_1^2 R_{d2}}{E_2^2 R_{d1}} \tag{62}$$

the following observations can be made regarding the primary control inputs:

1. The primary control inputs enable current sharing among the converters as it is evident from (62).
2. The primary control inputs also enable damping out the oscillations due to the CPL and ensures local asymptotic stability of the equilibrium point indicated in (43).
3. A plot of X_{1eq} and X_{2eq} vs X_{3eq} for varying values of P is given in Fig. 20. As observed in this figure, the droop characteristics are nonlinear. However the slopes of the characteristics are dependent on R_{d1} and R_{d2}. The range of the voltage droop equals the difference between V_{nl} and E_g where E_g is the greater value among E_1 and E_2. For an arbitrary load power, P_1, the voltage at the dc vehicular microgrid reaches V_1 (point A in Fig. 20). The lengths of the segments AB and AC represent I_{L2} and I_{L1}, respectively, where I_{L2} and I_{L1} represent X_{2eq} and X_{1eq} at the load power P_1

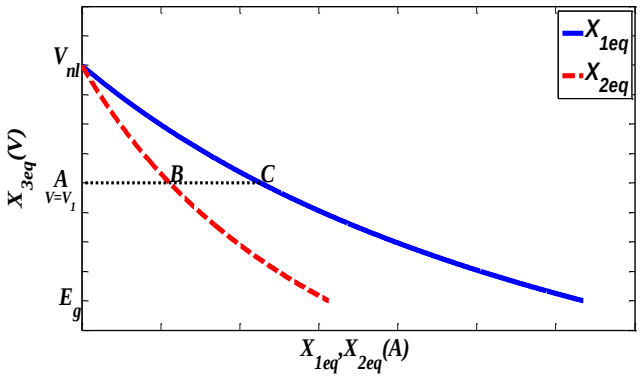

Figure. 20. X_{1eq} and X_{2eq} Vs X_{3eq} for varying P

The primary control inputs (61) ensure acceptable current sharing among the paralleled boost converters. But, this leads to unacceptable voltage regulation at the dc main bus. To

ensure that this voltage stays within acceptable limits, secondary control inputs in the form of integral control terms are added to the primary control inputs. Thus, the overall control inputs are given by

$$d_1 = \frac{k_1 E_1 - x_1 R_{d1} + k_i E_1^2 \int (V_{nl} - x_3) dt}{E_1}$$
$$d_2 = \frac{k_2 E_2 - x_2 R_{d2} + k_i E_2^2 \int (V_{nl} - x_3) dt}{E_2} \tag{63}$$

where k_i is the integral controller gain. The equilibrium point associated with the overall control inputs (63) is given by

$$\mathbf{X_{eq}} = \begin{bmatrix} X_{1eq} \\ X_{2eq} \\ X_{3eq} \end{bmatrix} = \begin{bmatrix} \frac{E_1^2 P R_{d2}}{E_1^3 R_{d2} + E_2^3 R_{d1}} \\ \frac{E_2^2 P R_{d1}}{E_1^3 R_{d2} + E_2^3 R_{d1}} \\ V_{nl} \end{bmatrix} \tag{64}$$

Thus, the secondary control input in (63) ensures that the input currents from the sources E_1 and E_2 are maintained at the same value as in the primary control stage (43) whereas from (64) the dc microgrid voltage is raised to $V_{nl.}$ The overall control inputs (63) contain integral control terms. For the equilibrium point (64) obtained after inserting the control inputs (63) to be locally asymptotically stable, the integral controller gain k_i has to be chosen sufficiently small. Under such conditions, the dynamics at the integral controller do not interfere with the dynamics due to the primary controllers (61). Thus, local asymptotic stability of the equilibrium point (64) is practically maintained [30].

STABILITY ANALYSIS

To arrive at the necessary conditions for local asymptotic stability of the equilibrium points (43) and (64), the proposed control inputs (61) and (63) are applied to the system represented by (35). The Jacobian of the system (35), **A**, given by

$$\mathbf{A} = \left.\frac{\partial \mathbf{f}}{\partial \mathbf{x}}\right|_{\mathbf{x}=\mathbf{X}_{\mathbf{eq}}} \tag{65}$$

is evaluated at each of the equilibrium point given in (43) and (64) in order to determine whether all the eigenvalues of **A** lie on the left-half of the *s*-plane. Consider the system (35) with only the primary control inputs (61) applied. The characteristic polynomial for the **A** matrix is

$$\det(s\mathbf{I}-\mathbf{A}) = s^3 + a_2 s^2 + a_1 s + a_0 \tag{66}$$

Applying the necessary conditions from the Routh stability criterion [67] for the local asymptotic stability of the equilibrium point indicated in (43) yields

$$a_2 > 0 \Rightarrow X_{3eq}^3 \left[\frac{R_{d2}}{L_2 E_2} + \frac{R_{d1}}{L_1 E_1}\right] > \frac{P}{C_1 + C_2} \tag{67}$$

$$a_1 > 0 \Rightarrow \begin{cases} \dfrac{1}{(C_1+C_2)}\left[\begin{array}{l} \dfrac{(1-k_2)^2}{L_2} + \dfrac{3(1-k_2)X_{2eq}R_{d2}}{L_2E_2} + \dfrac{2X_{2eq}^2 R_{d2}^2}{L_2 E_2^2} + \\ \dfrac{(1-k_1)^2}{L_1} + \dfrac{3(1-k_1)X_{1eq}R_{d1}}{L_1E_1} + \dfrac{2X_{1eq}^2 R_{d1}^2}{L_1 E_1^2} \end{array}\right] + \\ \dfrac{X_{3eq}^2 R_{d1} R_{d2}}{L_1 L_2 E_1 E_2} > \dfrac{P}{(C_1+C_2)X_{3eq}}\left(\dfrac{R_{d1}}{L_1E_1} + \dfrac{R_{d2}}{L_2E_2}\right) \end{cases} \tag{68}$$

$$a_0 > 0 \Rightarrow \begin{cases} \dfrac{X_{3eq}R_{d1}(1-k_2)^2}{E_1} + \dfrac{X_{3eq}R_{d2}(1-k_1)^2}{E_2} + \dfrac{3X_{3eq}X_{2eq}R_{d1}R_{d2}(1-k_2)}{E_1E_2} \\ + \dfrac{2X_{3eq}R_{d1}X_{2eq}^2R_{d2}^2}{E_1E_2^2} + \dfrac{3X_{3eq}X_{1eq}R_{d1}R_{d2}(1-k_1)}{E_1E_2} + \dfrac{2X_{3eq}R_{d2}X_{1eq}^2R_{d1}^2}{E_1^2E_2} > \dfrac{R_{d1}R_{d2}P}{E_1E_2} \end{cases} \tag{69}$$

The condition (67) can be satisfied qualitatively by choosing higher values for the capacitances and lower values for the inductances [17]. Next, the conditions for the local asymptotic stability of the equilibrium point given in (64) obtained by considering both

the primary and the secondary control inputs (63) are derived. The characteristic polynomial for the **A** matrix is given by

$$\det(s\mathbf{I}-\mathbf{A}) = s^4 + a_3 s^3 + a_2 s^2 + a_1 s + a_0 \tag{70}$$

From (70), the necessary conditions for the local asymptotic stability of the equilibrium point (64) can be derived using the Routh stability criterion [67]

$$a_3 > 0 \Rightarrow V_{nl}^3 \left[\frac{R_{d1}}{L_1 E_1} + \frac{R_{d2}}{L_2 E_2} \right] > \frac{P}{(C_1 + C_2)} \tag{71}$$

$$a_2 > 0 \Rightarrow \begin{cases} \dfrac{1}{(C_1+C_2)} \left[\dfrac{(1-k_2)^2}{L_2} + \dfrac{(1-k_1)^2}{L_1} \right] + \dfrac{1}{(C_1+C_2)} \left[\dfrac{X_{2eq} R_{d2} (1-k_2)}{L_2 E_2} + \dfrac{X_{1eq} R_{d1} (1-k_1)}{L_1 E_1} \right] \\ + \dfrac{V_{nl}^2 R_{d1} R_{d2}}{L_1 L_2 E_1 E_2} > \dfrac{k_i P}{(C_1+C_2)} + \dfrac{P}{V_{nl}(C_1+C_2)} \left[\dfrac{R_{d1}}{L_1 E_1} + \dfrac{R_{d2}}{L_2 E_2} \right] \end{cases} \tag{72}$$

$$a_1 > 0 \Rightarrow \begin{cases} \dfrac{V_{nl}}{L_1 L_2} \left[\dfrac{R_{d1}(1-k_2)^2}{E_1} + \dfrac{R_{d2}(1-k_1)^2}{E_2} \right] + k_i V_{nl} \left[\dfrac{(1-k_2)E_2 + X_{2eq} R_{d2}}{L_2} + \dfrac{(1-k_1)E_1 + X_{1eq} R_{d1}}{L_1} \right] \\ + \dfrac{V_{nl} R_{d1} R_{d2}}{L_1 L_2 E_1 E_2} \left[X_{2eq}(1-k_2) + X_{1eq}(1-k_1) \right] > k_i P V_{nl} \left[\dfrac{R_{d1}}{L_1 E_1} + \dfrac{R_{d2}}{L_2 E_2} \right] + \dfrac{R_{d1} R_{d2} P}{L_1 L_2 E_1 E_2} \end{cases} \tag{73}$$

$$a_0 > 0 \Rightarrow \left\{ \frac{R_{d1}(1-k_2)E_2 + R_{d1} R_{d2} X_{2eq}}{E_1} + \frac{R_{d2}(1-k_1)E_1 + R_{d1} R_{d2} X_{1eq}}{E_2} > \frac{R_{d1} R_{d2} P}{E_1 E_2} \right. \tag{74}$$

The condition (71) is satisfied because $V_{nl} \geq X_{3eq}$ Hence, (67) is satisfied. The condition (71) suggests that by inserting larger values of capacitances and smaller values of inductances, a stable operating point can be achieved with the overall control inputs (63).

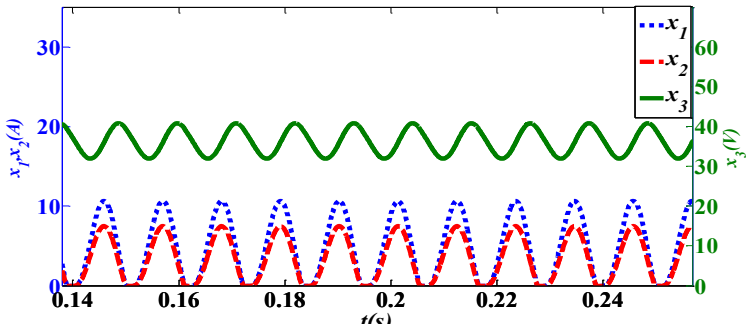

Figure. 21. Simulated results of x_1, x_2 and x_3 operating in open loop with fixed duty ratios

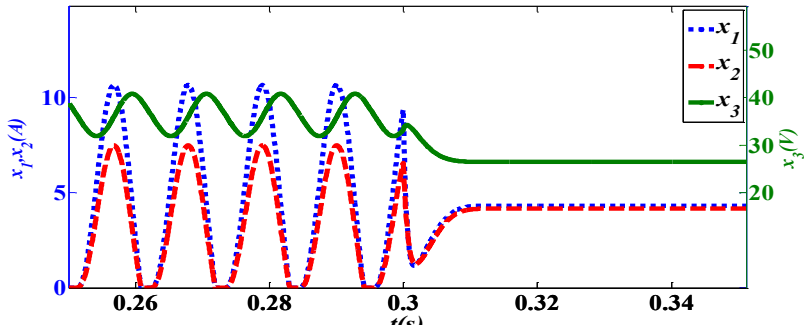

Figure. 22. Simulated results of x_1, x_2 and x_3 showing the transition from open-loop to the primary control mode

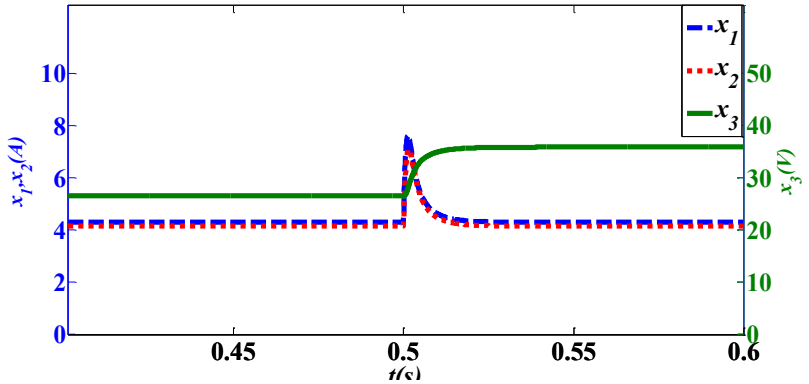

Figure. 23. Simulated results of x_1, x_2 and x_3 showing the transition from the primary control mode to the secondary control mode

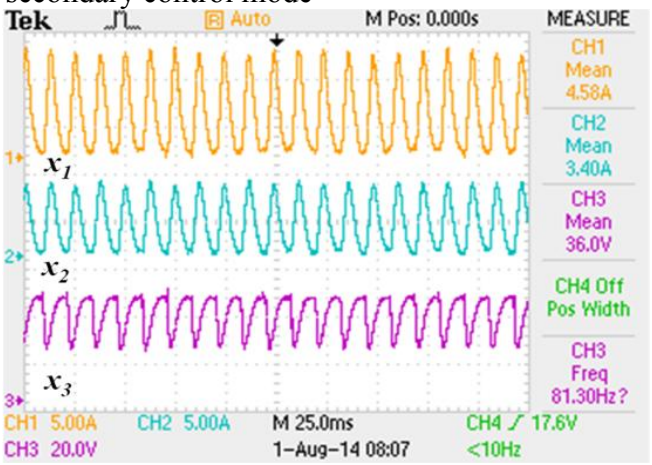

Figure. 24. Experimental results of x_1, x_2 and x_3 in open loop with fixed duty ratios

SIMULATION AND EXPERIMENTAL RESULTS

Simulation results

To show the validity of the analysis, the circuit shown in Fig. 18 was simulated with the following parameters. E_1=20V, E_2=15V, C_1=C_2=940μF, L_1=730μH, L_2=780μH, V_{nl}=36V, P=150W, k_1=0.444, k_2=0.583, R_{d1}=0.929Ω and R_{d2}=0.541Ω. It is desired that the input currents supplied by the sources E_1 and E_2 are shared in the ratio given by (62). Initially, the circuit is operated in open loop with the open loop duty ratios D_1=0.444 and D_2=0.583 respectively. The results are shown in the Fig. 21. From Fig. 21, it can be observed that the waveforms of x_1, x_2 and x_3 exhibit limit cycle oscillations at a frequency of 90Hz. To damp the oscillations due to the CPL and to enable current sharing among the converters, virtual resistances R_{d1} and R_{d2} are inserted in the form of the control inputs (61) at t=0.3s. It can be observed from the Fig. 22 that x_1, x_2 and x_3 settle down at their equilibrium values of 4.29A, 4.14A and 26.5V respectively.

It should be noted that even though the primary controllers enable current sharing among the parallel connected converters, the voltage regulation at vehicular dc microgrid main bus (36V to 26.5V) could be considered unacceptable for many applications. To raise the voltage of the vehicular microgrid to the nominal value of V_{nl}, a secondary controller with k_i=0.01 is added to the primary control inputs at t=0.5s. The overall control inputs are given by (63). Fig. 23 shows the waveforms of x_1, x_2 and x_3 when the secondary controller is added. It can be observed that the voltage at the vehicular microgrid is raised to V_{nl} whereas the currents x_1 and x_2 are maintained at the same value as in the primary control stage.

Experimental results

The circuit parameters used during the experiment representing a vehicular dc microgrid are the same as the simulation parameters. The parameters of the realized CPL are: L_L=450μH, C_L=1680μF, V_L=21.3V and R_L=3Ω where L_L, C_L, V_L and R_L refer to the inductor, capacitor, output voltage and the load resistor values of the POL buck converter respectively. For sensing and feedback of the inductor currents, current sensing shunt resistors of 0.05Ω are placed in series with the inductors. Initially, the circuit is operated in open loop with the open loop duty ratios D_1=0.444 and D_2=0.583. From the results shown in the Fig. 24, it can be observed that the waveforms of x_1, x_2 and x_3 exhibit limit cycle oscillations with a frequency of about 90Hz. The currents x_1 and x_2 exhibit limit cycle oscillations about the average values of 4.58A and 3.40A respectively which is dependent on the internal impedance of the sources E_1 and E_2.

After adding the primary controller, the waveforms of x_1, x_2 and x_3 are shown in Fig. 25. From this figure, it can be observed that the voltage of the vehicular dc microgrid is reduced to 26.5 V and the inductor currents settle down at 4.25A and 4.12A respectively. The current sharing and the voltage reduction at the dc microgrid described above represents the addition of virtual droop resistances of R_{d1}=0.929Ω and R_{d2}=0.541Ω. The input currents are shared in the ratio given by (62). To restore the voltage back to V_{nl}, secondary controllers with k_i=0.01 are added. The waveforms of x_1, x_2 and x_3 after adding the secondary controller is shown in the Fig. 26. It can be observed from the Fig. 26 that the secondary control action has restored the voltage of the vehicular dc microgrid bus to 36V and the two input currents remain nearly in the same value of x_1=4.29A and x_2=4.14A as in the primary control stage. Thus the current sharing ratio is maintained constant and based on (62).Transition from open loop to primary droop control is shown in Fig. 27. As soon as the controller is switched on, the

oscillations in x_1, x_2 and x_3 are damped in 40ms, the voltage of the dc microgrid main bus is drooped, and the load currents settle down to their equilibrium values given by (43). Transition from the primary control mode to the secondary control mode is shown in Fig. 28. As seen in Fig. 28, the voltage increases to V_{nl} while the currents settle down at the same values as in the primary droop stage in about 100ms. The secondary controllers in (63) provide line and load regulation. To verify line regulation, E_2 is increased from 15V to 20 V. Figure. 29 shows the response when E_2 is increased. It can be observed that while x_3 is maintained constant at 36V, x_1 decreases to 2.1A and x_2 increases to 5.4A. The inductor currents settle down at their new equilibrium values in about 125ms. To test load regulation, the CPL was increased from 150W to 200W and the results are shown in Fig. 30. From Fig. 30, it can be observed that x_1 and x_2 settle down at 5.74A and 5.58A respectively maintaining the same ratio as in the primary and secondary control stages. The vehicular microgrid voltage, x_3 remains unchanged at 36V.

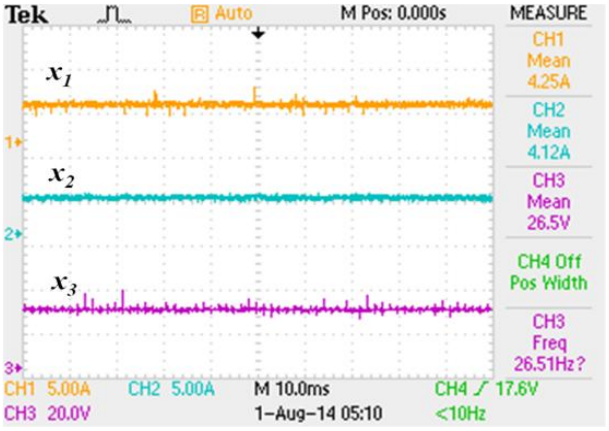

Figure. 25. Experimental results of x_1, x_2 and x_3 after primary droop control

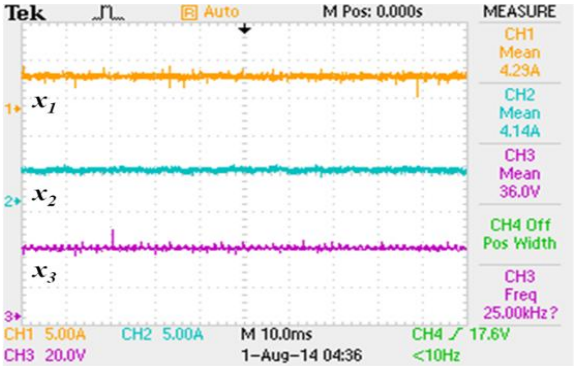

Figure. 26. Experimental results of x_1, x_2 and x_3 after secondary control

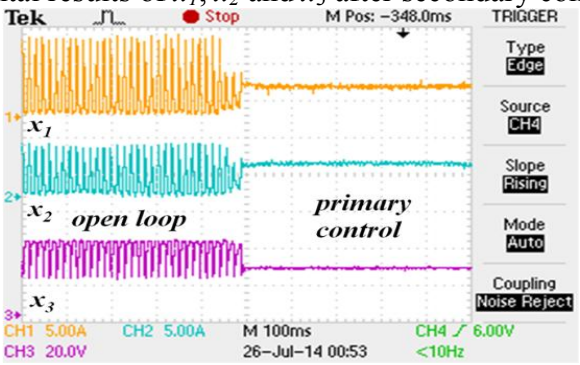

Figure. 27. Experimental results of x_1, x_2 and x_3 showing the dynamic response from open loop to primary droop control

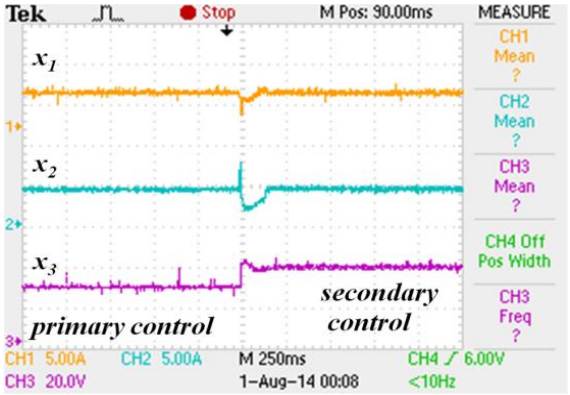

Figure. 28. Experimental results of x_1, x_2 and x_3 showing the dynamic response from primary droop control to secondary control mode

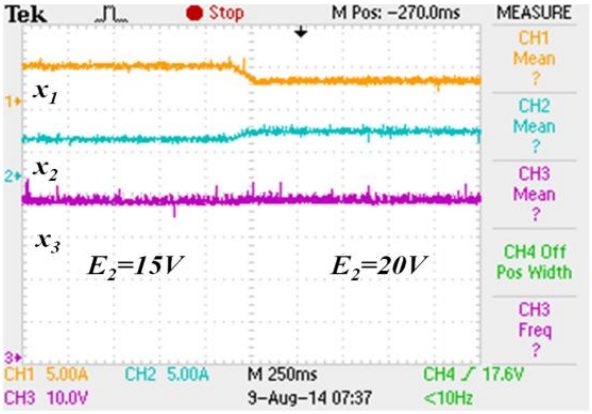

Figure. 29. Experimental waveforms of x_1, x_2 and x_3 showing the dynamic response when E_2 is increased from 15V to 20V

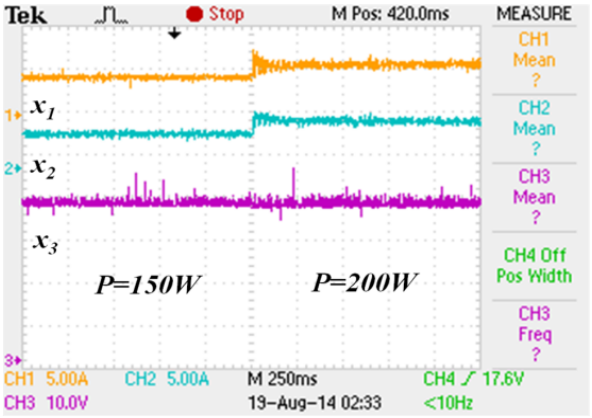

Figure. 30. Experimental waveforms of x_1, x_2 and x_3 showing the dynamic response when P is increased from 150W to 200W

SUMMARY

The concept of autonomous control of a dc microgrid is extended to an automotive power system. A passivity based controller is proposed in order to design the autonomous control of an automotive power system consisting of parallel connected boost converters supplying a CPL. The approach involves the addition of virtual resistances as a part of the control law. The virtual resistances added enable the realization of a non-linear droop of

the vehicles' main bus voltage with respect to the converters input currents. The virtual resistances added not only enable the current sharing among the converters but also damp out the oscillations at the main bus caused by CPLs. To compensate for the voltage deviations due to the droop controller, secondary control terms consisting of integral controllers are added. Although passivity based analysis suggests global asymptotic stability, the equilibrium points obtained are only locally asymptotically stable due to the duty cycle limitations. The conditions to ensure the local asymptotic stability of the equilibrium points are derived. The proposed controller is verified with simulation and experimental results.

Chapter 4: A Semi-Autonomous Hierarchical Control Scheme for DC Microgrids with Constant Power Loads

CONTROLLER DESIGN AND ANALYSIS

A system of *m* parallel-connected converters supplying power to CPLs is shown in Fig. 31 [68]. The CPLs in Fig. 31 may be dc-dc converters whose output voltage is maintained constant by fast-regulating PI controllers [18] or they may be batteries in regulated charging mode [20]. They can also be inverter-fed drives, whose output characteristic consists of a single value of output torque corresponding to a single value of speed [19]. The source converters in Fig. 31 are assumed to be operating in continuous conduction mode (CCM). The average state equations for such a system can be given as follows.

$$\begin{aligned} \mathbf{f}(\mathbf{x},t) &= \begin{cases} f_1(\mathbf{x},\mathbf{E},P,\mathbf{d}) \\ f_2(\mathbf{x},\mathbf{E},P,\mathbf{d}) \\ \vdots \\ f_n(\mathbf{x},\mathbf{E},P,\mathbf{d}) \end{cases} \\ P &= P_1 + P_2 ..... + P_r \\ \mathbf{d} &= \left[d_1, d_2, \ldots d_m\right]^T, \mathbf{E} = \left[E_1, E_2, \ldots E_m\right]^T, \mathbf{x} = \left[x_1, x_2, \ldots x_n\right]^T \end{aligned} \tag{75}$$

where x is the vector of state variables in the system which are the inductor currents and capacitor voltages. If the source converters in Fig. 31 consist of converters of simple topology, then $n=m+1$. The instantaneous duty cycle and source voltage of i^{th} converter are given by d_i and E_i respectively.

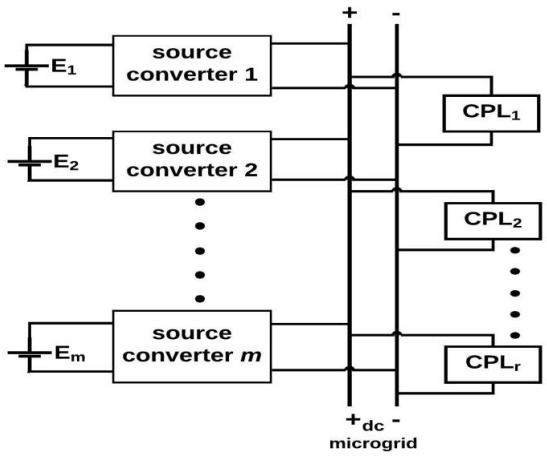

Fig. 31. A dc microgrid with *m* parallel source converters supplying CPLs[68]

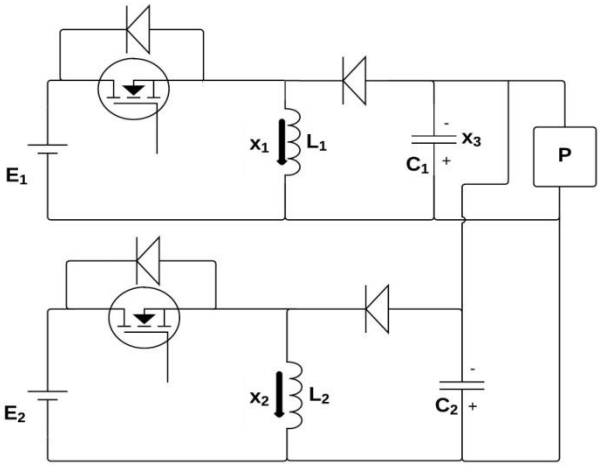

Fig. 32. A system of 2 parallel buckboost converters supplying a CPL.

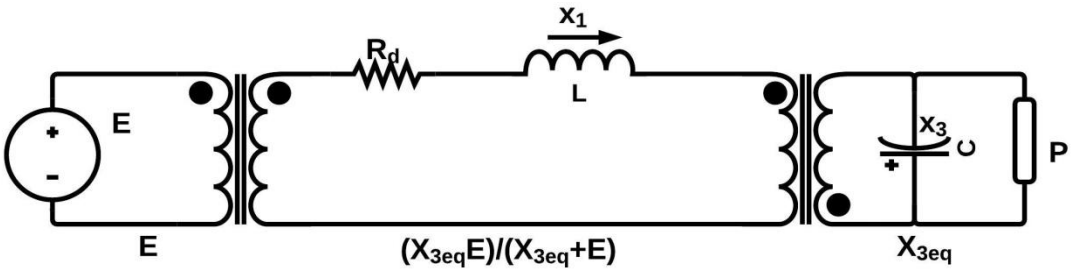

Fig. 33. Equivalent circuit of top buckboost converter in Fig. 32 supplying a CPL.[69]

By lumping together all the CPLs in (75), the damping provided by transmission line resistances in the microgrid is removed and stability of equilibrium point can be obtained

purely in terms of droop resistances realized through controller action. For the stable and efficient operation of a dc microgrid, it is necessary to ensure that oscillations induced by CPLs is properly damped. In addition, the currents supplied by the various sources should be proportional to their respective power ratings. In order to ensure proper current sharing and stable operation of source converters, consider the vector of duty cycles, **d** in (75) to involve feedback of state variables. Let

$$\mathbf{d} = \mathbf{g}(\mathbf{x}) \tag{76}$$

It is important that the chosen state feedback maintains the stability of the corresponding equilibrium point, $\mathbf{X_{eq}}$. Since the system equations (75) are non-linear, stability of $\mathbf{X_{eq}}$ is estimated by linearizing the equations about the equilibrium point [67]. This is done as follows. The duty cycle expressions (76) are substituted in the system equations (75). Then the expression for the linearized system jacobian **A** which is given by

$$\mathbf{A} = \left.\frac{\partial \mathbf{f}}{\partial \mathbf{x}}\right|_{\mathbf{x}=\mathbf{X_{eq}}} \tag{77}$$

is calculated. Observing the structure of the **A** matrix (77) helps in deriving the primary control law. In particular, the following criterion is applied to derive primary control law.

$$\text{trace}(\mathbf{A}) < 0 \tag{78}$$

In addition, autonomy of primary controllers is also taken into account while deriving primary control laws. It will be shown that, for an m parallel converter case, primary control input of q^{th} parallel converter, $d_{q,p}$ is given by

$$d_{q,p} = \frac{k_q E_q - x_{Lq} R_{dq}}{E_q} \tag{79}$$

where k_q, E_q, R_{dq} are no-load duty ratio, source voltage and virtual droop resistance of the q^{th} converter respectively. The variable x_{Lq} corresponds to inductor current of the q^{th} converter. The vector of primary control inputs is referred to as $\mathbf{d_p}$. Thus

$$\mathbf{d_p} = \left[d_{1p}, d_{2p}.....d_{mp} \right]^T \tag{80}$$

In order to obtain the primary equilibrium point, the control inputs (80) need to be substituted in the system equations (75). The variables $x_1 \ldots x_n$ are replaced by $X_{1eq} \ldots X_{neq.}$ The equilibrium point obtained is given by $\mathbf{X_{eq,pri}}$. As an example, consider the case of two parallel buckboost converters supplying a CPL as shown in Fig. 32. The equivalent circuit of top buck boost converter in Fig. 32 is given in Fig. 33 [69]. Parallel buck and parallel boost configurations have been analyzed in [70] and [71] respectively. The simplest case of two parallel buckboost converters is considered without loss of generality. The average state space equation for the system is

$$\mathbf{f}(\mathbf{x},t) = \begin{cases} L_1 \dfrac{dx_1}{dt} = d_1 E_1 - d_1^{'} x_3 \\ L_2 \dfrac{dx_2}{dt} = d_2 E_2 - d_2^{'} x_3 \\ (C_1 + C_2) \dfrac{dx_3}{dt} = d_1^{'} x_1 + d_2^{'} x_2 - \dfrac{P}{x_3} \end{cases}$$
$$d_1^{'} = 1 - d_1, d_2^{'} = 1 - d_2$$
$$\mathbf{x} = \left[x_1, x_2, x_3 \right]^T = \left[i_{L1}, i_{L2}, v_C \right]^T \tag{81}$$

where d_1, d_2 refer to the instantaneous duty cycles of the top and bottom converters, respectively. Let

$$d_1 = g_1(x_1, x_3)$$
$$d_2 = g_2(x_2, x_3) \tag{82}$$

so that the control laws are symmetric. Substituting (82) in (81) and calculating (77) as generalized expression

$$\mathbf{A}=\begin{bmatrix} \frac{(E_1+x_3)}{L_1}\frac{\partial g_1}{\partial x_1} & 0 & \frac{(E_1+x_3)}{L_1}\frac{\partial g_1}{\partial x_3}+\frac{(g_1-1)}{L_1} \\ 0 & \frac{(E_2+x_3)}{L_2}\frac{\partial g_2}{\partial x_2} & \frac{(E_2+x_3)}{L_2}\frac{\partial g_2}{\partial x_3}+\frac{(g_2-1)}{L_2} \\ \left[\frac{1-g_1}{C_1+C_2}-\frac{x_1}{C_1+C_2}\frac{\partial g_1}{\partial x_1}\right] & \left[\frac{1-g_2}{C_1+C_2}-\frac{x_2}{C_1+C_2}\frac{\partial g_2}{\partial x_2}\right] & \left[\frac{P}{(C_1+C_2)x_3^2}-\frac{x_1}{C_1+C_2}\frac{\partial g_1}{\partial x_3}-\frac{x_2}{C_1+C_2}\frac{\partial g_2}{\partial x_3}\right] \end{bmatrix} \quad (83)$$

It can be observed from (83) that in order for all the 3 eigenvalues to lie on the left half of the *s* plane, one of the necessary conditions is that trace of **A** must be negative. Hence,

$$\frac{(E_1+x_3)}{L_1}\frac{\partial g_1}{\partial x_1}+\frac{(E_2+x_3)}{L_2}\frac{\partial g_2}{\partial x_2}+\frac{P}{(C_1+C_2)x_3^2}-\frac{x_1}{C_1+C_2}\frac{\partial g_1}{\partial x_3}-\frac{x_2}{C_1+C_2}\frac{\partial g_2}{\partial x_3}<0 \quad (84)$$

The primary controller is fully autonomous and hence g_1 and g_2 can be assumed to involve only x_1 and x_2 respectively. This means that primary controller of a converter can involve only the feedback of its own inductor current. Hence, considering the symmetric nature of g_1 and g_2 in (82)

$$\frac{\partial g_1}{\partial x_1}<0, \frac{\partial g_2}{\partial x_2}<0, \frac{\partial g_1}{\partial x_3}=\frac{\partial g_2}{\partial x_3}=0 \quad (85)$$

The simplest means to ensure that (85) is satisfied is by providing a proportional negative feedback of the inductor currents of the respective converters. But since $0<d_1<1$ and $0<d_2<1$ the following control laws can be used for primary control.

$$d_{1p}=\frac{k_1E_1-R_{d1}x_1}{E_1}, 0<d_{1p}<1, 0<k_1<1$$
$$d_{2p}=\frac{k_2E_2-R_{d2}x_2}{E_2}, 0<d_{2p}<1, 0<k_2<1$$
$$\frac{k_1E_1}{1-k_1}=\frac{k_2E_2}{1-k_2}=V_{nl} \quad (86)$$

In (86), V_{nl} refers to the no load voltage of the dc microgrid and R_{d1}, R_{d2} are virtual droop resistances. The resistances are virtual in the sense that they are proportional constants of the respective inductor currents and are realized through controller action. The control inputs given by (86) are conveniently referred to as the primary control inputs d_{1p}, d_{2p} respectively. The equilibrium point given by $[X_{1eq}, X_{2eq}, X_{3eq}]^T$ is obtained

in terms of R_{d1}, R_{d2}, E_1, E_2, k_1, k_2 and P. Among the above mentioned terms, all the quantities except P are constants. In the case of parallel buckboost converters, the equation to obtain X_{3eq} is given by

$$f_{pri}\left(X_{3eq}\right): a_4 X_{3eq}^4 + a_3 X_{3eq}^3 + a_2 X_{3eq}^2 + a_1 X_{3eq} + a_0 = 0 \tag{87}$$

where

$$\begin{aligned}
a_4 &= -E_1^2(1-k_1)R_{d2} - E_2^2(1-k_2)R_{d1} - PR_{d1}R_{d2} \\
a_3 &= E_1^3 k_1 R_{d2} + E_2^3 k_2 R_{d1} - 2R_{d1}E_2^2E_1(1-k_2) - 2R_{d2}E_1^2E_2(1-k_1) - 2PR_{d1}R_{d2}(E_1+E_2) \\
a_2 &= 2E_1^3E_2k_1R_{d2} + 2E_2^3E_1k_2R_{d1} - E_1^2(1-k_1)E_2^2R_{d2} - E_2^2(1-k_2)E_1^2R_{d1} - 4PR_{d1}R_{d2}E_1E_2 - PR_{d1}R_{d2}(E_1^2+E_2^2) \\
a_1 &= E_1^3E_2^2k_1R_{d2} + E_2^3E_1^2k_2R_{d1} - 2PR_{d1}R_{d2}E_1E_2(E_1+E_2) \\
a_0 &= -E_1^2E_2^2PR_{d1}R_{d2}
\end{aligned} \tag{88}$$

For practical values of E_1, E_2, R_{d1}, R_{d2}, the locus of real roots of quartic equation (87) for increasing values of P is indicated in Fig. 34. Of the four roots of the equation (87), two of them are always complex. The nature of the other two roots is as follows. When $P=0$, one of the two roots is $X_{3eq}=V_{nl}$ and the other is $X_{3eq}=0$. As P is increased, both the real roots start moving towards each other. At $P=P_{max}$, both the roots are equal to $X_{3eq,min}$. Beyond P_{max}, there are no real roots for the equation (87). Thus, the locus of real root which starts at $X_{3eq}=V_{nl}$ for $P=0$ and moves left till it reaches $P=P_{max}$ represents the locus of microgrid voltage. The primary control inputs (86) enable current sharing which is given by

$$I_{share} = \frac{X_{1eq}}{X_{2eq}} \tag{89}$$

The primary equilibrium point, $\mathbf{X_{eq,pri}}$ obtained in terms of X_{3eq} is given by

$$\mathbf{X_{eq,pri}} = \begin{bmatrix} X_{1eq} \\ X_{2eq} \\ X_{3eq} \end{bmatrix} = \begin{bmatrix} \dfrac{E_1(1-k_1)(V_{nl}-X_{3eq})}{R_{d1}(X_{3eq}+E_1)} \\ \dfrac{E_2(1-k_2)(V_{nl}-X_{3eq})}{R_{d2}(X_{3eq}+E_2)} \\ X_{3eq} \end{bmatrix} \tag{90}$$

In the case of parallel buckboost converters, in order to obtain $X_{3eq,min}$ and P_{max} in Fig. 34, the following procedure can be followed. From (87), (88) we can write

$$h_{pri}\left(X_{3eq}\right): PR_{d1}R_{d2} = \frac{b_4X_{3eq}^4 + b_3X_{3eq}^3 + b_2X_{3eq}^2 + b_1X_{3eq}}{c_4X_{3eq}^4 + c_3X_{3eq}^3 + c_2X_{3eq}^2 + c_1X_{3eq} + c_0} \tag{91}$$

where b_4,b_3,b_2,b_1 correspond to a_4,a_3,a_2 and a_1 respectively in (88) without terms containing P and c_4,c_3,c_2,c_1 and c_0 correspond to negative of coefficients of $PR_{d1}R_{d2}$ in (88). From (91), at $P=P_{max}$

Quantity	Buck	Boost	Buckboost
X_{3eq} at $P=0$	$V_{nl}=k_1E_1, 0<k_1\leq 1$	$V_{nl}=\frac{E_1}{(1-k_1)}, 0\leq k_1<1$	$V_{nl}=\frac{E_1k_1}{(1-k_1)}, 0<k_1<1$
X_{3eq} at $P=P_{max}$	$\frac{V_{nl}}{2}$	E_1 if $E_1>E_2$ and E_2 if $E_1<E_2$	$0<X_{3eq,min}<\frac{V_{nl}}{2}$ refer(91),(92)
P_{max}	$\frac{V_{nl}^2}{4R_{d12}}, R_{d12}=R_{d1}\|\|R_{d2}$	$\frac{k_1\left(E_1^3R_{d2}+E_2^3R_{d1}\right)}{E_1R_{d1}R_{d2}}$ if $E_1>E_2$ $\frac{k_2\left(E_1^3R_{d2}+E_2^3R_{d1}\right)}{E_2R_{d1}R_{d2}}$ if $E_1<E_2$	$P=P_{max}$ refer (93)
current sharing (89)	$\frac{R_{d2}}{R_{d1}}$	$\frac{E_1^2R_{d2}}{E_2^2R_{d1}}$	$\frac{(1-k_1)^2R_{d2}\left(E_2+X_{3eq}\right)k_2}{(1-k_2)^2R_{d1}\left(E_1+X_{3eq}\right)k_1}$

Table 1: Primary control results for 3 basic topologies

$$\frac{\partial h_{pri}}{\partial X_{3eq}} = 0 \tag{92}$$

However, (92) is a sixth degree equation and hence the roots ($X_{3eq,min}$) can be obtained only for specific values of system parameters [72]. Once $X_{3eq,min}$ is obtained, P_{max} can be calculated using

$$P_{\max} = \begin{cases} \dfrac{X_{3eq,\min}^2}{R_{d1}} \left(\dfrac{E_1}{E_1 + X_{3eq,\min}} \right)^3 \left((1+k_1) - \dfrac{X_{3eq,\min}}{E_1}(1-k_1) \right) + \\ \dfrac{X_{3eq,\min}^2}{R_{d2}} \left(\dfrac{E_2}{E_2 + X_{3eq,\min}} \right)^3 \left((1+k_2) - \dfrac{X_{3eq,\min}}{E_2}(1-k_2) \right) \end{cases} \tag{93}$$

Table. 1 gives results regarding primary control and equilibrium points for three basic configurations. Some observations about Table. 1 are as follows

1. As P is increased from 0, the voltage at dc microgrid, X_{3eq} starts reducing from V_{nl}. At $P=P_{max}$, $X_{3eq}=X_{3eq,min}$.
2. The characteristic obtained in Fig. 34 for parallel buckboost converters is similar to that obtained for parallel buck converters [20], however, there are some differences. In the case of parallel buck converters, $X_{3eq,min}$ is a constant and is given by

$$X_{3eq,\min} = \frac{V_{nl}}{2} \tag{94}$$

In case of parallel buckboost converters,

$$0 < X_{3eq,\min} < \frac{V_{nl}}{2} \tag{95}$$

However, for stability considerations, parallel buckboost operation can be restricted to lie in the region

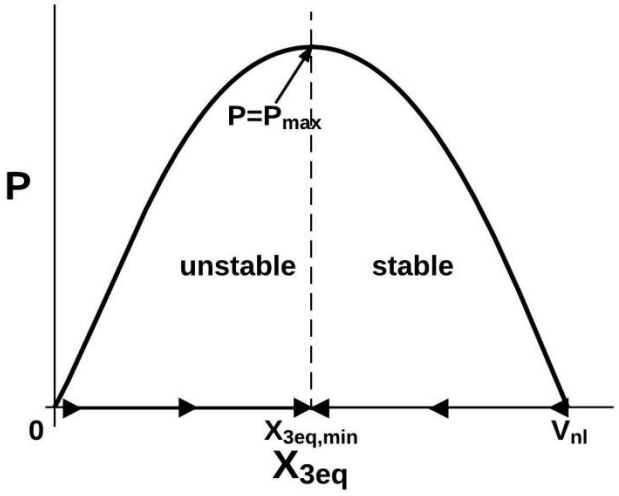

Fig. 34. X_{3eq} Vs P characteristics for parallel buckboost converters in Fig. 32

$$\frac{V_{nl}}{2} \le X_{3eq} \le V_{nl} \tag{96}$$

4. In case of parallel buck and parallel buckboost configurations, stable operation range is given by (96). The expression for P_{max} for parallel boost converters is obtained as a result of duty cycle restrictions rather than as an explicit expression as in the case of other two simple topologies.

5. A fixed current sharing ratio(independent of P) (89) is obtained in the case of parallel buck and parallel boost converters since the inductor is located at the output and input of the respective converters. However, this observation is true only in the case of simple converter topologies.

Droop controllers enable current sharing at the cost of poor voltage regulation at the dc microgrid. This poor voltage regulation is a result of voltage drop in the droop resistances which can be remedied by adding secondary control inputs [38]. In general, for an m parallel converter case, overall (primary + secondary) control input of q^{th} parallel converter, $d_{q,s}$ is given by

$$d_{q,s} = \frac{k_q E_q - x_{Lq} R_{dq} + k_{iq} \int (V_{nl} - x_{\mu g}) dt}{E_q} \tag{97}$$

where k_{iq} is the integral control gain q^{th} converter. The variable $x_{\mu g}$ is the state variable corresponding to the microgrid voltage. The equilibrium point obtained with the overall control inputs, $\mathbf{X_{eq,sec}}$ can be calculated as explained previously. For ideal microgrid operation, it is desired that current sharing (89) obtained in primary control stage is maintained after the addition of secondary controller. The integral control gains of secondary controllers are designed so as to attain this objective. If current sharing ratio in primary control stage is constant (independent of P), it can be ensured that after addition of secondary controllers, current sharing ratio is identical to that in primary control stage. If current sharing ratio in primary control stage is not constant, then some approximation needs to be made in the expression for current sharing ratio in the primary control stage (89) so that after the addition of secondary controllers, it is almost identical to that in the primary control stage.

Taking the example of parallel buckboost converters, the overall control inputs are given by

$$d_1 = \frac{k_1 E_1 - x_1 R_{d1} + k_{i1}\int (V_{nl} - x_3)dt}{E_1}$$
$$d_2 = \frac{k_2 E_2 - x_2 R_{d2} + k_{i2}\int (V_{nl} - x_3)dt}{E_2} \tag{98}$$

where k_{i1} and k_{i2} are the integral control constants of the top and bottom converters respectively. In the case of parallel buckboost converters, the equilibrium point obtained using the control input (98) is given by

$$\mathbf{X_{eq,sec}} = \begin{bmatrix} X_{1eq} \\ X_{2eq} \\ X_{3eq} \end{bmatrix} = \begin{bmatrix} \dfrac{k_{i1} P R_{d2}}{V_{nl}\left(k_{i1} R_{d2}(1-k_1) + k_{i2} R_{d1}(1-k_2)\right)} \\ \dfrac{k_{i2} P R_{d1}}{V_{nl}\left(k_{i1} R_{d2}(1-k_1) + k_{i2} R_{d1}(1-k_2)\right)} \\ V_{nl} \end{bmatrix} \tag{99}$$

In the case of buckboost converters, the inductor current given by X_{1eq} in (90) and (99) is neither equal to input current nor equal to the output current of the top converter in Fig. 32. In order to calculate the input currents of the top and bottom converters, consider Fig. 33 which contains the equivalent circuit of the top buckboost converter in Fig. 32. From (90), the vector of input currents of the top and bottom converters in primary control stage represented as $\mathbf{I_{in,pri}}$ is given by

$$\mathbf{I_{in,pri}} = \begin{bmatrix} I_{in1,pri} \\ I_{in2,pri} \end{bmatrix} = \begin{bmatrix} \dfrac{E_1(1-k_1)(V_{nl}-X_{3eq})X_{3eq}}{R_{d1}(E_1+X_{3eq})^2} \\ \dfrac{E_2(1-k_2)(V_{nl}-X_{3eq})X_{3eq}}{R_{d2}(E_2+X_{3eq})^2} \end{bmatrix} \tag{100}$$

Consider the ratio of the input currents of the converters similar to (89)

$$\frac{I_{in1,pri}}{I_{in2,pri}} = \frac{E_1(1-k_1)R_{d2}(E_2+V_{nl}-V_{dr})^2}{E_2(1-k_2)R_{d1}(E_1+V_{nl}-V_{dr})^2} \tag{101}$$

where V_{dr} is the droop voltage and $X_{3eq}=V_{nl}-V_{dr}$. Substituting for V_{nl} from (86) and simplifying

$$\frac{I_{in1,pri}}{I_{in2,pri}} = \frac{E_1(1-k_1)R_{d2}\left(\dfrac{E_2}{(1-k_2)}-V_{dr}\right)^2}{E_2(1-k_2)R_{d1}\left(\dfrac{E_1}{(1-k_1)}-V_{dr}\right)^2} \tag{102}$$

Since $k_2<1$ and $k_1<1$ and considering

$$\frac{E_2}{(1-k_2)} > V_{nl} > V_{dr}$$
$$\frac{E_1}{(1-k_1)} > V_{nl} > V_{dr} \tag{103}$$

Considering (103), (96), V_{dr} can be neglected in (102) and the following approximation can be made.

$$\frac{I_{in1,pri}}{I_{in2,pri}} = \frac{E_2(1-k_1)^3 R_{d2}}{E_1(1-k_2)^3 R_{d1}} \tag{104}$$

Some reasons for considering the approximation (104) are as follows. A standard voltage of 400Vdc is used in data centers and 48Vdc is used in telecom sector [73]. Thus V_{nl} in (101) is fixed. However, controllers can be designed so as to keep V_{dr} at a minimum value and also maintain stability. As already explained (96), the maximum value of V_{dr} is restricted to ($V_{nl}/2$). Hence the approximation in (102) is valid. Considering the sharing of input currents (104), current sharing is maintained after the addition of secondary controller even at heavy loads. Following the same steps and calculating the converter input currents in the secondary stage $I_{in1,sec}$ and $I_{in2,sec}$ from (99)

$$\mathbf{I_{in,sec}} = \begin{bmatrix} I_{in1,sec} \\ I_{in2,sec} \end{bmatrix} = \begin{bmatrix} \dfrac{k_{i1} P R_{d2} k_1}{V_{nl}\left(k_{i1} R_{d2}(1-k_1) + k_{i2} R_{d1}(1-k_2)\right)} \\ \dfrac{k_{i2} P R_{d1} k_2}{V_{nl}\left(k_{i1} R_{d2}(1-k_1) + k_{i2} R_{d1}(1-k_2)\right)} \end{bmatrix} \tag{105}$$

Equating (100) and (105) and considering (104) to make current sharing (at the converter input) in primary and secondary stage to be equal

$$\begin{aligned} k_{i1} &= k_i k_2 E_2 (1-k_1)^3 \\ k_{i2} &= k_i k_1 E_1 (1-k_2)^3 \end{aligned} \tag{106}$$

In the case of paralleled buckboost converters $\mathbf{X_{eq,pri}}$ and $\mathbf{X_{eq,sec}}$ are given by (90) and (99) respectively. Table. 2 gives results regarding secondary control for the 3 basic converter configurations.

Quantity	Buck	Boost	Buck boost
Integral control gain	$k_{i1}=k_{i2}=k_i$	$k_{i1} = k_i E_1^2$ $k_{i2} = k_i E_2^2$	$k_{i1} = k_i k_2 E_2 \left(1-k_1\right)^3$ $k_{i2} = k_i k_1 E_1 \left(1-k_2\right)^3$
Current sharing ratio	$\dfrac{R_{d2}}{R_{d1}}$	$\dfrac{E_1^2 R_{d2}}{E_2^2 R_{d1}}$	$\dfrac{k_2 E_2 \left(1-k_1\right)^3 R_{d2}}{k_1 E_1 \left(1-k_2\right)^3 R_{d1}}$

Table 2: Secondary control results for 3 basic topologies

STABILITY CONDITIONS

The control inputs of the form (79) and (97) are applied to paralleled converters supplying CPL. The resulting equilibrium points, $\mathbf{X_{eq,pri}}$ and $\mathbf{X_{eq,sec}}$ are only locally asymptotically stable. To arrive at necessary and sufficient conditions for the local asymptotic stability of $\mathbf{X_{eq,pri}}$ and $\mathbf{X_{eq,sec}}$, the respective control inputs are applied in the system equations (75). The jacobian of system equations, **A** (77) is evaluated at $\mathbf{X_{eq,pri}}$ and $\mathbf{X_{eq,sec}}$ separately. The system characteristic equation given by $det(s\mathbf{I}-\mathbf{A})$ is obtained at each of these equilibrium points. The necessary and sufficient conditions to ensure local asymptotic stability of each of the equilibrium points can be derived using Routh stability criterion [67]. Let us assume that the primary control inputs (79) are applied to the system equations (75). Let us assume that the system characteristic equation is given by

$$\det\left(s\mathbf{I}-\mathbf{A}\right)=s^{n}+a_{n-1}s^{n-1}+.....+a_{1}s+a_{0} \tag{107}$$

where a_{n-1}, $....a_1$, a_0 are real and they are coefficients of the system characteristic equation. Among the necessary conditions to ensure local asymptotic stability, the conditions which hold true for any value of m (number of converters connected in parallel) are

$$a_{n-1}>0 \Leftrightarrow \operatorname{trace}(A)<0 \tag{108}$$

$$a_{0}>0 \Leftrightarrow \begin{cases}\det(A)<0 \text{ if } n \text{ is odd}\\ \det(A)>0 \text{ if } n \text{ is even}\end{cases} \tag{109}$$

The condition (108) involves relation between the converter elements like L, C apart from source voltages **E,** load power P and the vector of droop resistances $\mathbf{R_d}$ whereas (109) does not involve the converter elements L and C. In other words, (108) is related to dynamic stability of converters whereas (109) is related to steady-state stability. Apart from conditions listed above, the conditions

$$\begin{aligned} &a_{n-2} > 0 \\ &\vdots \\ &a_1 > 0 \end{aligned} \tag{110}$$

depend on number of .paralleled converters *m*. The conditions (110) also depend on the converter elements *L, C* apart from source voltages, droop resistances and load power. Apart from (108), (109) and (110), which are only necessary conditions for local asymptotic stability, there are necessary and sufficient conditions which can be examined from Routh array [67].

As explained earlier, since (108), (109) are independent of *m*, they are examined in detail using the equivalent circuits of the converters. First, consider condition (108). To explain the physical significance of (108), the virtual droop resistances are replaced by actual physical resistances. The circuit consisting of *m* parallel converters is broken down as follows.

1. *m* series R-L circuits consisting of the respective source voltage, inductance and droop resistance as shown in Fig. 35(a) .
2. One series R-C circuit consisting of CPL as represented by its equivalent circuit [20] and the output capacitor as shown in Fig. 35(b).

Defining the quantities

$$\frac{di_{L1}}{dt}(pu)_{(t=0)} = \frac{\frac{di_{L1}}{dt}_{(t=0)}}{i_{L1(t=\infty)}} = \frac{R_{d1}}{L_1} \tag{111}$$

$$\frac{di_C}{dt}(pu)_{(t=0)} = \frac{\frac{di_C}{dt}_{(t=0)}}{i_{C(t=0)}} = \frac{P}{Cv_C^2} \tag{112}$$

where $\frac{di_{L1}}{dt}(pu)$ and $\frac{di_C}{dt}(pu)$ are user-defined quantities which represent per-unit values of the rate of change of the inductor and capacitor currents. They are not strictly per-unit

values in the sense that they are ratios of change in current to the actual current through the inductor and capacitor respectively.

The condition $a_{n-1}>0$ states that

$$\sum_{i=1}^{m} \frac{di_{L,i}}{dt}(pu)_{(t=0)} > \frac{di_C}{dt}(pu)_{(t=0)} \tag{113}$$

However, for (113) to hold true, the quantities on both the sides of (113) should be referred to the same side of transformer in the equivalent circuit. It should be noted that in each of the basic converter topologies, inductors are located closer to the source than capacitor. The condition (113) simply means that the inductors and droop resistances of the converters must be designed such that the sum of initial rates of rise of currents in the input R-L circuits should be greater than the initial rate of rise of current through

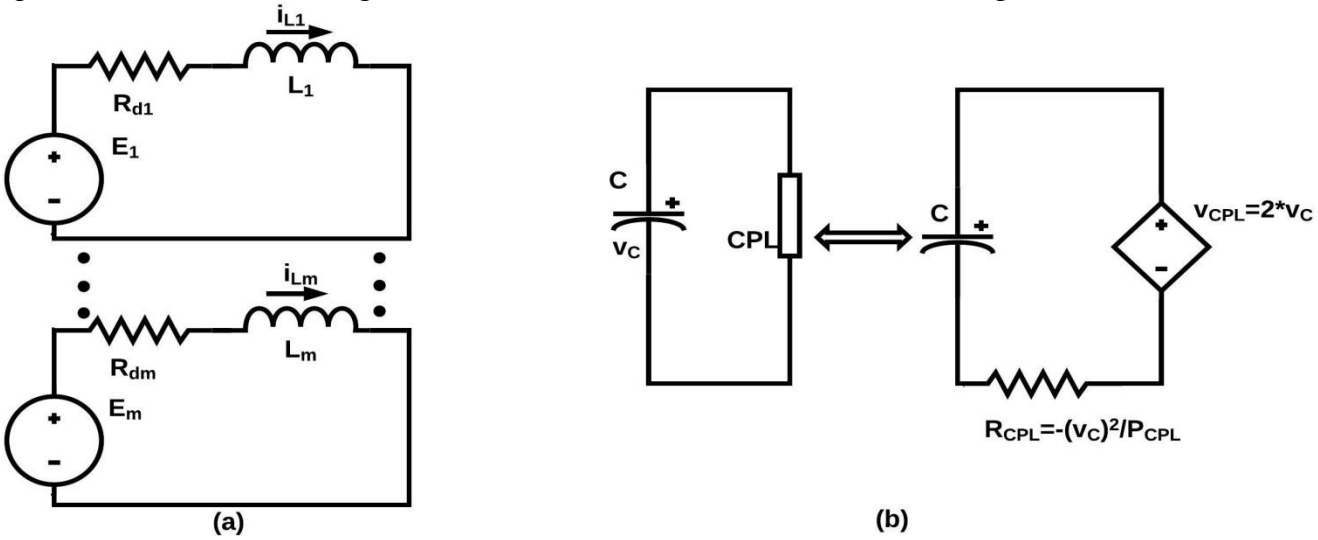

Fig.35.System of paralleled source converters in Fig. 31 broken down into (a) *m* input modules consisting of source voltage, droop resistance and inductance (b) one output module consisting of capacitor and equivalent circuit of CPL from [20]

the output R-C circuit. The increase in current through the output R-C circuit in (113) can be explained by the fact that R_{CPL} in Fig. 35(b) is negative. Now, consider condition (109)

which involves only the droop resistances and load power P. It is the well-known Middlebrook criterion [72]. In literature, while performing stability analysis, this criterion is checked numerically for specific cases. In this paper, general expressions have been derived for Middlebrook criterion which can be applied to any microgrid containing non-isolated converter topologies. The equivalent circuit of converter is used for this purpose. The Middlebrook criterion suggests that when viewed from the microgrid load coupling point, equivalent load resistance should be greater than the equivalent source resistance [72]. While calculating source and load resistances using the equivalent circuit approach, they have to be referred to the same side of transformer in the equivalent circuit.

The stability criteria listed in (108) and (109) are examined in context of parallel buckboost converters. Consider the system (81) with only primary control inputs (86) applied. The characteristic polynomial for the **A** matrix is

$$\det(s\mathbf{I}-\mathbf{A}) = s^3 + a_2 s^2 + a_1 s + a_0 \tag{114}$$

To derive the condition corresponding to $a_2>0$, we proceed as follows. Breaking down the parallel buckboost converter circuit into 2 R-L series circuits and 1 R-C series circuit as explained previously, we can calculate

$$L_1 \frac{dx_1}{dt} = L_1 \frac{R_{d1}}{L_1} \frac{E_1}{R_{d1}} e^{-\frac{R_{d1}}{L_1}t} \tag{115}$$

Referring voltage across inductor (115) to the output of the buckboost converter in Fig. 33 and applying condition (113), we obtain

$$\frac{R_{d1}}{L_1}\left(1+\frac{X_{3eq}}{E_1}\right)+\frac{R_{d2}}{L_2}\left(1+\frac{X_{3eq}}{E_2}\right) > \frac{P}{(C_1+C_2)X_{3eq}^2} \tag{116}$$

which is identical to the condition $a_2>0$ obtained using (108) in the characteristic equation. To obtain the condition corresponding to $a_0>0$ for the parallel buckboost configuration, consider the equivalent circuit of buckboost converter in Fig. 33. Referring

the droop resistance R_d to the output of the transformer in the right and simplifying, we obtain

$$\frac{1}{R_{d1}}\left[\frac{E_1}{E_1+X_{3eq}}\right]^2+\frac{1}{R_{d2}}\left[\frac{E_2}{E_2+X_{3eq}}\right]^2>\frac{P}{X_{3eq}^2} \tag{117}$$

For $P<P_{max}$, this condition holds true for $(V_{nl}/2) \leq X_{3eq} \leq V_{nl}$. In addition, this condition is also shown to hold true numerically for practical values of converter voltages and droop resistances in the voltage range $X_{3eq,min} \leq X_{3eq} \leq (V_{nl}/2)$. Apart from the conditions (116), (117) the other necessary condition for the asymptotic stability of $\mathbf{X_{eq,pri}}$ (90) is

$$a_1>0 \Rightarrow \frac{1}{L_1(C_1+C_2)}\left[\frac{\left(E_1(1+k_1)-X_{3eq}(1-k_1)\right)E_1}{\left(E_1+X_{3eq}\right)^2}\right]+\frac{1}{L_2(C_1+C_2)}\left[\frac{\left(E_2(1+k_2)-X_{3eq}(1-k_2)\right)E_2}{\left(E_2+X_{3eq}\right)^2}\right]$$
$$+\frac{X_{3eq}R_{d1}R_{d2}}{L_1L_2}\left(\frac{1}{E_1}+\frac{1}{E_2}\right)+\frac{R_{d1}R_{d2}}{L_1L_2}\left[\frac{X_{3eq}^2}{E_1E_2}+1\right]>\frac{P}{(C_1+C_2)X_{3eq}}\left[\frac{R_{d1}}{L_1E_1}+\frac{R_{d2}}{L_2E_2}+\frac{R_{d2}}{L_2X_{3eq}}+\frac{R_{d1}}{L_1X_{3eq}}\right] \tag{118}$$

Next, we need to check for the stability of the $\mathbf{X_{eq,sec}}$, obtained after the insertion of primary and secondary controller. Then, the system characteristic equation for the m parallel converter configuration is given by

$$\det(s\mathbf{I}-\mathbf{A})=s^{n+1}+b_ns^n+b_{n-1}s^{n-1}+.....+b_1s+b_0 \tag{119}$$

where $b_n, b_{n-1}, ..., b_0$ are real. The condition $b_n>0$ is satisfied once the condition (108) .i.e. $a_{n-1}>0$ is satisfied. The condition $b_0>0$ is satisfied for all practical values of droop resistances and integral control gains. The most significant stability conditions for $\mathbf{X_{eq,sec}}$ correspond to those pertaining to the integral control gain k_i. However, these conditions are dependent on converter configuration, microgrid size and can be numerically verified for separate cases.

Taking the example of paralleled buckboost converters, the characteristic polynomial with overall (primary + secondary) control inputs (98) inserted is given by

$$\det\left(s\mathbf{I}-\mathbf{A}\right)=s^4+b_3s^3+b_2s^2+b_1s+b_0 \tag{120}$$

Applying the Routh stability criterion, the conditions for local asymptotic stability of the equilibrium point (99) can be obtained. The necessary stability condition corresponding to $b_3>0$ is given by

$$b_3>0\Rightarrow\frac{R_{d2}}{L_2}\left(\frac{V_{nl}}{E_2}+1\right)+\frac{R_{d1}}{L_1}\left(\frac{V_{nl}}{E_1}+1\right)>\frac{P}{(C_1+C_2)V_{nl}^2} \tag{121}$$

As can be seen, (121) is obtained by replacing X_{3eq} in (116) with V_{nl}. Since $V_{nl}\geq X_{3eq}$ (121) is always satisfied when (116) is satisfied. One of necessary conditions on k_i with regard to parallel buckboost converters is

$$b_2>0\Rightarrow\frac{X_{1eq}}{E_1(C_1+C_2)}\left[k_{i1}-\frac{R_{d1}(1-k_1)}{L_1}\right]+\frac{X_{2eq}}{E_2(C_1+C_2)}\left[k_{i2}-\frac{R_{d2}(1-k_2)}{L_2}\right]<\frac{1}{(C_1+C_2)}\left[\frac{(1-k_1)^2}{L_1}+\frac{(1-k_2)^2}{L_2}\right]$$
$$+\frac{V_{nl}R_{d1}R_{d2}}{L_1L_2}\left[\frac{1}{E_1}+\frac{1}{E_2}\right]+\frac{(1-k_1-k_2+2k_1k_2)R_{d1}R_{d2}}{L_1L_2(1-k_1)(1-k_2)}-\frac{P}{V_{nl}(C_1+C_2)}\left[\frac{R_{d1}}{L_1V_{nl}}+\frac{R_{d2}}{L_2V_{nl}}+\frac{R_{d1}}{L_1E_1}+\frac{R_{d2}}{L_2E_2}\right] \tag{122}$$

Term	Buck	Boost	Buckboost
$a_2>0$	$\frac{R_{d1}}{L_1}+\frac{R_{d2}}{L_2}>\frac{P}{(C_1+C_2)X_{3eq}^2}$	$X_{3eq}\left[\frac{R_{d2}}{L_2E_2}+\frac{R_{d1}}{L_1E_1}\right]>\frac{P}{(C_1+C_2)X_{3eq}^2}$	$\left.\begin{array}{l}\frac{R_{d1}}{L_1}\left(1+\frac{X_{3eq}}{E_1}\right)+\\ \frac{R_{d2}}{L_2}\left(1+\frac{X_{3eq}}{E_2}\right)\end{array}\right\}>\frac{P}{(C_1+C_2)X_{3eq}^2}$
$a_0>0$	$\frac{1}{R_{d1}}+\frac{1}{R_{d2}}>\frac{P}{X_{3eq}^2}$	$\frac{1}{R_{d1}}\left(\frac{E_1}{X_{3eq}}\right)^2+\frac{1}{R_{d2}}\left(\frac{E_2}{X_{3eq}}\right)^2>\frac{P}{X_{3eq}^2}$	$\left.\begin{array}{l}\frac{1}{R_{d1}}\left[\frac{E_1}{E_1+X_{3eq}}\right]^2\\ +\frac{1}{R_{d2}}\left[\frac{E_2}{E_2+X_{3eq}}\right]^2\end{array}\right\}>\frac{P}{X_{3eq}^2}$

Table 3: Stability results for 3 basic topologies

Table.3 gives common stability results for three basic configurations. It should be reiterated that in order to arrive at the stability conditions listed in Table. 3, there is no computational effort involved in terms of calculation of system characteristic equations (107), (119). Specifically, actual evaluation of the condition $a_0>0$ (109) using system characteristic equation provides a result which is different from that evaluated using equivalent circuit approach. For example, in the case of parallel buckboost converters, actual evaluation of condition (109) using system characteristic equation gives (93) (with an inequality relation), whereas the one evaluated using equivalent circuit approach is (117). This is due to the presence of transformers with nonlinear turns-ratio in the equivalent circuit in Fig. 33. Even though (117) is more conservative than (93), with regard to computational effort involved and its general ease of extension to any value of m, (117) seems to be a better solution. Even for a large system containing basic topologies, stability conditions (107), (108) can be derived using the equivalent circuit approach. It saves a lot of effort in terms of linearizing the system equations and calculation of jacobian (77).

SIMULATION AND EXPERIMENTAL RESULTS

Simulation results

Simulation and experiments are performed to show the validity of analysis. The circuit shown in Fig. 32 is used in simulation and experiments. The circuit parameters are the following. E_1=36V, E_2=28V, C_1=C_2=660μF, L_1= L_2=400μH, V_{nl}=32V, P=130W, R_{d1}=0.4Ω, R_{d2}=0.3Ω. Initially, the circuit is operated in open loop with D_{OL1}=0.471 and D_{OL2}=0.533 which are the open loop duty ratios of the two converters respectively. The simulation results for open loop operation are shown in Fig. 36. Limit cycle oscillations of a frequency of around 150Hz are observed in the voltage and current waveforms in Fig. 36. The primary controllers (86) are switched on at t=0.2s. The simulation results for

transition from open loop to primary control are given in Fig. 37. It can be observed from Fig. 37 that x_1, x_2 and x_3 settle down at equilibrium values of 4.43A, 4.64A and 26.2V respectively. The input currents of the two converters are I_{in1}=1.87A and I_{in2}=2.25A (100). The input currents are shared in the ratio I_{in2}:I_{in1}=1.20. Since the voltage drop after primary controller is added may be unacceptable, secondary controller with k_i=0.45 (98) is added to primary controller at t=0.5s. Fig. 38 shows the simulation results for the transition from primary control mode to secondary control mode. It can be observed from Fig. 38 that the microgrid voltage, x_3 raises to 32V. The inductor currents, x_1 and x_2 decrease and settle down at 4.02A and 4.16A respectively after some initial dynamics. The corresponding input current values are I_{in1}=1.89A and I_{in2}=2.22A (105) and the ratio of the input currents I_{in2}:I_{in1}=1.18. Thus, input current sharing ratios are identical in the primary and secondary control stages.

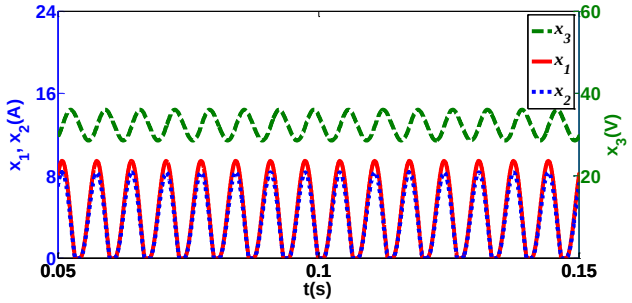

Fig. 36. Simulation results of a parallel buckboost converters- open loop operation.

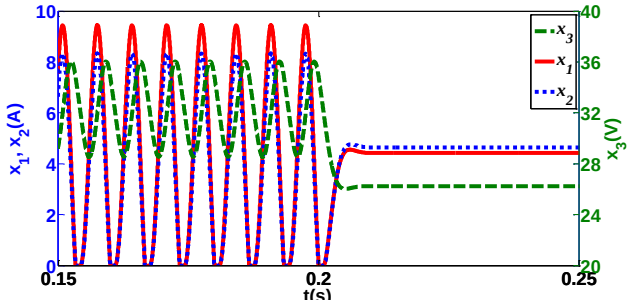

Fig. 37. Simulation results for parallel buckboost converters transitioning from open loop to primary control

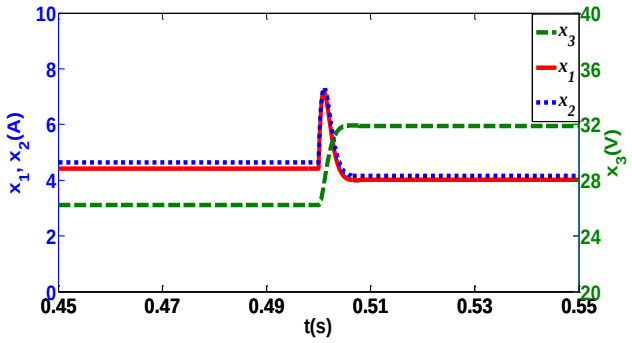

Fig. 38. Simulation results for parallel buckboost converters transitioning from primary control to secondary control

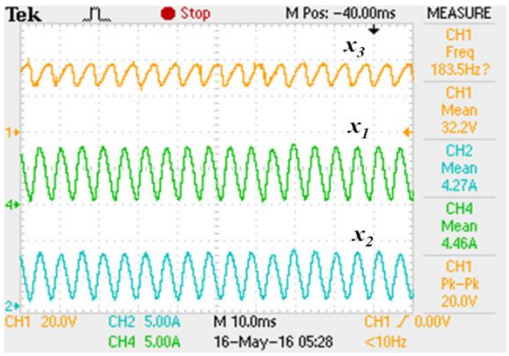

Fig. 39. Experimental results of parallel buckboost converters-open loop

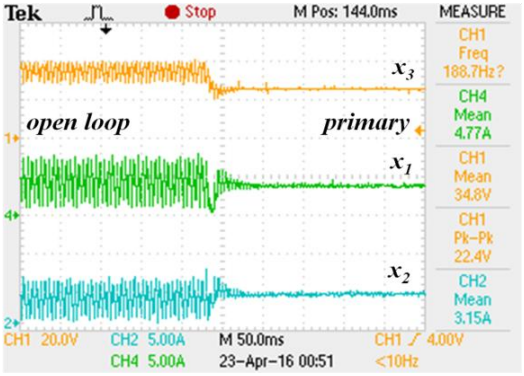

Fig. 40. Experimental results for parallel buckboost converters transitioning from open loop to primary control

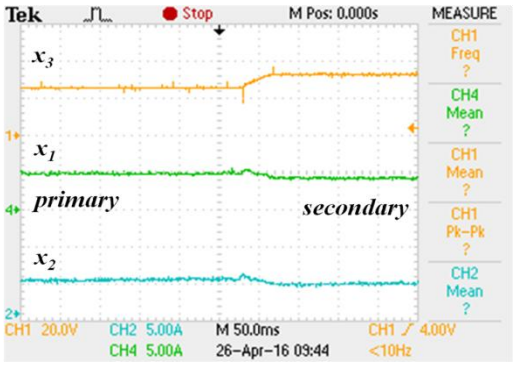

Fig. 41. Experimental results for parallel buckboost converters transitioning from primary control to secondary control

Experimental results

The circuit parameters used in the experimental dc microgrid are identical to the simulation parameters. Texas instruments based TM4C123 launchpads are used for digital control of the converters. The above mentioned launchpad is a low cost microcontroller implementing several useful features including a CAN communication interface [75]. A total of 3 launchpads are used. Two launchpads are used for the local control of paralleled converters. One launchpad is used to sense the microgrid voltage and communicate secondary control signals to the paralleled converters using a CAN communication network. The CPL is realized by loading the microgrid with a buck converter whose output voltage is maintained constant using a fast regulating PI controller. Such a converter is also called point of load (POL) converter [18]. The parameters of the POL buck converter are as follows. L_L=300µH, C_L=1680µF, V_L=16.2V, R_L=2Ω. Thus, CPL of 130W is realized. The open loop waveforms of the state variables are shown in Fig. 39. During open loop operation, x_1 and x_2 depend on internal impedance of the sources E_1 and E_2 which are dc power supplies in this case. The transition of microgrid from open loop to primary control is given in Fig. 40. As soon as the primary controller is switched on, limit cycle oscillations are damped in about 30ms.

The inductor currents x_1, x_2 settle down at their equilibrium values of 4.42A and 4.64A respectively. The microgrid voltage drops to X_{3eq}=26.2V. Thus primary controller enables current sharing whose ratio is given by X_{2eq}:X_{1eq}=1.05. As mentioned earlier, CAN communication protocol is used to implement secondary controller. CAN transceiver chips MCP2551 are used as interface between microcontrollers and the CAN bus. The MCP2551 is a 5V, noise tolerant, high speed chip capable of protecting the microcontrollers from the current spikes in the CAN bus. Data transfer rate is fixed at a maximum of 1 Mbps and secondary control signal is transmitted as a 12 bit data. Since, there are only two receivers, only 2 bits of the 11 bit identifier are used for identification purposes. A part of the 12 bit data is encoded within the other nine bits of the identifier. Thus faster communication is possible and secondary control data is transmitted at 20kHz. The results showing the transition from primary control mode to secondary control mode is given in Fig. 41. As soon as the secondary controller is switched on, the microgrid voltage raises to 32V. The two inductor currents x_1 and x_2 slightly decrease and settle down to their new equilibrium values of X_{1eq}=4.02A and X_{2eq}=4.16A in about 50ms. The current sharing ratio is given by X_{2eq}:X_{1eq}=1.04 which is almost identical to the primary control stage. Secondary controllers enable line and load regulation. To test line regulation, the input voltage of converter 2, E_2 is reduced to 23V and the results are given in Fig. 42. It can be observed from Fig. 42 that x_2 decreases to 1.88A, x_1 increases to 6.19A and x_3 is restored to 32V within 150ms. Thus CAN based secondary controller is effective in ensuring that microgrid voltage is restored to V_{nl} even if the source voltages vary. To test load regulation, the load power is increased from 130W to 180W. and results are given in Fig. 43. It can be observed from Fig. 43 that x_1 and x_2 increase to their new equilibrium values of X_{1eq}=5.55A, X_{2eq}=5.75A. The microgrid voltage X_{3eq} is restored to 32V within 70ms. Another important observation is as follows. The current

sharing of inductor currents, X_{2eq}:X_{1eq}=1.04 and the input currents, I_{in2}:I_{in1}=1.17 are identical to those obtained in the primary and secondary control stages.

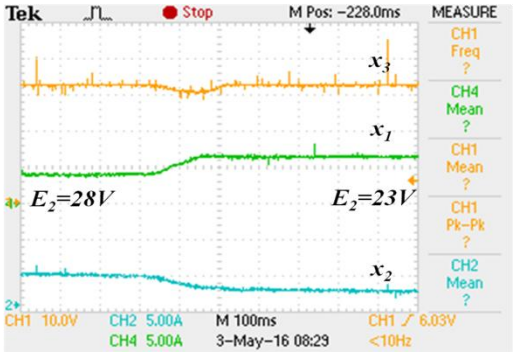

Fig. 42. Experimental results for line regulation of parallel buckboost converters

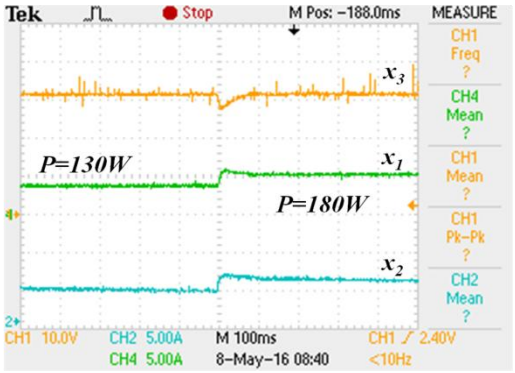

Fig. 43. Experimental results for load regulation of parallel buckboost converters

SUMMARY

A general framework for designing hierarchical control scheme for dc microgrids with CPLs is proposed in this paper. The control scheme consists of two levels and is developed as follows. Using small-signal linearized approach, the first or lower control level namely primary control is designed. This primary control scheme involves feedback of inductor currents of the individual paralleled converters and is autonomous. The significance of primary controller is that it enables current sharing among paralleled

converters and also damps limit cycle oscillations due to CPL. To compensate for the voltage deviations due to primary controller, the second level of control, namely secondary controller is added. This secondary control stage is an integral controller which communicates to local controllers using a high speed communication link. The secondary control gains are designed to ensure that current sharing obtained using primary controller is maintained. The stability conditions are explained using equivalent circuit of the converters. Using the equivalent circuit approach, stability conditions can be derived for a general dc microgrid with minimum effort. The control schemes and stability results are compared for microgrids containing the three basic converter topologies. The validity of proposed control schemes are shown through simulation and experimental results.

Chapter 5: A Linear Damping Scheme for Higher Order dc-dc Converters Supplying Constant-Power Loads in a dc Microgrid[3]

CONTROLLER DESIGN AND ANALYSIS

A system of non-isolated dc-dc converters of various topologies supplying a CPL is shown in Fig. 44

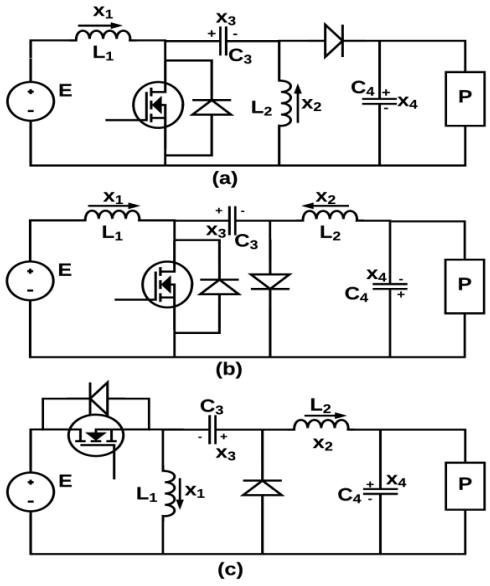

Fig. 44 Higher-order dc-dc converters supplying a CPL. (a). SEPIC, (b) Cuk, (c) Zeta

The state equations for the converters in Fig. 44 can be given in the form

$$\begin{aligned} L_n \dot{x}_n &= f_n(\mathbf{x}, d, t),\ n = 1, 2 \\ C_n \dot{x}_n &= f_n(\mathbf{x}, d, t),\ n = 3, 4 \end{aligned} \tag{123}$$

In (123), **x** is the vector of state variables which is given by

$$\mathbf{x} = [x_1, x_2, x_3, x_4]^T \tag{124}$$

The state variables x_1, x_2, x_3 and x_4 are the respective inductor currents and capacitor voltages as given in Fig. 44. The variable d refers to the duty cycle of the MOSFET. Similarly, the vector of state equations can be defined such that

[3] Contents of this chapter are published in "A Linear Damping Scheme for Higher Order DC-DC converters Supplying Constant Power Loads in a DC Microgrid", proc. Energy Conversion Congress and Exposition (ECCE-Europe) 2017., where Mahesh Srinivasan is the first author

$$\mathbf{f} = [\, f_1,\, f_2,\, f_3,\, f_4 \,]^T \tag{125}$$

The state equations for the 3 converters in Fig. 44 are given in Table. 4. The variable *d'* in Table. 4 is given by

$$d' = 1 - d \tag{126}$$

Assuming *d* to involve feedback of state variables, a generalized expression can be used for *d* in the form of

$$d = g(\mathbf{x}) \tag{127}$$

Since the system in (123) is non-linear, the chosen state feedback (127) should ensure the stability of the corresponding equilibrium point $\mathbf{X_{eq}}$. Stability of the equilibrium point $\mathbf{X_{eq}}$ can be estimated as follows. First, the duty cycle expression given by (127) is substituted in the system equations (123). Next, the expression for linearized system jacobian given by

$$\mathbf{A} = \left.\frac{\partial \mathbf{f}}{\partial \mathbf{x}}\right|_{\mathbf{x}=\mathbf{X_{eq}}} \tag{128}$$

(128) is calculated. As an example, the **A** matrix obtained in the case of a SEPIC converter is given by (129).

$$\mathbf{A} = \begin{bmatrix} \frac{(x_3+x_4)}{L_1}\frac{\partial g}{\partial x_1} & \frac{(x_3+x_4)}{L_1}\frac{\partial g}{\partial x_2} & \frac{(g-1)}{L_1} + \frac{(x_3+x_4)}{L_1}\frac{\partial g}{\partial x_3} & \frac{(g-1)}{L_1} + \frac{(x_3+x_4)}{L_1}\frac{\partial g}{\partial x_4} \\ \frac{(x_3+x_4)}{L_2}\frac{\partial g}{\partial x_1} & \frac{(x_3+x_4)}{L_2}\frac{\partial g}{\partial x_2} & \frac{g}{L_2} + \frac{(x_3+x_4)}{L_2}\frac{\partial g}{\partial x_3} & \frac{(g-1)}{L_2} + \frac{(x_3+x_4)}{L_2}\frac{\partial g}{\partial x_4} \\ \frac{(1-g)}{C_3} - \frac{(x_1+x_2)}{C_3}\frac{\partial g}{\partial x_1} & -\frac{1}{C_3}\left((x_1+x_2)\frac{\partial g}{\partial x_2} + g\right) & -\left(\frac{x_1+x_2}{C_3}\right)\frac{\partial g}{\partial x_3} & -\left(\frac{x_1+x_2}{C_3}\right)\frac{\partial g}{\partial x_4} \\ \frac{(1-g)}{C_4} - \frac{(x_1+x_2)}{C_4}\frac{\partial g}{\partial x_1} & \frac{(1-g)}{C_4} - \frac{(x_1+x_2)}{C_4}\frac{\partial g}{\partial x_2} & -\left(\frac{x_1+x_2}{C_4}\right)\frac{\partial g}{\partial x_3} & -\left(\frac{x_1+x_2}{C_4}\right)\frac{\partial g}{\partial x_4} + \frac{P}{C_4 x_4^2} \end{bmatrix} \tag{129}$$

It should be noted that, the terms in **A** matrix in the case of other two converters is also similar to (129). Among the necessary conditions to ensure that all the eigen values of **A** lie in the left half of *s* plane (LHS), one of the simple conditions is that

$$\text{trace}(\mathbf{A}) < 0 \tag{130}$$

To satisfy (130), one or more of the necessary conditions given by (131), (132) need to be satisfied.

$$\frac{\partial \mathbf{g}}{\partial x_i} < 0, \ i = 1,2 \tag{131}$$

$$\frac{\partial \mathbf{g}}{\partial x_i} > 0, \ i = 3,4 \tag{132}$$

	SEPIC	Cuk	Zeta
$L_1 \dot{x}_1$	$E - d'(x_3 + x_4)$	$E - d'x_3$	$dE - d'x_3$
$L_2 \dot{x}_2$	$dx_3 - d'x_4$	$-x_4 + dx_3$	$d(E + x_3) - x_4$
$C_3 \dot{x}_3$	$d'x_1 - dx_2$	$d'x_1 - dx_2$	$d'x_1 - dx_2$
$C_4 \dot{x}_4$	$d'(x_1 + x_2) - \frac{P}{x_4}$	$x_2 - \frac{P}{x_4}$	$x_2 - \frac{P}{x_4}$

Table 4: Average state equations for system in Fig. 44

To ensure condition (132), *g* has to involve positive feedback of the respective capacitor voltages. It should be noted that SEPIC and Cuk converters have their respective input modules identical to that of a boost converter and the input module of a Zeta converter is identical to that of a buckboost converter. Hence, to limit *d* from reaching higher values nearing 1, positive feedback of x_3 or x_4 may be avoided. This implies that *g* can involve feedback of either of inductor currents x_1, x_2 or both. This is equivalent to inserting a virtual resistance in series with the respective inductances. In a dc microgrid, there will a number of sources that interface through parallel connected LRCs at a common dc bus. To ensure that the control algorithm derived in this paper can be extended to such a parallel converter scenario, and to ensure the simplicity of control algorithm, let us assume that *g* involves feedback of either x_1 or x_2. Hence, there is a need to decide the

location to insert the virtual resistance. Among the two inductors, it is chosen to insert the virtual resistance in series with the input inductance, L_1, for the following reasons.

The current through L_1, x_1, is the input current for all the three converter configurations. When more converters are connected in parallel, this virtual resistance could as well serve as a droop resistance [38] enabling current sharing among converters.

Since the purpose of the virtual resistance is to damp limit cycle oscillations, the equilibrium point obtained after inserting the resistance has to be stable. However, for a given value of the damping resistance, there exists a maximum value of load power beyond which no stable equilibrium point exists. This is true both in the case of inserting virtual resistance in series with L_1or L_2. Assuming that the virtual resistance is inserted in series with L_2, the maximum load power, $P_{max,L2}$ is given by

$$P_{max,L2} = \frac{E^2\left([2-k]-2\sqrt{[1-k]}\right)}{R_d}, 0 < k < 1 \tag{133}$$

where k is the open loop duty ratio and R_d is the virtual droop resistance. Assume that same R_d is inserted in series with L_1. The maximum load that can be supplied at the microgrid while still ensuring that the corresponding equilibrium point is stable can be given by

$$P_{\max,L1} = \frac{E^2\left(1-\sqrt{(1-k)}\right)}{R_d} \tag{134}$$

such that $P_{max,L1} > P_{max,L2}$. It should be noted that load powers greater than $P_{max,L1}$ can be supplied by inserting the same R_d in series with L_1 but stability of the corresponding equilibrium point cannot be ensured.

Hence, the duty cycle d_1 for the switch during the first stage, active damping stage is designed as follows

$$d_1 = \frac{kE - x_1 R_d}{E}, 0 < d_1 < 1 \tag{135}$$

The resistance R_d in (135) is virtual in the sense that there is no real power loss in the resistor and it is implemented through control action. The equilibrium point obtained using the control input d_1 in (135) is given by $\mathbf{X_{eq,1}}$. The individual components of $\mathbf{X_{eq,1}}$ are referred by

$$\mathbf{X_{eq,1}} = \left[X_{1eq,1}, X_{2eq,1}, X_{3eq,1}, X_{4eq,1} \right]^T \tag{136}$$

The equilibrium point $\mathbf{X_{eq,1}}$ obtained in the case of all the three configurations .i.e. SEPIC, Cuk and Zeta is given in Table 5. Observing Table 5, one can notice that during the active damping stage, the equilibrium values of all state variables except x_3 are identical for all the three converter configurations. The equilibrium value of the state variable x_3, which is represented by $X_{3eq,1}$ is the voltage across the center capacitor namely C_3. The equilibrium values of the state variables x_1 and x_2 which are represented by $X_{1eq,1}$ and $X_{2eq,1}$ respectively are the input and the output currents of the converters in all the 3 converter configurations. By substituting the control input (135) in the system equation (123) and calculating the linearized system jacobian matrix **A** corresponding to the system described by (123), we can observe that the control input d_1 given by (135) is able to damp the limit cycle oscillations caused by the constant power loads of the dc microgrid buses. However the voltage at dc microgrid is reduced from the nominal voltage V_{nl} to $X_{4eq,1}$ where V_{nl} is the no load voltage of the dc microgrid which is given by

$$V_{nl} = \frac{kE}{(1-k)}, 0 < k < 1 \tag{137}$$

This deviation of microgrid voltage from V_{nl} to $X_{4eq,1}$ may be unacceptable. Further, the controller needs to ensure that deviations in load power and source voltages do not affect

the microgrid voltage. In order to ensure that the controller compensates for voltage deviations at the dc microgrid buses, an integral term needs to be added to the control input d_1 in (135) so that the total control input becomes

$$d = \frac{kE - x_1 R_d + k_i \int (V_{nl} - x_4)\, dt}{E} \tag{138}$$

where k_i is the integral control gain and d is the overall control input obtained by combing the first and second stages. The equilibrium point obtained using the overall control inputs d in (138) is given by $\mathbf{X_{eq,2}}$. The individual components of $\mathbf{X_{eq,2}}$ are referred by

$$\mathbf{X_{eq,2}} = \left[X_{1eq,2}, X_{2eq,2}, X_{3eq,2}, X_{4eq,2} \right]^T \tag{139}$$

The equilibrium point $\mathbf{X_{eq,2}}$ is obtained in the case of all the three configurations .i.e. SEPIC, Cuk and Zeta and is given in Table. 6. Observing Table. 6, one can notice that during the voltage regulation stage, the microgrid voltage is restored to V_{nl}. The observations regarding the state variables x_1, x_2 and x_3 as listed in the active damping stage hold true in the case of voltage regulation stage as well.

	SEPIC	Cuk	Zeta
$X_{1eq,1}$	$\frac{P}{E}$	$\frac{P}{E}$	$\frac{P}{E}$
$X_{2eq,1}$	$\frac{PE^2}{E\left(kE^2 - PR_d\right)} - \frac{P}{E}$	$\frac{PE^2}{E\left(kE^2 - PR_d\right)} - \frac{P}{E}$	$\frac{PE^2}{E\left(kE^2 - PR_d\right)} - \frac{P}{E}$
$X_{3eq,1}$	E	$\frac{E^3}{E^2(1-k) + PR_d}$	$\frac{E\left(kE^2 - PR_d\right)}{E^2(1-k) + PR_d}$
$X_{4eq,1}$	$\frac{E\left(kE^2 - PR_d\right)}{E^2(1-k) + PR_d}$	$\frac{E\left(kE^2 - PR_d\right)}{E^2(1-k) + PR_d}$	$\frac{E\left(kE^2 - PR_d\right)}{E^2(1-k) + PR_d}$

Table 5: Equilibrium point obtained after active damping stage for converters in Fig. 44

	SEPIC	Cuk	Zeta
$X_{1eq,2}$	$\frac{P}{E}$	$\frac{P}{E}$	$\frac{P}{E}$
$X_{2eq,2}$	$\frac{P}{V_{nl}}$	$\frac{P}{V_{nl}}$	$\frac{P}{V_{nl}}$
$X_{3eq,2}$	E	$V_{nl}+E$	V_{nl}
$X_{4eq,2}$	V_{nl}	V_{nl}	V_{nl}

Table 6: Equilibrium point obtained after voltage regulation stage for converters in fig. 44

STABILITY RESULTS

For the equiliubrium point $\mathbf{X_{eq,1}}$ to be locally asymptotically stable, the real part of the eigenvalues of the linearized version of matrix **A** given by (128) evaluated at $\mathbf{X_{eq,1}}$ need to be negative. Suppose now that the characteristic polynomial of the matrix **A** is of the form $s^4+a_3s^3+a_2s^2+a_1s+a_0$. Then the relevant conditions for asymptotic stability based on the Routh-stability criterion [67] indicates that $\mathbf{X_{eq,1}}$ is stable if the coefficients a_3, a_2, a_1 and a_0 are greater than zero. The conditions given by $a_3>0$ and $a_0>0$ are identical for all the 3 converters. The conditions given by $a_2>0$ and $a_1>0$ are identical for Cuk and Zeta converters while they are slightly different for SEPIC converter. The conditions common for all the 3 converters are given in (140), (141).

$$a_3 > 0 \Rightarrow \frac{R_d}{L_1}\left(1+\frac{X_{4eq,1}}{E}\right) > \frac{P}{C_4 X_{4eq,1}^2} \tag{140}$$

$$a_0 > 0 \Rightarrow$$

$$E^4 X_{4eq,1}^2 (1-k)^2 - PR_{d1}\begin{bmatrix} E^4 k + E^3 X_{4eq,1}(2k-1) + \\ 3E^2 X_{4eq,1}^2 (-1+k) \end{bmatrix} + (PR_d)^2 \left[E^2 + 2EX_{4eq,1} + 2X_{4eq,1}^2 \right] > 0 \tag{141}$$

The conditions $a_1>0$and $a_2>0$ for SEPIC converter are

$$a_1 > 0 \Rightarrow$$

$$\frac{1}{L_2 L_1 C_3}\left(kR_d - \frac{PR_d^2}{E^2} + \frac{R_d X_{4eq,1} k}{E} - \frac{PR_d^2 X_{4eq,1}}{E^3} \right) + \frac{1}{L_2 C_3 C_4}\left(-\frac{k^2 P}{X_{4eq,1}^2} - \frac{P^3 R_d^2}{E^4 X_{4eq,1}^2} + \frac{2kP^2 R_d}{\left(EX_{4eq,1}\right)^2} \right)$$

$$+ \frac{1}{L_1 C_3 C_4}\left(-\frac{P(1-k)^2}{X_{4eq,1}^2} - \frac{3P^2 R_d (1-k)}{\left(EX_{4eq,1}\right)^2} - \frac{P^2 R_d (1-k)}{EX_{4eq,1}^3} - \frac{2P^3 R_d^2}{E^4 X_{4eq,1}^2} - \frac{P^3 R_d^2}{\left(EX_{4eq,1}\right)^3} \right) > 0 \tag{142}$$

$$a_2 > 0 \Rightarrow$$

$$\frac{1}{L_2 C_3}\left(k^2 - \frac{2kPR_d}{E^2} + \frac{(PR_d)^2}{E^4} \right) + \frac{1}{L_1 C_3}\left(\begin{matrix} \frac{3PR_d(1-k)}{E^2} + \frac{PR_d(1-k)}{EX_{4eq,1}} \\ + \frac{2(PR_d)^2}{E^4} + \frac{(PR_d)^2}{E^3 X_{4eq,1}} + (1-k)^2 \end{matrix} \right) +$$

$$\frac{1}{L_1 C_4}\left(\begin{matrix} -\frac{PR_d}{X_{4eq,1}^2} - \frac{kPR_d}{EX_{4eq,1}} + (1-k)^2 \\ + \frac{3PR_d(1-k)}{E^2} + \frac{2(PR_d)^2}{E^4} + \frac{(PR_d)^2}{E^3 X_{4eq,1}} \end{matrix} \right) + \frac{1}{L_2 C_4}\left(\begin{matrix} \frac{2PR_d(1-k)}{E^2} + \\ \frac{(PR_d)^2}{E^4} + (1-k)^2 \end{matrix} \right) > 0 \tag{143}$$

The conditions given by $a_1>0$ and $a_2>0$ in the case of Cuk and Zeta converters are

$$a_1 > 0 \Rightarrow$$

$$\frac{1}{L_2 C_3 C_4}\left(-\frac{k^2 P}{X_{4eq,1}^2} - \frac{P^3 R_d^2}{E^4 X_{4eq,1}^2} + \frac{2kP^2 R_d}{\left(EX_{4eq,1}\right)^2} \right) + \frac{1}{L_2 L_1 C_3}\left(\begin{matrix} kR_d - \frac{PR_d^2}{E^2} + \frac{R_d X_{4eq,1} k}{E} \\ - \frac{PR_d^2 X_{4eq,1}}{E^3} \end{matrix} \right)$$

$$+ \frac{1}{L_1 C_3 C_4}\left(\begin{matrix} -\frac{P(1-k)^2}{X_{4eq,1}^2} - \frac{3P^2 R_d (1-k)}{\left(EX_{4eq,1}\right)^2} - \\ \frac{P^2 R_d (1-k)}{EX_{4eq,1}^3} - \frac{2P^3 R_d^2}{E^4 X_{4eq,1}^2} - \frac{P^3 R_d^2}{\left(EX_{4eq,1}\right)^3} \end{matrix} \right) + \frac{1}{L_2 L_1 C_4}\left(R_d + \frac{R_d X_{4eq,1}}{E} \right) > 0 \tag{144}$$

$$a_2 > 0 \Rightarrow$$

$$\frac{1}{L_2 C_3}\left(k^2 - \frac{2kPR_d}{E^2} + \frac{(PR_d)^2}{E^4} \right) + \frac{1}{L_1 C_4}\left(-\frac{PR_d}{X_{4eq,1}^2} - \frac{PR_d}{EX_{4eq,1}} \right)$$

$$+ \frac{1}{L_2 C_4} + \frac{1}{L_1 C_3}\left(\begin{matrix} \frac{3PR_d(1-k)}{E^2} + \frac{PR_d(1-k)}{EX_{4eq,1}} \\ + \frac{2(PR_d)^2}{E^4} + \frac{(PR_d)^2}{E^3 X_{4eq,1}} + (1-k)^2 \end{matrix} \right) > 0 \tag{145}$$

The condition (140) is similar to the condition derived in [17] where it has been suggested that stability can be achieved in dc microgrids if resistive loads are higher than

the CPLs. The condition (131) can be satisfied qualitatively by choosing higher values for the capacitors and lower values for the inductors [17]. One of the main observations is that for stability of equilibrium point $\mathbf{X_{eq,1}}$, the center capacitor C_3 has to be designed smaller in the case of Cuk and Zeta converters than in the case of SEPIC converter.

It should be noted that each of the converters given in Fig. 44 is a fourth order system. However, after the addition of integral controller in the voltage regulation stage given by (138), each of the converters becomes a fifth order system. Hence, it is difficult to derive general stability conditions. Further assuming that the system characteristic equation is now given by $s^5+b_4s^4+b_3s^3+b_2s^2+b_1s+b_0$, the necessary conditions given by $b_4...b_0>0$ do not provide any condition on the integral control gain k_i. So stability can be ascertained for individual cases as follows. The linearized system jacobian, now given by $\mathbf{A_{new}}$ which is a 5x5 matrix is calculated. The eigen values of $\mathbf{A_{new}}$ are evaluated at $X_{eq,2}$ to verify if all of them lie on the left half of the s plane

SIMULATION AND EXPERIMENTAL RESULTS

Simulation results

The previous analysis was verified by simulation and experiments on all three converter configurations. The system and control parameters for each converter in Fig. 44 are given in Table. 7. Initially, the system is simulated in open loop with open loop duty ratios given by k. It can be observed from Figs. 45, 47 and 49 that initially x_1 and x_4 exhibit limit cycle oscillations about their respective equilibrium points given in Table. 6. Active damping virtual resistors given by R_d are switched (through control action) at t=0.35s in order to damp the limit cycle oscillations. The transition of SEPIC, Cuk and Zeta converters from open loop to active damping stage can be observed in Figs. 45, 47 and. 49 respectively. Once the active damping controller is switched on, limit cycle

oscillations are damped in about 30ms for all 3 converter configurations. The state variables x_1 and x_4 settle down at the equilibrium values given by $X_{1eq,1}$ and $X_{4eq,1}$ respectively which are shown in Table. 5. It should be noted from Figs. 45, 47 and 49, that the controller given by (135) damps the limit cycle oscillations but causes deviation in the microgrid voltage from V_{nl}. In order to restore the microgrid voltage to V_{nl} and to maintain the same in the event of source voltage or load changes, it is necessary to switch on the next control stage namely voltage regulation stage. This stage consists of adding integral controllers with appropriate gains to the active damping stage given by (135). The overall control algorithm is now given by (138). Simulation results for transition from active damping stage to voltage regulation stage for SEPIC, Cuk and Zeta converters are given in Figs 46, 48 and 50 respectively. It can be observed from Figs 46, 48 and 50 that microgrid voltage is restored to V_{nl} in about 50ms. It should be noted that the current x_1 represents the input current of the converter for all the 3 configurations. Hence, there is no change in the equilibrium value of x_1 from the active damping stage to the voltage regulation stage indicating that the load being supplied is CPL.

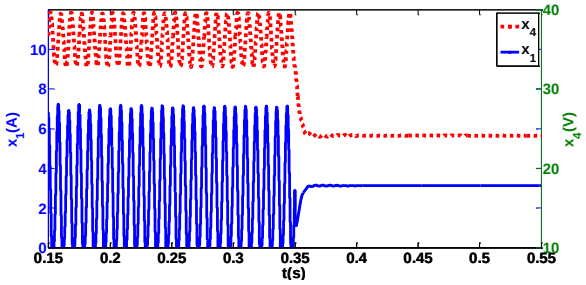

Fig. 45. Simulated results for transition of SEPIC converter from open loop to active damping stage

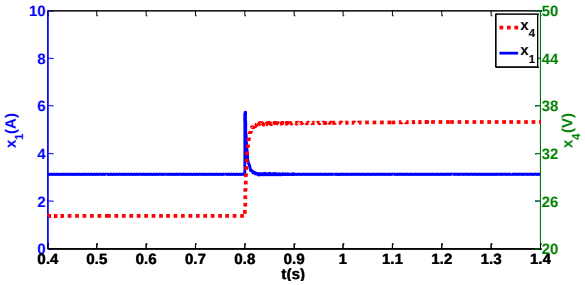

Fig. 46. Simulated results for transition of SEPIC converter from active damping stage to voltage regulation stage

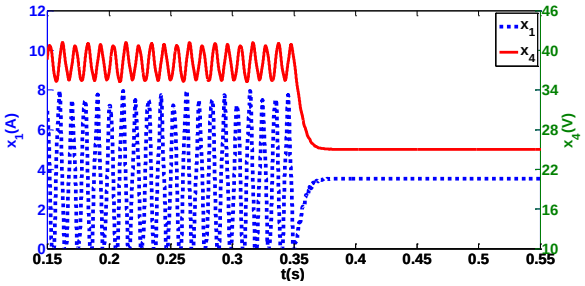

Fig. 47. Simulated results for transition of Cuk converter from open loop to active damping stage

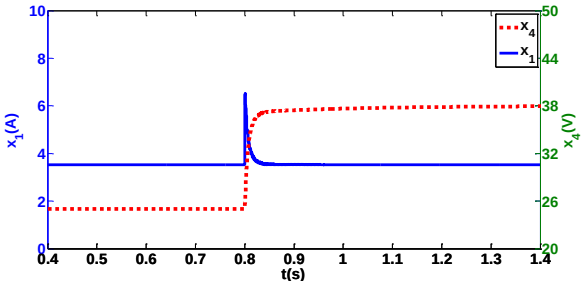

Fig. 48. Simulated results for transition of Cuk converter from active damping stage to voltage regulation stage

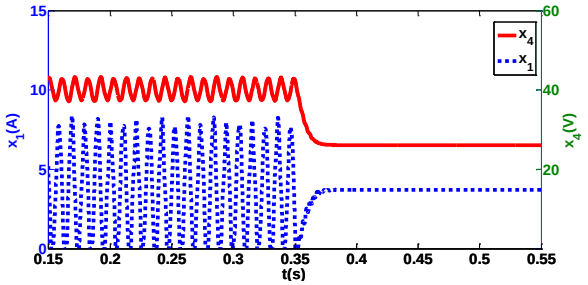

Fig. 49. Simulated results for transition of Zeta converter from open loop to active damping stage

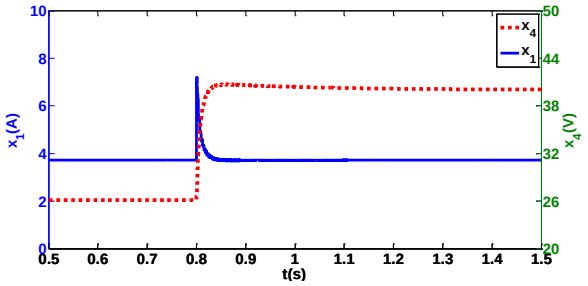

Fig. 50. Simulated results for transition of Zeta converter from active damping stage to voltage regulation stage

Parameter	SEPIC	Cuk	Zeta
E(V)	32	34	35
L_1(μH)	650	600	600
L_2(μH)	600	650	650
C_3(μF)	600	200	200
C_4(μF)	1200	1650	1650
P(W)	100	120	130
R_d(Ω)	1.02	1	1
V_{nl}(V)	36	38	40
k	0.529	0.528	0.533
k_i	0.97	0.97	0.9
Equilibrium point during active damping stage			
$X_{1eq,1}$(A)	3.13	3.53	3.71
$X_{4eq,1}$(V)	24.12	25.02	26.1
Equilibrium point during voltage regulation stage			
$X_{1eq,2}$(A)	3.13	3.53	3.71
$X_{4eq,2}$(V)	36	38	40
Line and load regulation			
$X_{1eq,line}$(A)	4.17	4.62	4.81
$X_{1eq,load}$(A)	4.38	4.71	4.86

Table 7: Circuit parameters and equilibrium points for simulation and experiments

Experimental results

For experiments, Texas instruments based TM4C123 launchpad is used for digital control of the converters. The above mentioned launchpad is a low cost microcontroller with a 80MHz clock consisting of 16 PWM channels, 2 ADC modules, 12 general purpose timer modules (GPTM) and 78 different interrupts supported through a nested vector interrupt control (NVIC) module [76]. In addition to the same, it also implements several other useful features including a Controller area network (CAN) communication interface [75]. Such a communication scheme may prove useful for communication between parallel connected converters in a microgrid [33]. The CPL is realized by loading the microgrid with a buck converter whose output voltage is maintained constant using a fast regulating PI controller. Such a converter is also called point of load (POL) converter [18]. The parameters of the POL buck converter are as follows. L_L=300μH, C_L=1680μF, R_L=2Ω. The voltage across the load resistor R_L given by V_L. The switching frequency of LRC converter is fixed at 10kHz and that of POL converter is 20kHz. The parameters of the experimental microgrid are identical to the simulation parameters. The results of the evaluation of the controller damping action due to the virtual resistance are shown in Figs. 51, 55 and 59 for SEPIC, Cuk and Zeta converters respectively. Experimental results for transition from active damping stage to voltage regulation stage are shown in Figs. 52, 56 and 60 for SEPIC, Cuk and Zeta converters respectively. In both the cases, experimental results obtained are identical to simulation results.The integral control term in (138) also enables line and load regulation. Line regulation results are shown in the Figs. 53, 57 and 61. The source voltage E is reduced by 8V for each of the converters. It can be observed from Figs. 53, 57 and 61 that x_1 increases from $X_{1eq,2}$ to $X_{1eq,line}$ whose values are given in Table. 7. The dc microgrid voltage is held constant at V_{nl}. The response time for the controller is around 150ms. Load regulation was tested by

increasing the load for each of the converters by 40W and the results are shown in the Figs. 54, 58 and 62. From Figs 54, 58 and 62, it can be observed that x_1 increases from $X_{1eq,2}$ to $X_{1eq,load}$ (values given in Table. 7). The microgrid voltage x_4 is held constant at V_{nl}.

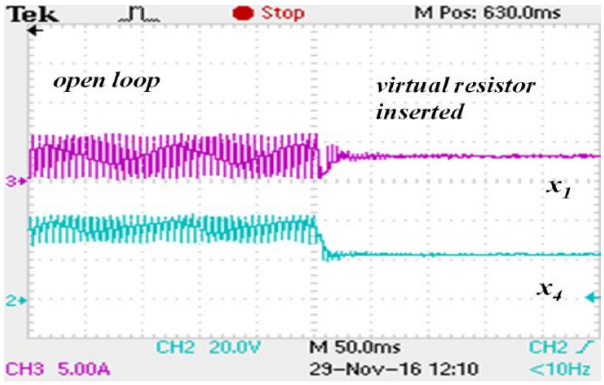

Fig. 51 Experimental results of transition of SEPIC converter from open loop to active damping stage

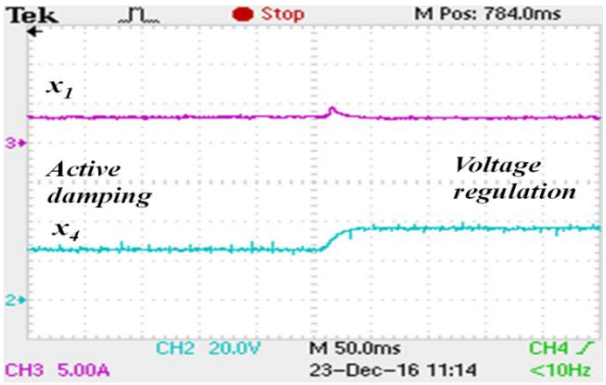

Fig. 52. Experimental results of transition of SEPIC converter from active damping stage to voltage regulation

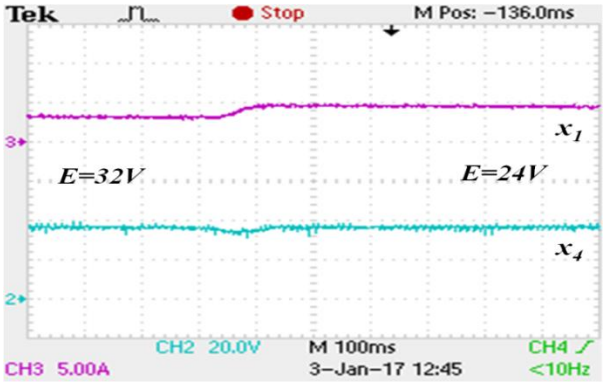

Fig. 53. SEPIC converter experimental waveforms showing line regulation

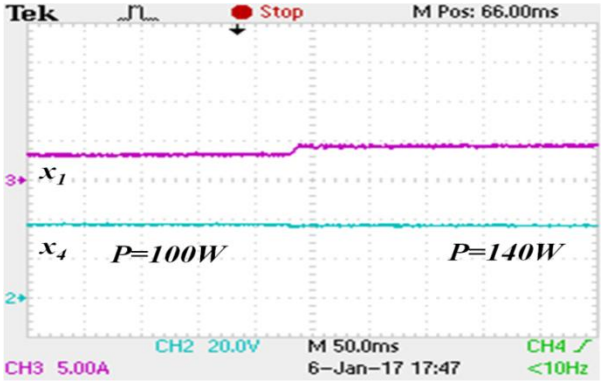

Fig. 54. SEPIC converter experimental waveforms showing load regulation

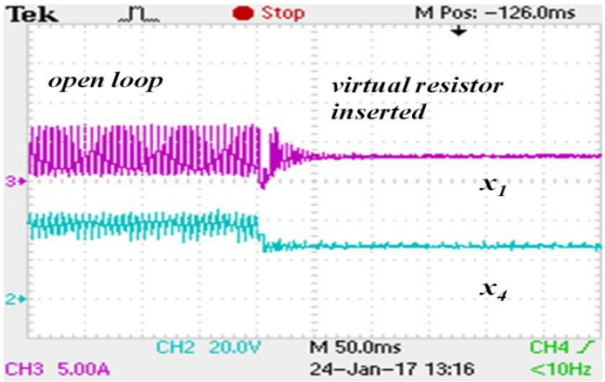

Fig.55. Experimental results of transition of Cuk converter from open loop to active damping stage

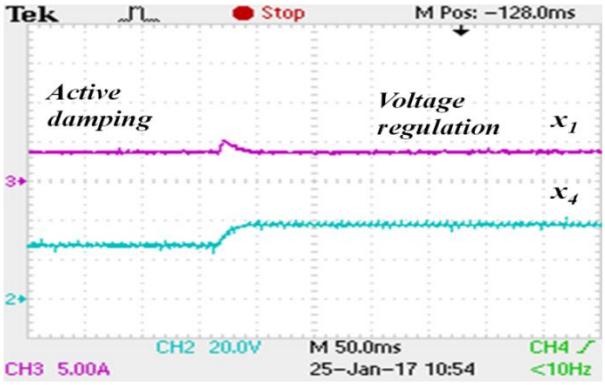

Fig. 56. Experimental results of transition of Cuk converter from active damping stage to voltage regulation stage

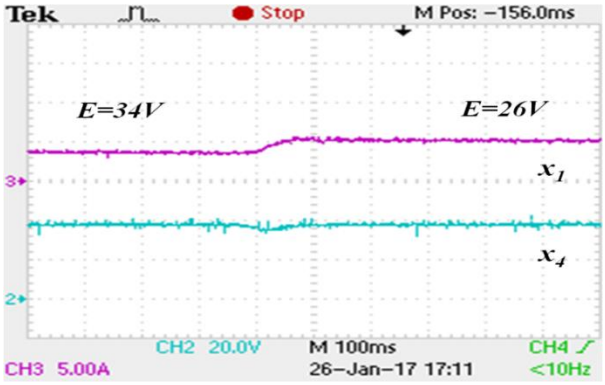

Fig. 57. Cuk converter experimental waveforms showing line regulation

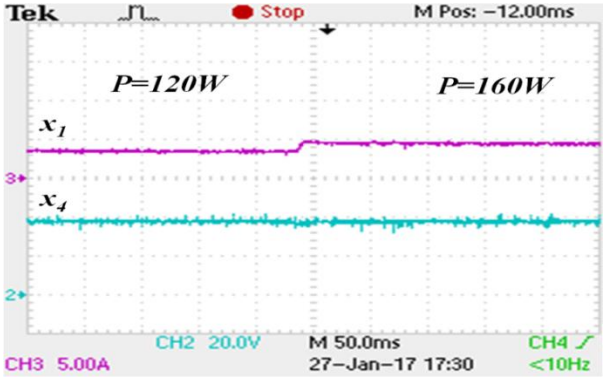

Fig. 58 Cuk converter experimental waveforms showing load regulation

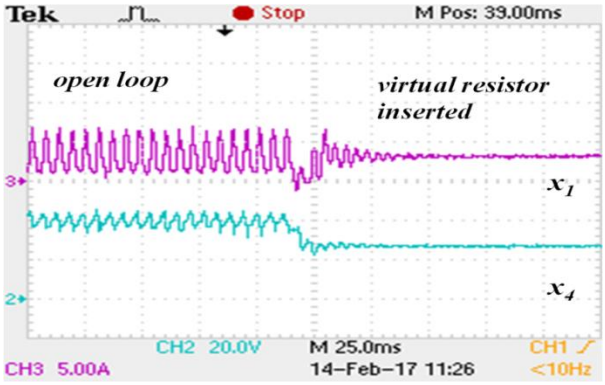

Fig. 59. Experimental results of transition of Zeta converter from open loop to active damping stage

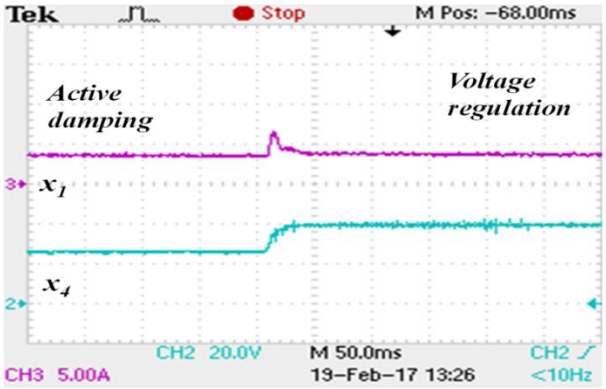

Fig. 60. Experimental results of transition of Zeta converter from active damping stage to voltage regulation stage

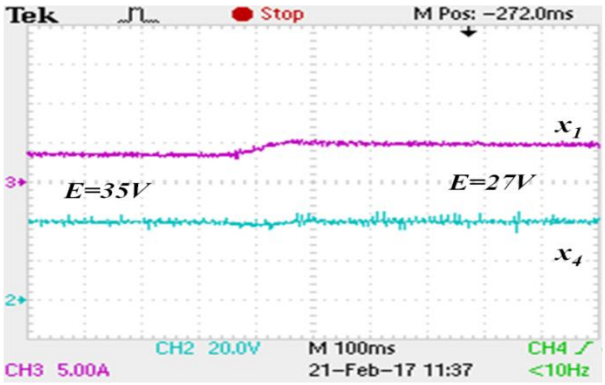

Fig. 61. Zeta converter experimental waveforms showing line regulation

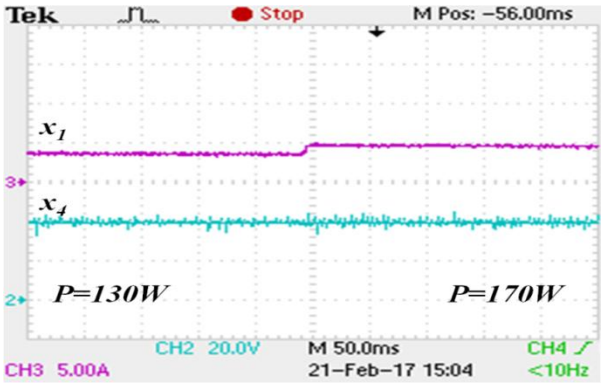

Fig. 62. Zeta converter experimental waveforms showing load regulation

SUMMARY

An active linear damping scheme is developed for a dc microgrid with higher order dc-dc converters like SEPIC, Cuk and Zeta supplying constant power loads. The controller implementation is carried out in two stages. The first stage involves a proportional negative feedback of the input inductor current of the converter. This stage, referred to as active damping stage enables damping the limit cycle oscillations due to CPL. The second stage involves the addition of an integral controller to the active damping stage. The second stage, referred to as voltage regulation stage enables in restoring and maintaining the microgrid voltage within acceptable limits. Stability conditions for the equilibrium points are derived. The proposed control scheme is verified by simulation and experimental results.

Chapter 6: Calculation of Loadability in a Droop Controlled DC Microgrid with Constant Power Loads[4]

PROBLEM DESCRIPTION

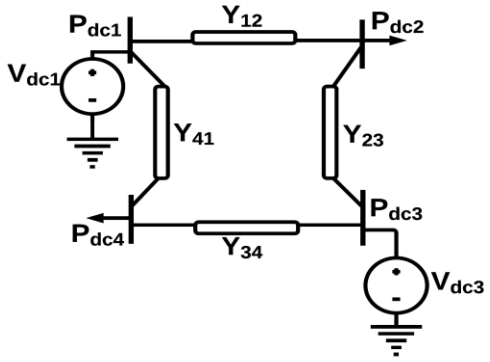

Figure. 63. A 4 bus DC microgrid [77]

Consider a general '*n*' bus dc microgrid where the sources are droop controlled. The loads in the microgrid are instantaneous constant power loads (CPLs). The variables representing each bus '*i'* of the system are the power injected by the bus, $P_{dc,i}$ and the voltage at the bus, $V_{dc,i}$. Depending on the variables specified at a bus, two kinds of buses can be defined for such a system [77].

1. Voltage drooped bus - In this bus, both $V_{dc,i}$ and $P_{dc,i}$ are unknown. A voltage drooped bus is analogous to the generator (PV) bus in a conventional power system. However, since this bus is connected to the voltage source through an actual or a virtual droop resistance [38], voltage at this bus is unknown.

[4] Contents of this chapter are published in "Calculation of Loadability in a Droop Controlled DC Microgrid with Constant Power Loads", Proc. Power Electronics for Distributed Generation Systems (PEDG) 2015, pp. 1-7, where Mahesh Srinivasan is the first author

2. Constant power bus - In this bus, $V_{dc,i}$ is unknown whereas $P_{dc,i}$ is assumed to be known. A constant power bus is analogous to the load (PQ) bus in a conventional power system.

Thus, the equations [77] that can be defined at a bus i of the system are given by

$$g_i(\mathbf{u}): V_{dc,i} - V_{nl,i} + \left(\frac{P_{dc,i}}{V_{dc,i}}\right) R_{di} = 0 \tag{146}$$

$$f_i(\mathbf{u}): \left(\frac{P_{dc,i}}{V_{dc,i}}\right) - \sum_{j=1}^{n} Y_{mat(i,j)} V_{dc,j} = 0 \tag{147}$$

In (146), $V_{nl,i}$ refers to the no load voltage at the i^{th} bus. The droop resistance of the generator at the same bus is denoted by R_{di}. In (147), $Y_{mat(i,j)}$ denotes the element in the i^{th} row and j^{th} column of the Y bus matrix. The equation (146) denoted by g_i is the voltage droop equation and is defined only at the voltage drooped bus. The equation (147) denoted by f_i is the KCL equation at the i^{th} bus and is defined at all the buses in the system [77]. Let the vector of voltage droop equations at all the voltage drooped buses be represented as **g** and the vector of KCL equations at all the buses be denoted **f**. The vector of unknowns in the system is denoted by **u** which consists of voltages at all the buses and the power injected at the voltage drooped buses**.** If there are local CPLs present at the voltage drooped buses, (146) gets modified as

$$g_i(\mathbf{u}): V_{dc,i} - V_{nl,i} + \left(\frac{P_{dc,i} + P_{ld,i}}{V_{dc,i}}\right) R_{di} = 0 \tag{148}$$

where $P_{ld,i}$ is the known value of CPL present at bus i. However, the aim of this paper is to adopt the algorithm in [78] to find the loadability at a constant power bus. So, it can be assumed that there are no local CPLs present at the voltage drooped buses without loss of generality. For a system containing n_1 voltage drooped buses and n_2 constant power buses, there exist $2n_1+n_2$ equations and $2n_1+n_2$ unknowns. To obtain the power flow solution, these $2n_1+n_2$ nonlinear equations are solved iteratively [77].

The generalized circle diagram approach proposed in [78] is not generally considered as a method for finding the loadability. It is shown in this paper that the algorithm proposed in [78] can be adopted to determine the maximum real power load that can be supplied at a constant power bus. A brief version of the algorithm in [78] is presented here for facilitating easy discussion. The notations and terminology used in the next paragraph and subsections correspond to those used in [78].

Power flow equations can be described by a vector of equations of the form

$$\begin{aligned} &\mathbf{F(u,k)} = \mathbf{0} \\ &\mathbf{u} \in \mathbb{R}^{n\times 1}, \mathbf{k} \in \mathbb{R}^{m\times 1} \end{aligned} \tag{149}$$

where **F** is a vector of *n* nonlinear equations, **u** is the vector of unknown parameters and **k** is the vector of known parameters. To study the response of the vector of unknowns **u** to the changes in the vector of knowns **k**, a target function of the form $T(\mathbf{u},\mathbf{k})$ is introduced**.** The algorithm proposed in [78] determines the response of the target function *T* when only two of the elements of **k** are varied, the others being held constant. When the function *T* is maintained at a constant value *t*, the set of equations can be defined as

$$\mathbf{F}(\mathbf{u}, x, y, \mathbf{k}') = 0 \tag{150}$$

$$T(\mathbf{u}, x, y, \mathbf{k}') = t \tag{151}$$

where *x* and *y* are the variable parameters in **k** and **k'** is the result of removing *x* and *y* from **k**. For each value of *t*, (150) and (151) constitute a contour because they contain *n+2* unknowns (**u**, *x* and *y*) and *n+1* constraints (**F** and *T*). This contour can be represented in two dimensions in the plane of the two varying parameters namely *x* and *y*. Tracing any contour involves the following steps [78].

1. Obtaining the first point on the contour.

2. Tracing the subsequent points on the contour.

The two steps are illustrated in Fig.64

Getting the First Point on the Contour

Let

$$\boldsymbol{\omega} = (\mathbf{u}, x, y) \tag{152}$$

$$\mathbf{G} = (\mathbf{F}, T) \tag{153}$$

$$\mathbf{g} = (0, 0, 0, \ldots\ldots, t) \tag{154}$$

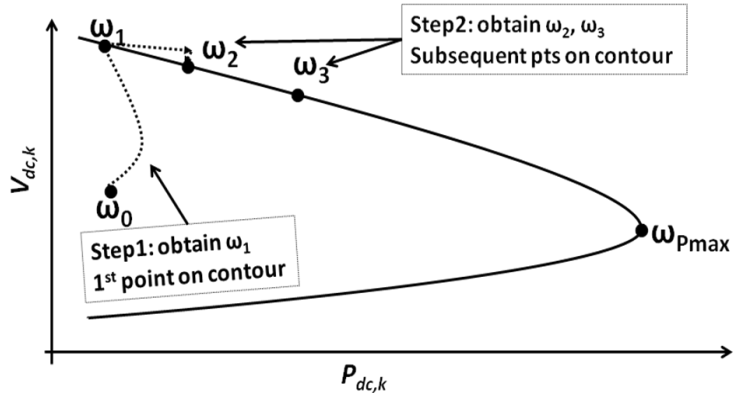

Figure. 64. Illustration of the steps in generalized circle diagram approach

The equations (152), (153) and (154) together are written as

$$\mathbf{G}(\boldsymbol{\omega}) = \mathbf{g} \tag{155}$$

In (155), **k'** has been omitted because it is a constant. Defining

$$H_{ij} = \frac{\partial G_i}{\partial \omega_j} \tag{156}$$

where i=1, 2, 3…n+1 and j=1, 2, 3…n+2. At the start of the iteration, an arbitrary point $\boldsymbol{\omega_0}$ can be obtained using a power flow program. The first point on the contour is obtained by successively updating $\boldsymbol{\omega_0}$ till convergence such that

$$\omega^{m+1} = \omega^m + H^*(\omega^m)\left[g - G(\omega^m)\right] \tag{157}$$

where $H^*(\omega^m)$ is the pseudo-inverse of $H(\omega^m)$.

Getting the subsequent points on the contour

Suppose the first point on the contour is $\boldsymbol{\omega_1}$, the subsequent points on the contour are obtained as follows [78]. The H matrix (156) is calculated at $\boldsymbol{\omega_1}$ and its singular value decomposition (SVD) is performed [79]. Thus

$$H = USV^T \tag{158}$$

where S is a diagonal matrix of the same dimension of H and with non-negative diagonal elements in the decreasing order which are the singular values of the matrix H. U and V are unitary square matrices having the dimensions (n+1)x(n+1) and (n+2)x(n+2) respectively. The last column of the V matrix is the tangent at $\boldsymbol{\omega_1}$ in the direction of the contour namely $\boldsymbol{\alpha_1}$. The equation of the plane at a distance s from $\boldsymbol{\omega_1}$ along $\boldsymbol{\alpha_1}$ and perpendicular to $\boldsymbol{\alpha_1}$ is given by

$$\alpha_1 \bullet \omega = \alpha_1 \bullet \omega_1 + s \tag{159}$$

It can be observed that (155) and (159) together constitute n+2 equations with n+2 unknowns. A step length of s is used as the distance moved along $\boldsymbol{\alpha_1}$. The initial point is taken as $\boldsymbol{\omega_1 + s\alpha_1}$.The equations (155) together with (159) are solved by the NR method. The solution constitutes the next point on the contour namely $\boldsymbol{\omega_2}$. An illustration of this step is given in the Fig. 65. Step 2, described in this section can be repeated to obtain the successive points on the contour.

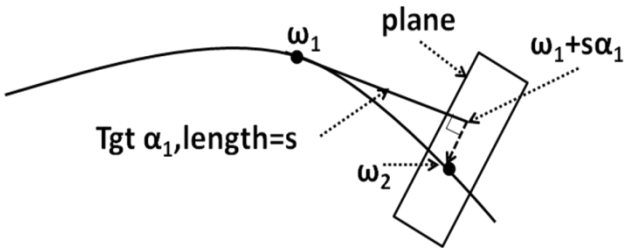

Fig. 65. Illustration of step 2 of generalized circle diagram approach [78]

ADOPTING PRICE METHOD TO FIND LOADABILITY

The system equations (146), (147) have to be modified in order to apply the generalized circle diagram approach to find the loadability. Thus

$$g_i(\mathbf{u}): V_{dc,i}^2 - V_{nl,i}V_{dc,i} + P_{dc,i}R_{di} = 0 \tag{160}$$

$$f_i(\mathbf{u}): P_{dc,i} - V_{dc,i}\sum_{j=1}^{n} Y_{mat(i,j)}V_{dc,j} = 0 \tag{161}$$

Let the constant power bus where the loadability has to be obtained be bus *q*. Instead of choosing both the parameters *x* and *y* from the vector of known parameters **k**, one of the parameters is chosen from **u** (a dependent variable) and the other is chosen from **k** as the power injected at the bus *q*. This step is different from the algorithm presented in the previous section. Thus *x* and *y* are given by (162) and (163) respectively.

$$x = P_{dc,q} \in \boldsymbol{k} \tag{162}$$

$$y = V_{dc,q} \in \mathbf{u} \tag{163}$$

The vector **F** (149) consists of the voltage droop equations **g** at all the voltage droop buses and the KCL equations **f** at all the buses except at a constant power bus *r* (which should be different from bus *q*). The choice of this constant power bus *r* is arbitrary. The KCL equation at bus *r* is the target equation *T* (151). The vector of unknowns **u** consists of the voltages at all the buses except bus *q* and the real power injected at all the voltage drooped buses. Let the variable *x* in (162) be denoted λ. The vector **k'** consists of the

known parameters such as the real power injected at all the constant power buses except bus q, line conductances which can be obtained from the Y_{bus} matrix, virtual droop resistances and the no-load voltages at the voltage drooped buses. The vector of unknown bus voltages taken together from **u** and y is denoted as $\mathbf{V_{dc}}$ while the vector of real power injected taken from **u** alone is denoted $\mathbf{P_{dc}}$. The equations (152)-(155) get modified as follows.

$$\boldsymbol{\omega} = (\mathbf{P_{dc}}, \mathbf{V_{dc}}, \lambda) \tag{164}$$

$$\mathbf{G} = (\mathbf{F}, T) \tag{165}$$

$$\mathbf{g} = (0, 0, 0, ..., 0) \tag{166}$$

$$\mathbf{G}(\mathbf{P_{dc}}, \mathbf{V_{dc}}, \lambda) = \mathbf{g} \tag{167}$$

Using (156) and (164), the H matrix now becomes

$$H = \left[\frac{\partial \mathbf{G}}{\partial \mathbf{P_{dc}}}, \frac{\partial \mathbf{G}}{\partial \mathbf{V_{dc}}}, \frac{\partial \mathbf{G}}{\partial \lambda} \right] \tag{168}$$

It should be noted that the matrix H (168) is rectangular having one column more than the number of rows. The matrix H (168) is the power flow jacobian augmented by one column which has zeros for all the rows except a 1 for the row corresponding to the KCL equation for bus q whose maximum value has to be calculated. The matrix H (168) is sparse whose terms can be calculated from (156) as follows.

$$\frac{\partial g_i}{\partial P_{dc,j}} = \begin{cases} R_{di} \text{ if } i = j \\ 0 \text{ otherwise} \end{cases} \tag{169}$$

$$\frac{\partial f_i}{\partial P_{dc,j}} = \begin{cases} 1 \text{ if } i = j \\ 0 \text{ otherwise} \end{cases} \tag{170}$$

$$\frac{\partial g_i}{\partial V_{dc,j}} = \begin{cases} 2V_{dc,i} - V_{nl,i} \text{ if } i = j \\ 0 \text{ otherwise} \end{cases} \tag{171}$$

$$\frac{\partial f_i}{\partial V_{dc,j}} = \begin{cases} -2Y_{mat(i,i)}V_{dc,i} - \sum_{\substack{i=1 \\ i \neq j}}^{n} Y_{mat(i,j)}V_{dc,j} \text{ if } i = j \\ -Y_{mat(i,j)}V_{dc,i} \text{ otherwise} \end{cases} \tag{172}$$

$$\frac{\partial g_i}{\partial \lambda} = 0 \tag{173}$$

$$\frac{\partial f_i}{\partial \lambda} = \begin{cases} 1 \text{ if } i = q \\ 0 \text{ otherwise} \end{cases} \tag{174}$$

In the case of conventional power flow in ac systems, symmetry properties of the jacobian terms could be exploited by normalizing the bus voltages to reduce the computational effort [80]. However, the effort involved in calculating H (168) in the case of a droop controlled DC microgrid cannot be reduced further.

To obtain the first point on the contour, a detailed procedure (briefly described in the previous section) is proposed in [78]. However, since it is desired to obtain the maximum real power that can be supplied at a constant power bus q, the first point on the contour can be obtained by the power flow program [77] directly by fixing $P_{ld,q}$ at a small value. This provides considerable simplicity to the method. After the first point on the contour, $\boldsymbol{\omega_1}$ is obtained, the subsequent points have to be traced. Using the H matrix, the tangent at $\boldsymbol{\omega_1}$ namely $\boldsymbol{\alpha_1}$ is obtained which is of the form

$$\boldsymbol{\alpha}_1 = \begin{bmatrix} \mathbf{dP}_{\mathbf{dc1}} \\ \mathbf{dV}_{\mathbf{dc1}} \\ \mathrm{d}\lambda_1 \end{bmatrix} \tag{175}$$

The equation of the plane at a distance s from $\boldsymbol{\omega_1}$ along $\boldsymbol{\alpha_1}$ is given by (159). The equation (159) can be rewritten as

$$\begin{bmatrix} \mathbf{dP}_{\mathbf{dc1}} \\ \mathbf{dV}_{\mathbf{dc1}} \\ \mathrm{d}\lambda_1 \end{bmatrix} \bullet \begin{bmatrix} \mathbf{P}_{\mathbf{dc}} \\ \mathbf{V}_{\mathbf{dc}} \\ \lambda \end{bmatrix} = \begin{bmatrix} \mathbf{dP}_{\mathbf{dc1}} \\ \mathbf{dV}_{\mathbf{dc1}} \\ \mathrm{d}\lambda_1 \end{bmatrix} \bullet \begin{bmatrix} \mathbf{P}_{\mathbf{dc1}} \\ \mathbf{V}_{\mathbf{dc1}} \\ \lambda_1 \end{bmatrix} + s \tag{176}$$

In (176), the step length is to be specified. Equation (167) has one unknown more than the number of equations. The equation (167) can be combined with (176) and solved iteratively taking $\boldsymbol{\omega_1}+s\boldsymbol{\alpha_1}$ as the initial guess to get the subsequent point $\boldsymbol{\omega_2}$ as given in (177).

$$\begin{bmatrix} G(\boldsymbol{\omega}) \\ \boldsymbol{\alpha}_1 \bullet \boldsymbol{\omega} \end{bmatrix} = \begin{bmatrix} \mathbf{g} \\ \boldsymbol{\alpha}_1 \bullet \boldsymbol{\omega}_1 + s \end{bmatrix} \tag{177}$$

SIMULATION RESULTS

The methods discussed earlier are illustrated and are used to obtain $P_{ld,2}$ *Vs* $V_{dc,2}$ contour for the 4 bus system in Fig. 63 [77]. In this system, buses 1 and 3 are voltage drooped buses and buses 2 and 4 are constant power buses. All the line resistances are 0.05Ω and the rest of the parameters are listed in Table. 8. The low line resistance values provide some important observations about the proposed method which will be explained at the end of this section. The value of $P_{ld,4}$ is maintained constant at 697.5W and is considered as the target equation in the algorithm in [78] and the corresponding equations are

$$F_1(\mathbf{u}, x, y, \mathbf{k}') : V_{dc,1}^2 - V_{nl,1}V_{dc,1} + P_{dc,1}R_{d1} = 0 \tag{178}$$

$$F_2(\mathbf{u}, x, y, \mathbf{k}') : V_{dc,3}^2 - V_{nl,3}V_{dc,3} + P_{dc,3}R_{d3} = 0 \tag{179}$$

$$F_3(\mathbf{u}, x, y, \mathbf{k}') : P_{dc,1} - V_{dc,1}\sum_{j=1}^{4} Y_{mat(1,j)}V_{dc,j} = 0 \tag{180}$$

$$F_4(\mathbf{u}, x, y, \mathbf{k}') : \lambda - V_{dc,2}\sum_{j=1}^{4} Y_{mat(2,j)}V_{dc,j} = 0 \tag{181}$$

$$F_5(\mathbf{u}, x, y, \mathbf{k}') : P_{dc,3} - V_{dc,3}\sum_{j=1}^{4} Y_{mat(3,j)}V_{dc,j} = 0 \tag{182}$$

$$T(\mathbf{u}, x, y, \mathbf{k}') : -697.5 - V_{dc,4}\sum_{j=1}^{4} Y_{mat(4,j)}V_{dc,j} = 0 \tag{183}$$

where **u**, *x*, *y* and **k'** are identical to those explained in the previous section. Thus

$$\begin{aligned} \mathbf{u} &= \left[P_{dc,1}, P_{dc,3}, V_{dc,1}, V_{dc,3}, V_{dc,4}\right] \\ x &= \lambda \\ y &= V_{dc,2} \end{aligned} \tag{184}$$

The aim of this study is to trace the contour of operating points for increasing values of load at bus 2 namely $P_{ld,2}$=-($P_{dc,2}$). The first step of the algorithm is to obtain the first point on the contour, namely $\boldsymbol{\omega_1}$, from an arbitrary point $\boldsymbol{\omega_0}$. An arbitrary point $\boldsymbol{\omega_0}$, given in Table 9, is chosen. Using (157), the first point on the contour namely $\boldsymbol{\omega_1}$ is calculated which is also given in Table 9. The point $\boldsymbol{\omega_1}$ is verified to lie on the contour using the power flow program [77]. In this paper, it is intended to obtain the maximum

value of P_{ld2}. As explained in the previous section, a small load of 108.702W can be inserted in bus 2 and the initial point on the contour $\boldsymbol{\omega_1}$ can be obtained directly using the power flow program [77].

To obtain the subsequent point on the contour, the tangent at $\boldsymbol{\omega_1}$ namely $\boldsymbol{\alpha_1}$ has to be obtained. To obtain the tangent, the H matrix (156) has to be calculated at $\boldsymbol{\omega_1}$. The symbol λ in (181) and (184) is $P_{dc,2}$ The structure of the H matrix is as follows.

$$H = \begin{bmatrix} \frac{\partial F_1}{\partial P_{dc,1}} & \frac{\partial F_1}{\partial P_{dc,3}} & \frac{\partial F_1}{\partial V_{dc,1}} & \frac{\partial F_1}{\partial V_{dc,3}} & \frac{\partial F_1}{\partial V_{dc,4}} & \frac{\partial F_1}{\partial P_{dc,2}} & \frac{\partial F_1}{\partial V_{dc,2}} \\ \frac{\partial F_2}{\partial P_{dc,1}} & \frac{\partial F_2}{\partial P_{dc,3}} & \frac{\partial F_2}{\partial V_{dc,1}} & \frac{\partial F_2}{\partial V_{dc,3}} & \frac{\partial F_2}{\partial V_{dc,4}} & \frac{\partial F_2}{\partial P_{dc,2}} & \frac{\partial F_2}{\partial V_{dc,2}} \\ \frac{\partial F_3}{\partial P_{dc,1}} & \frac{\partial F_3}{\partial P_{dc,3}} & \frac{\partial F_3}{\partial V_{dc,1}} & \frac{\partial F_3}{\partial V_{dc,3}} & \frac{\partial F_3}{\partial V_{dc,4}} & \frac{\partial F_3}{\partial P_{dc,2}} & \frac{\partial F_3}{\partial V_{dc,2}} \\ \frac{\partial F_4}{\partial P_{dc,1}} & \frac{\partial F_4}{\partial P_{dc,3}} & \frac{\partial F_4}{\partial V_{dc,1}} & \frac{\partial F_4}{\partial V_{dc,3}} & \frac{\partial F_4}{\partial V_{dc,4}} & \frac{\partial F_4}{\partial P_{dc,2}} & \frac{\partial F_4}{\partial V_{dc,2}} \\ \frac{\partial F_5}{\partial P_{dc,1}} & \frac{\partial F_5}{\partial P_{dc,3}} & \frac{\partial F_5}{\partial V_{dc,1}} & \frac{\partial F_5}{\partial V_{dc,3}} & \frac{\partial F_5}{\partial V_{dc,4}} & \frac{\partial F_5}{\partial P_{dc,2}} & \frac{\partial F_5}{\partial V_{dc,2}} \\ \frac{\partial T}{\partial P_{dc,1}} & \frac{\partial T}{\partial P_{dc,3}} & \frac{\partial T}{\partial V_{dc,1}} & \frac{\partial T}{\partial V_{dc,3}} & \frac{\partial T}{\partial V_{dc,4}} & \frac{\partial T}{\partial P_{dc,2}} & \frac{\partial T}{\partial V_{dc,2}} \end{bmatrix} \tag{185}$$

The H matrix is same as the power-flow jacobian matrix and it is augmented by one column corresponding to the partial derivative with respect to $P_{dc,2}$. This column has all zeros and a +1 corresponding to the partial derivative of F_4 (181). Performing SVD of the H matrix (185) as explained in section II B (158) the tangent at $\boldsymbol{\omega_1}$ namely $\boldsymbol{\alpha_1}$ is obtained and is given in Table 9. It should be noted that the tangent calculated using the method in [78] is normalized. Thus

$$\|\boldsymbol{\alpha_1}\|_2 = 1 \tag{186}$$

Since the tangent (186) is normalized, (159) corresponds to the equation of a plane. Once the tangent at $\boldsymbol{\omega_1}$ is obtained, the subsequent point, $\boldsymbol{\omega_2}$ has to be traced. Equations (178)-(183) constitute a set of 6 equations with 7 unknowns. An additional equation, which is the equation of the plane, is given by (159) which can be rewritten as

$$\Delta P_{dc1}P_{dc1} + \Delta P_{dc3}P_{dc3} + \Delta V_{dc1}V_{dc1} + \Delta V_{dc3}V_{dc3} + \Delta V_{dc4}V_{dc4} + \Delta P_{dc2}P_{dc2} + \Delta V_{dc2}V_{dc2} = \alpha_1 \bullet \omega_1 + s \quad (187)$$

Parameter	Value	Units
$V_{nl,1}$	48	V
$V_{nl,3}$	48	V
R_{d1}	0.2	Ω
R_{d3}	0.5	Ω
P_{ld4}=-($P_{dc,4}$)	697.5	W

Table 8: Parameters of the 4 Bus Test System [77]

Quantity	ω_0	ω_1	α_1
$P_{dc,1}$	0	569.763	0.5599
$P_{dc,3}$	0	243.224	0.2380
$V_{dc,1}$	48	45.495	-0.0026
$V_{dc,3}$	48	45.316	-0.0028
$V_{dc,4}$	48	45.019	-0.0027
$P_{dc,2}$	-630	-108.702	-0.7937
$V_{dc,2}$	48	45.346	-0.0031

Table 9: First Point on the Contour

		s=10	s=100	s=500
Quantity	ω_1	ω_2	ω_2	ω_2
$P_{dc,1}$	569.763	575.3622	625.7971	850.9309
$P_{dc,3}$	243.224	245.6035	267.0269	362.4098
$V_{dc,1}$	45.495	45.4692	45.2330	44.1448
$V_{dc,3}$	45.316	45.2885	45.0354	43.8695
$V_{dc,4}$	45.019	44.9913	44.7445	43.6073
$P_{dc,2}$	-108.702	-116.6379	-188.0318	-504.5976
$V_{dc,2}$	45.346	45.3145	45.0298	43.7186

Table 10: Subsequent Points for Different Step Lengths

Quantity	ω_{ld2max}	α_{ld2max}
$P_{dc,1}$	2822.671	-0.97
$P_{dc,3}$	1144.675	-0.235
$V_{dc,1}$	27.386	0.0286
$V_{dc,3}$	25.914	0.0307
$V_{dc,4}$	25.979	0.0305
$P_{dc,2}$	-2846.102	-0.0001
$V_{dc,2}$	23.640	0.034

Table 11: Loadability Point at Bus 2

where the terms with the prefix Δ are the components of the tangent $\boldsymbol{\alpha}_1$. Now the equations (178)-(183) and (187) are solved iteratively taking the point $\boldsymbol{\omega}_1 + s\boldsymbol{\alpha}_1$ as the initial guess. The subsequent points for 3 different step lengths are given in Table 10. The points in Table 10 are verified to lie on the contour by using the power flow program

[77]. The $P_{ld,2}$ vs. $V_{dc,2}$ contour has been obtained using the proposed method and is shown in Fig. 66. The loadability at bus 2 is observed to be 2846.102W. The value of $V_{dc,2}$ at this point is 23.64V. The other unknown components at the point namely $\boldsymbol{\omega_{ld2max}}$ is given in Table. 11. It should be noted that the component corresponding $V_{dc,2}$ in the tangent attains its maximum value at $\boldsymbol{\omega_{ld2max}}$.

To show the validity of the proposed method, the system shown in Fig. 63 is dynamically simulated. The droop controlled sources at buses 1 and 3 are replaced with droop controlled buck converters. In [70], a linear droop of the dc microgrid voltage with respect to the inductor currents of the parallel connected buck converters supplying a CPL has been implemented. It has been shown in [70] that such a linear droop enables current sharing among the paralleled converters and also damps the limit cycle oscillations due to CPL. The control scheme for buck converter at bus 1 is given by

$$\boldsymbol{d_{1P}} = \frac{\boldsymbol{V_{nl,1}} - \boldsymbol{x_1 R_{d1}}}{\boldsymbol{E_1}} \tag{188}$$

where x_1 is the inductor current of the buck converter at bus 1. The parameters of the buck converters are as follows. E_1=64V, E_3=72V, C_1=C_3=1000μF, L_1=L_3=640μH, R_{d1}=0.2Ω and R_{d3}=0.5Ω where the subscripts 1 and 3 refer to the buck converter and control parameters at the respective voltage drooped buses. In [17], [70] a stability criterion has been derived which places a limit on the maximum value of CPL that can be supplied at a microgrid. However, there also exist several other stability criteria to be satisfied which relate to the parallel connected buck converters circuit parameters [70]. To make sure that instability only occurs due to the maximum load being exceeded and not due to the buck converters inductors and capacitors, additional capacitors of 8000μF need to be added at all the buses. The circuit thus obtained is simulated for 2 load powers namely P_{ld2}=2846W and P_{ld2}=2847W. The results obtained for two load powers

mentioned above are given in the Fig. 67. It can be observed from Fig. 67 that limit cycle oscillations are observed in the $V_{dc,2}$ waveform. However, when the primary controller is inserted at t=0.3s, the limit cycle oscillations are damped and $V_{dc,2}$ reaches the equilibrium value of 23.64V for P_{ld2}=2846W whereas for P_{ld2}=2847W, $V_{dc,2}$ becomes zero leading to voltage collapse. An interesting result can be observed regarding the voltage at bus 2 when the maximum power is supplied at the same bus. In [70], the equilibrium value of the microgrid voltage for parallel connected droop-controlled buck converters is given by

$$V_{\mu g} = \frac{V_{nl} + \sqrt{\left(V_{nl}^2 - 4PR_{d12}\right)}}{2} \tag{189}$$

where $V_{\mu g}$ is the equilibrium value of the microgrid voltage and $R_{d12}=R_{d1}||R_{d2}$. It can be observed from (189) that maximum P will be supplied when the microgrid voltage $V_{\mu g}=(V_{nl}/2)$ provided the stability criteria related to the buck converters circuit parameters are satisfied and the line resistances are ignored. In the simulation performed, $V_{dc,2}$ reaches the equilibrium value of nearly (V_{nl}/2) when maximum power is supplied at bus 2. This confirms that loadability calculated using the proposed approach is the absolute maximum real power that can be supplied at the microgrid bus.

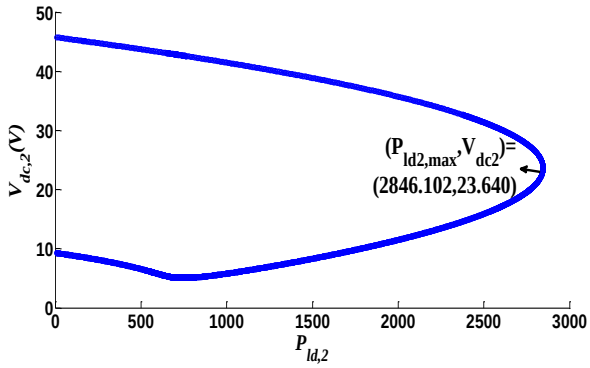

Fig.66. P_{ld2} Vs $V_{dc,2}$ for 4 bus dc microgrid

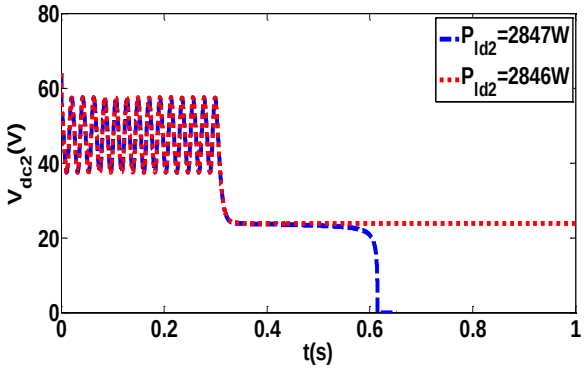

Fig. 67. Simulation results for P_{ld2}=2846W and P_{ld2}=2847W

SUMMARY

A method to trace the operating points of a droop controlled DC microgrid with CPLs is proposed. As a result, the maximum load that can be supplied at a microgrid bus is obtained. The various buses in a droop controlled DC microgrid are described and the system equations are presented. The generalized circle diagram algorithm is modified and applied to obtain the operating points. Simulations performed on an example microgrid validate the proposed method.

Chapter 7: Conclusions

CONTRIBUTIONS

In this dissertation, a general methodology to develop hierarchical control schemes for dc microgrids loaded by CPLs is proposed. The objective of this research work is that of stable operation of a dc microgrid with acceptable operating conditions in the presence of CPLs. In addition, another important goal of this research work is to ensure proper current sharing among parallel connected sources in a dc microgrid. To attain the above mentioned objectives, certain modifications are made to the hierarchical control architecture available in the literature. Firstly, the lower control level in the hierarchy, namely primary droop controller has to account for the presence of CPLs in the microgrid in addition to its assigned task of current sharing between the parallel connected converters. Hence the primary controller should ensure that the equilibrium point obtained after inserting it is stable. Secondly, the higher control level namely secondary controller is realized as follows. Two different architectures for secondary controllers are proposed namely autonomous and semi-autonomous. In the case of autonomous secondary controller, secondary control algorithm is incorporated in each of the parallel connected converter modules. In the case of a semi-autonomous secondary controller, a remote secondary controller with a high speed communication link to the parallel converter modules is realized. The proposed control algorithms are tested on a variety of dc microgrids with different converter topologies. Simulation and experimental results obtained on these dc microgrids verify the proposed control algorithms. Finally an algorithm to obtain the stability limit of a general dc microgrid loaded by CPLs is proposed and is verified by simulations. Details of the various goals attained in this research work are as follows.

An autonomous controller is proposed to achieve current sharing of parallel connected buck converters in a dc micro-grid with constant power loads. A two stage controller is proposed, where current sharing is achieved with a primary/droop control that requires no communication between the converter modules. The output voltage in the main bus is drooped linearly with respect to the load current supplied by each of the converters. To compensate for the voltage deviations without affecting current sharing, the droop control is augmented by a secondary/voltage regulating control. Asymptotic stability of the equilibrium point with the proposed control input is examined using Lyapunov and conditions to ensure local asymptotic stability of the equilibrium points are derived. Simulations and experimental results are included to verify the analysis.

An autonomous control law is derived for a microgrid which consists of system of parallel connected boost converters supplying a constant power load. The control law derived using the passivity based approach consists of two stages. The first, primary stage involves a non-linear droop of the microgrid voltage with respect to the current supplied by each of the converters thereby enabling current sharing. The primary controller also damps the oscillations in the dc microgrid caused by the presence of the constant power load. The secondary controller adjusts for the voltage deviations due to the primary controller without affecting the current sharing. The conditions to ensure the asymptotic stability of the equilibrium points are derived. Experimental results are presented to verify the proposed control law.

A semi-autonomous control scheme is derived for a microgrid which consists of system of parallel connected buckboost converters supplying a constant power load using small-signal linearized approach. The control algorithm consists of two levels. The lower level consists of droop-based primary controllers. The primary controller enables current-sharing among paralleled sources and also damps limit cycle oscillations due to constant

power loads. The higher level consists of a secondary controller which compensates for voltage deviations due to primary controller. This higher level is implemented by a remote secondary controller which uses a high speed communication link to communicate to local controllers. The conditions to ensure local asymptotic stability of equilibrium points are explained using the equivalent circuit of converters. At each stage of controller design and stability analysis, the results obtained for three basic configurations are compared and analyzed. The control schemes and stability results are explained by considering a microgrid consisting of paralleled buckboost converters. Simulations and experimental results are used to verify the validity of the proposed control schemes.

A linear controller is proposed for dc microgrids with SEPIC, Cuk and Zeta power electronic converters supplying constant power loads. The controller is implemented in two stages. During the first stage, also known as active damping stage, limit cycle oscillations are damped by inserting a virtual resistance in series with the input inductor of each of the converters. During the second stage, an integral controller is added the first stage to compensate for the voltage deviations due to virtual resistance. The second stage, also known as voltage regulation stage maintains microgrid voltage within acceptable limits in the event of source and load variation. Linearization and small signal analysis are used to derive stability conditions for the equilibrium points. Simulation and experiments performed on a prototype microgrid are used to verify the proposed control laws.

The maximum real power load in a dc microgrid bus is traced geometrically. The dc microgrid is droop-controlled with the loads being constant power loads. The generalized circle diagram approach used in a conventional power system is modified to be used in a droop-controlled dc microgrid for this purpose. The different types of buses

present in a dc microgrid are described and the locus of operating points is then obtained by applying the generalized circle diagram approach. The proposed method is verified by simulations on a 4 bus dc microgrid.

FUTURE WORK

Hierarchical control schemes for microgrids with parallel connected converters of basic topologies are developed in chapters 2, 3 and 4. In chapter 5, control laws are proposed to stabilize higher order dc-dc converters supplying CPLs. The hierarchical control scheme can be extended to a dc microgrid consisting of parallel connected configurations of such higher order dc-dc converters. Further, a number of feasible multiple input dc-dc converter topologies have been developed in [74]. A possible area worth investigating could be to develop hierarchical control schemes for such multiple input converter configurations loaded with CPLs.

References

[1] P. Chiradeja and R. Ramakumar, “An approach to quantify the technical benefits of distributed generation,” *IEEE Trans. Energy Conversion.,*vol. 19, no. 4, pp. 764–773, Dec. 2004.

[2] S. Anand and B. G. Fernandes, "Steady state performance analysis for load sharing in DC distributed generation system", *Proc. 10th Int. Conf. Environ. Electr. Eng.*, pp. 1-4, 2011

[3] E. A. A. Coelho , P. C. Cortizo and P. F. D. Garcia "Small-signal stability for parallel-connected inverters in stand-alone AC supply systems", *IEEE Trans. Ind. Appl.,* vol. 38, no. 2, pp.533 -542, 2002

[4] D. P. Ariyasinghe and D. M. Vilathgamuwa, "Stability analysis of microgrids with constant power loads", *Proc. IEEE Int. Conf. Sustainable Energy Technol.*, pp. 279-284, 2008

[5] R. H. Lasseter, "Microgrids", *Proc. IEEE Power Eng. Soc. Winter Meeting,* 2002, vol. 1, pp. 305-308

[6] A. Kwasinski, Technological assessment of distributed generation systems operation during extreme events, IEEE PEDG 2012, pp 534-541.

[7] Office of Electricity Delivery and Energy Reliability, Smart Grid R&D Program. 2011. DOE Microgrid Workshop Report, San Diego, CA.

[8] R. Kamel, A. Chaouachi, and K. Nagasaka, “Detailed analysis of micro-grid stability during islanding mode under different load conditions,” *Engineering,* vol. 3, no. 5, pp. 508–516, 2011

[9] P. Piagi and R. H. Lasseter, "Autonomous control of microgrids", *Proc. IEEE Power Eng. Soc. General Meeting,* 2006, pp 1-8

[10]. A. Emadi, Y. J. Lee, K. Rajashekara, "Power electronics and motor drives in electric hybrid electric and plug-in hybrid electric vehicles", *IEEE Trans. Ind. Electron.,* vol. 55, no. 6, pp. 2237-2245, Jun. 2008

[11] J. Bryan, R. Duke and S. Round, "Decentralized generator scheduling in a nanogrid using dc bus signaling", *Proc. IEEE Power Eng. Soc. Gen. Meet.2004 ,* pp. 977-982.

[12] T. Dragičević, X. Lu, J. C. Vasquez, J. M. Guerrero, "DC microgrids—Part I: A review of control strategies and stabilization techniques", *IEEE Trans. Power Electron.*, vol. 31, no. 7, pp. 4876-4891, Jul. 2016.

[13] Z. H. Jian, Z. Y. He, J. Jia and Y. Xie, "A Review of control strategies for DC Micro-grid", *Proc. IEEE 4th International Conference on Intelligent Control and Information Processing (ICICIP)*, pp. 666-671, 2013

[14] *IEEE Standard 1547.7 (2013)* Guide to Conducting Distribution Impact Studies for Distributed Resource Interconnection; Dec. 2013

[15] *IEEE Standard 1547a (2014)* Standard for Interconnecting Distributed Resources with Electric Power Systems – Amendment 1; May 2014

[16] T. Dragicevic, X. Lu, J. C. Vasquez, and J. M. Guerrero, "DC microgrids – Part II: A review of power architectures, applications and standardization issues," *IEEE Trans. Power Electron.*,vol. 31, no. 5, pp. 3528–3549, May 2016

[17] A. Kwasinski and C. N. Onwuchekwa, "Dynamic behavior and stabilization of dc microgrids with instantaneous constant-power loads", *IEEE Trans. Power Electronics,* vol. 26, No 3, pp. 822-834, Mar. 2011.

[18] A.Kwasinski and P. T. Krein, "Passivity-based control of buck converters with constant-power loads," in *Proc. 2007 Power Electronics Specialists Conference. PESC 2007*, pp. 259-265.

[19] A. Emadi, A. Khaligh, C. H. Rivetta, and G. A. Williamson, "Constant power loads and negative impedance instability in automotive systems: Definition, modeling, stability, and control of power electronic converters and motor drives," *IEEE Trans. Veh. Technol*., vol. 55, no. 4, pp. 1112–1125, Jul. 2006.

[20] T. Dragicevic, J. Guerrero , J. Vasquez and D. Skrlec "Supervisory control of an adaptive-droop regulated dc microgrid with battery management capability", *IEEE Trans. Power. Electronics*, vol. 29, no. 2, pp.695 -706, 2014

[21] A. M. Rahimi and A. Emadi, "An analytic investigation of DC/DC power electronic converters with constant power loads in vehicular power systems," *IEEE Trans. Power Electronics*., vol. 68, no. 6, pp.2689–2702, Jul. 2009.

[22] R. Majumder, " Some Aspects of Stability in Microgrids," *IEEE Trans. Power Systems,* vol. 28, no. 3, pp. 3243-3250, August 2013

[23] A. M. Rahimi and A. Emadi, "Active damping in dc/dc power electronic converters: A novel method to overcome the problems of constant power loads", *IEEE Trans. Ind. Electron*., vol. 56, no. 5, pp. 1428-1439, May 2009

[24] P. A. Dahono, "A control method for DC-DC converter that has an LCL output filter based on new virtual capacitor and resistor concept",in *Proc. 2004 Power Electronics Specialists Conference. PESC 2004* pp. 36-42.

[25] Y. A. R. I. Mohamed, and A. A. Radwan, "Hierarchical control system for robust microgrid operation and seamless mode transfer in active distribution systems", *IEEE Trans. Smart Grid,* vol. 2, pp. 352-362, Jun. 2011

[26] C. N. Onwuchekwa and A. Kwasinski, "Analysis of boundary control for buck converters with instantaneous constant-power loads," *IEEE Trans. Power Electronics*, vol 25, no 8, pp. 2018-2032, Aug. 2010.

[27] A. Rahimi, G. A. Williamson and A. Emadi, "Loop-cancellation technique: A novel nonlinear feedback to overcome the destabilizing effect of constant-power loads", *IEEE Trans. Veh. Technol.*, vol. 59, no. 2, pp. 650-661, Feb. 2010.

[28] J. Wang and D. Howe, "A power shaping stabilizing control strategy for DC power systems with constant power loads" *IEEE Trans. Power Electronics*, vol 23, no 6, pp. 2982-2989, Nov. 2008.

[29]V. Yousefzadeh, A. Babazadeh, B. Ramachandran, E .Iarcon, L.Pao and D. Maksimovic, "Proximate-Time Digital Control for Synchronous Buck DC-DC converters," *IEEE Trans. on Power Electronics,* vol. 23, no. 4, pp. 2018-2026, Jul. 2008.

[30] A. Kwasinski and P. T. Krein, "Stabilization of constant power loads in dc-dc converters using passivity based control ," in Proc *29th International Telecommunications Energy Conference, 2007 . INTELEC 2007*, pp. 867-874.

[31] C. N. Onwuchekwa and A. Kwasinski, "Analysis of boundary control for boost and buck-boost converters in distributed power architectures with constant-power loads," in Proc. *2011 Applied Power Electronics Conference (APEC) 2011*, pp. 1816-1823.

[32] Y. Li, K. R. Vannorsdel, A. J. Zirger, M. Norris, and D. Maksimovic, "Current mode control for boost converters with constant power loads," *IEEE Trans. Circuits Syst.* I, Reg. Papers, vol. 59, no. 1, pp. 198–206, Jan. 2012.

[33] S. Anand and B. G. Fernandes, " Reduced-order model and stability analysis of a low-voltage DC microgrid", *IEEE Trans. Industrial Electronics*, vol 60, No 11, pp. 5040-5049, Nov. 2013.

[34] R. S Balog, W. W Weaver and P. T Krein, "The load as an energy asset in the distributed DC SmartGrid architecture" *IEEE Trans. Smart Grid*, vol 3, no 1, pp. 253-260, Mar. 2012.

[35] M. Cespedes, L. Xing, and J. Sun, "Constant-power load system stabilization by passive damping," *IEEE Trans.Power Electron.*, vol. 26, no. 7, pp. 1832–1836, Jul. 2011.

[36] A. Emadi, and M. Ehsani, "Negative impedance stabilizing controls for PWM dc/dc converters using feedback linearization techniques" *Proc. 35thth Annual Energy Conversion Engineering Conference and Exhibit, IECEC-2000*, vol 1, pp. 613-620

[37] P. Magne, D. Marx, B. Nahid-Mobarakeh, and S. Pierfederici, "Large-Signal Stabilization of a DC-Link Supplying a Constant Power Load Using a Virtual Capacitor: Impact on the Domain of Attraction,", *IEEE Transactions on Industry Applications*, vol. 48, No 3, pp. 878-887, May/Jun 2012.

[38] J. M. Guerrero , J. C. Vasquez , J. Matas, L. G. de Vicuna and M. Castilla , "Hierarchical control of droop-controlled ac and dc microgrids - A general approach toward standardization" , *IEEE Trans. Ind. Electron.* , vol. 58 , no. 1 , pp.158 -172 , 2011

[39]B. T. Irving and M. M. Jovanovic, "Analysis, design and performance evaluation of droop current sharing methods", *Proc. IEEE Applied Power Electronics Conf. (APEC',00)*, pp. 235-241, 2000

[40]J. Shi, L. Zhou, X. He, "Common-duty-ratio control of input-parallel output-parallel (IPOP) connected dc–dc converter modules with automatic sharing of currents", *IEEE Trans. Power Electron.*, vol. 27, no. 7, pp. 3277-3291, Jul. 2012.

[41]S. K. Mazumder, M. Tahir, and K. Acharya, "Master–slave current sharing control of a parallel dc–dc converter system over an RF communication interface," *IEEE Trans. Ind. Electron.*, vol. 55, no. 1, pp. 59–66, Jan. 2008.

[42]S. Anand , B. G. Fernandes and J. M. Guerrero , "Distributed control to ensure proportional load sharing and improve voltage regulation in low-voltage dc microgrids" , *IEEE Trans. Power Electron.* , vol. 28 , no. 4 , pp.1900 -1913 , 2013

[43]P. Wang, X. Lu , X. Yang,, W. Wang and D. Xu, "An Improved Distributed Secondary Control Method for DC Microgrids With Enhanced Dynamic Current Sharing Performance," *IEEE Trans. Power Elec,* vol. 31, no. 9, pp. 6658–6673, Sep. 2016

[44] X. Lu , K. Sun , J. M. Guerrero , J. C. Vasquez , L. Huang and R. Teodorescu, "SoC-based droop method for distributed energy storage in DC microgrid applications", *Proc. 2012 IEEE Int. Symp. Ind. Electron. (ISIE)*, 2012

[45] N. L. Diaz, T. Dragicevic, J. C. Vasquez and J. M. Guerrero, "Intelligent distributed generation and storage units for DC microgrids - A new concept on cooperative control without communications beyond droop control," *IEEE Trans. Smart Grid*,vol 5, No 5, pp 2476-2485, Sep 2014 .

[46]T. Dragicevic, J. M. Guerrero and J. C. Vasquez "A distributed control strategy for coordination of an autonomous LVDC microgrid based on power-line signaling," *IEEE Trans. Industrial Electronics*,vol 61, No 7, pp 3313-3326, Jul 2014 .

[47] E. Jamshidpour , B. Nahid-Mobarakeh , P. Poure , S. Pierfederici and S. Saadate, "Distributed stabilization in DC hybrid power systems", *Proc. IEEE Veh. Power Propulsion Conf.*, pp.1-6 Sep. 2011

[48] R. W. Erickson and D. Maksimovic, *Fundamentals of Power Electronics* Norwell, MA: Kluwer, 1997

[49] A. Emadi and S. S. Williamson, "Fuel cell vehicles: Opportunities and challenges," in Proc. *IEEE Power Eng. Soc. Gen. Meeting*, Denver, CO, Jun. 2004, pp. 1640–1645.

[50] L. Solero, A. Lidozzi, and J. A. Pomilio, “Design of multiple-input power converter for hybrid vehicles,” .*IEEE Trans. Power Electron*ics., vol. 20, no. 5, pp. 1007–1016, Sep. 2005.

[51] S. Bae and A. Kwasinski, “Maximum power point tracker for a multiple-input dc-dc Cuk converter,” in Proc. *31st International Telecommunications Energy Conference, 2009,*, pp. 1 –5.

[52] R. Zhao and A. Kwasinski, "Multiple-input single ended primary inductor converter (SEPIC) converter for distributed generation applications," in Proc. *Energy Conversion Congress and Exposition, 2009. ECCE 2009*, pp. 1847-1854.

[53] G. Preetham and W. Shireen, "Photovoltaic station for plug-in hybrid electric vehicles in a smart grid environment,", in Proc. *IEEE PES Innovative Smart Grid Technologies Conf*., 2012, pp. 1-8

[54] A. P. N. Tahim, D. J. Pagano, E. Lenz, V. Stramosk, "Modeling and stability analysis of islanded dc microgrids under droop control", *IEEE Trans. Power Electron.,* vol. 30, no. 8, pp. 4597-4607, Aug. 2015.

[55] P.-H. Huang, W. Xiao, M. El Moursi, "A practical load sharing control strategy for DC microgrids and DC supplied houses", *Proc. 39th Annu. Conf. IEEE Ind. Electron. Soc. (IECON 2013)*, pp. 7124-7128, 2013.

[56] L. Meng, T. Dragicevic, J. M. Guerrero, J. C. Vasquez, "Dynamic consensus algorithm based distributed global efficiency optimization of a droop controlled dc microgrid", *Proc. IEEE Energy Conf.*, pp. 1276-1283, May 2014.

[57] Y. Gu, X. Xiang, W. Li, X. He, "Mode-adaptive decentralized control for renewable DC microgrid with enhanced reliability and flexibility", *IEEE Trans. Power Electron.*, vol. 29, no. 9, pp. 5072-5080, Sep. 2014.

[58] K. Sun, L. Zhang, Y. Xing and J. M. Guerrero, "A Distributed control strategy based on DC bus signaling for modular photovoltaic generation systems with battery energy storage", *IEEE Trans. Power Electron.,* vol. 26, no. 10, pp. 3032-3045, Oct. 2011.

[59] F. Ochoa , A. P. Feltrin and G. P. Harrison, "Evaluating distributed generation impacts with a multiobjective index", *IEEE Trans. Power Del.*, vol. 21, no. 3, pp. 1452-1458, 2006

[60] P. Kundur, Power System Stability and Control, New York:McGraw-Hill, 1994.

[61] A. Emadi and M. Ehsani, “Multi-converter power electronic systems: Definition and applications,” in Proc. *32nd Power Electron. Spec. Conf., PESC 2001*, pp. 1230–1236.

[62] C. Rivetta, G. A. Williamson, "Large-signal analysis of a DC-DC buck power converter operating with constant power load", *Proc. IEEE Ind. Electron. Conf.*, 2003, pp. 72-78

[63]. D. Czarkowski, M. K. Kazimierczuk, "Static and dynamic-circuit models of PWM buck-derived dc–dc convertors", *IEE Proceedings G Circuits Devices and Syst.,* vol. 139, no. 6, pp. 669-679, Dec.1992.

[64] M. Veerachary, "Analysis of fourth-order dc–dc converters: A flow graph approach", *IEEE Trans. Ind. Electron.*, vol. 55, no. 1, pp. 133-141, Jan. 2008.

[65] R. Leyva, D. Maksimovic, R. Ling, "Second-order sliding-mode controller for higher-order DC-DC converters", *IEEE 15th Workshop Control Model. Power Electron.*, pp. 1-7, 2014.

[66] H. K. Khalil, *Non-linear Systems*, Third edition. New Jersey: Prentice Hall, 2002.

[67]K. Ogata, *Modern Control engineering*, Third edition. New Jersey: Prentice Hall, 1997

[68] X. Feng, Z. Ye, K. Xing, F. C. Lee and D. Borojevic, "Impedance specification and impedance improvement for dc distributed power system", *Proc. IEEE PESC*, vol. 2, pp. 889-894.

[69] R. D. Middlebrook and S. Cuk, "A general unified approach to modeling switching-converter power stages", *Proc. IEEE PESC*, pp. 18-34, 1976

[70] M. Srinivasan and A. Kwasinski, ”Autonomous Hierarchical Control of dc microgrids with Constant Power Loads” *Proc. Applied Power Electronics Conference and Exposition (APEC)* 2015, pp 2808-2815

[71] M. Srinivasan and A. Kwasinski, “Decentralized Control of a Vehicular Microgrid with Constant Power Loads”, *Proc IEEE Electric Vehicle Conference (IEVC),* 2014, pp.1-8.

[72] R. D. Middlebrook, “Input filter considerations in design and application of switching regulators,” in *Proc. IEEE Ind. Appl. Soc. Annu. Meet.,1976,* pp. 366–382.

[73] S. Anand and B. G. Fernandes, "Optimal voltage level for DC microgrids", *Proc. 36th Annu. IEEE Ind. Electron. Soc. Conf.*, pp. 3034-3039, 2010

[74] A. Kwasinski, "Identification of feasible topologies for multiple-input dc–dc converters", IEEE Trans. Power Electron., vol. 24, no. 3, pp. 856-861, Mar. 2009.

[75] J. W. Valvano, *Embedded Systems: Real-time Interfacing of Arm® Cortex(TM)-M4 Microcontrollers*, vol 2, CreateSpace Independent Publishing Platform, 2014

[76] Texas Instruments, “Tiva™ TM4C123GH6PM Microcontroller” TM4C123 datasheet, Revised June.2014.

[77] C. Li, S. K. Chaudhary, T. Dragicevic, J. C. Vasquez, and J. M. Guerrero, “Power flow analysis for DC voltage droop controlled DC microgrids”, *Proc. 11th International Multi-Conference on Systems, Signals & Devices (SSD),* 2014, pp. 1-5

[78] G. B. Price, "A Generalized Circle Diagram Approach for Global Analysis of Transmission System Performance," *IEEE Trans Power App and Syst*, Vol PAS-103, No 10, pp 2881-2890, Oct 1984

[79] C. L. Lawson and R. J. Hanson. "*Solving Least Squares Problems*", Prentice Hall Inc., 1974.

[80] H. W. Dommel, W. F. Tinney, and W. L. Powell, "Further developments in Newton's method for power system applications," *Proc. IEEE Winter Power Meet,* 1970.